# HOLOCENE POSTGLACIAL FLUVIAL PROCESSES AND LANDFORMS IN LOW RELIEF LANDSCAPES

A Dissertation
Submitted to the Graduate Faculty
of the
North Dakota State University
of Agriculture and Applied Science

By

Zachary Rockford Phillips

In Partial Fulfillment of the Requirements
for the Degree of
DOCTOR OF PHILOSOPHY

Major Program:
Environmental and Conservation Science

July 2020

Fargo, North Dakota

# North Dakota State University
## Graduate School

**Title**

HOLOCENE POSTGLACIAL FLUVIAL PROCESSES AND LANDFORMS IN LOW RELIEF LANDSCAPES

**By**

Zachary Rockford Phillips

The Supervisory Committee certifies that this ***disquisition*** complies with North Dakota State University's regulations and meets the accepted standards for the degree of

**DOCTOR OF PHILOSOPHY**

SUPERVISORY COMMITTEE:

Stephanie Day
Chair

Benjamin Laabs

Aaron Daigh

Xuefeng Chu

Approved:

7 / 14 / 2020
Date

Craig Stockwell
Department Chair

## ABSTRACT

Postglacial rivers are part of the relatively young low-relief landscape system left behind by glaciers. Over time, postglacial rivers are susceptible to both minor and major channel planform changes as the Earth and its newly exposed rivers adjust to new isostatic and geomorphic equilibriums. Those planform changes result in topographic features that are well preserved among the largely unaltered landscape and offer opportunities to learn about the processes that create them. This work focuses on those minor and major planform changes and the resulting landforms, with a focus on processes effecting the glaciolacustrine Red River Valley. Here, three studies were conducted, two regarding minor planform changes and one focusing on major planform changes. Studies included in this work regard 1) the spatial distribution of meander cutoffs and meander cutoff relief on the Red River, 2), avulsion timing and length resulting from isostatic tilting and 3) mobile river ice and bank interaction frequency, locations, and erosion in meandering rivers. Results show that rivers develop meander cutoffs that faster in areas where geologic materials are more easily eroded and their relief shows a positive relationship with the rate of river incision. Major channel path changes (avulsions) in the presence of isostatic tilting were found to be most frequent soon after river establishment while rates of isostatic rebound are high enough to outpace channel incision. River ice was found to most frequently interact with the outer banks of channels with long, tight bends and high sinuosity, potentially contributing to the meandering process. From these results it can be interpreted that postglacial rivers were highly dynamic early in their history and have stabilized over time, with most of the changes occurring in areas with more erodible alluvium. Presently, rivers undergo most of their changes during the spring thaw when mobile river ice is impacting the banks, with sinuous river reaches impacted most frequently by mobile river ice.

## ACKNOWLEDGEMENTS

I give my great appreciation to the four members of my advisory committee, Stephanie Day, Benjamin Laabs, Aaron Daigh, and Xuefeng Chu for their constructive criticisms during the review of this dissertation. Each of them carries key knowledge and passion for each of the different subjects covered in this document. I thank and congratulate Stephanie Day for giving me the opportunity and freedom to pursue this research as her first Doctoral student at NDSU. I have enjoyed every moment of this work and I have learned a lot along the way. The NDWRRI Fellowship program provided funding to support this work and the ND Governor's School Program supplied great research assistants and funding that aided in conducting pilot studies.

Those academics and professionals who have advised me and given me help along the way are also deserving of recognition. I would like to thank Ralph von Frese for facilitating my interest in seismicity as an undergraduate and giving me advice that has guided me through two other degrees. I would like to thank my M.S. advisory committee who initiated my interest in rivers and geomorphology, Scott Drzyzga, Sean Cornell, and Chris Woltemade. Without their support I would have had no interest to continue my pursuit of knowledge.

I would also like to thank the nonacademic members of my life who have supported me no matter what life path I choose. My parents, Barb and George, have been pivotal in supporting my education and I would not be anywhere near where I am today without them. My sister, Sydney has been a huge inspiration as I have worked through my degrees and has always been supportive of me no matter what. Elise, Mary, Finnley, and Sisko have made my short escapes from work a great deal of fun. Elise, you have put up with a lot of my stress throughout this process. Thank you for being patient with me and being positive when I was not so happy

## TABLE OF CONTENTS

## LIST OF TABLES

## LIST OF FIGURES

## LIST OF EQUATIONS

## LIST OF APPENDIX FIGURES

# CHAPTER I: INTRODUCTION

Rivers are part of highly variable and dynamic integrated landscape systems, reflecting changes in those systems through their morphology (Schumm, 1977; 1985). In North America, during the Pleistocene glaciers loaded the asthenosphere with ice up to 3.2 km thick across more than 13,000,000 $km^2$ and lead to the reorganization and denudation of drainage networks (Flint, 1971; Dyke et al., 2003; Shugar et al., 2017). After glacial activity ceases, early in their history, rivers are highly susceptible to changes that display the initial morphologic evolution of postglacial landscapes (Gran et al., 2013).

During this initial period, rivers erode as the equilibrium between the lithosphere and asthenosphere is re-established and postglacial isostatic rebound drives regional landscape tilting and vertical motion. In areas of glacial deposition the contemporaneous processes of erosion and glacial rebound leave behind signatures recording planform changes and landscape evolution history of postglacial rivers (Burnett and Schumm, 1983; Holbrook and Schumm, 1999; Maddy and Bridgland, 2000; Clark et al., 2012; Gran et al., 2013). Depending on their orientation, as the landscape tilts, rivers can become steeper, more gradual, tilt laterally, or some combination of the prior. Rivers have well-studied responses to such adjustments, which involve changes in sinuosity and lateral shifting (Schumm, 1977; Piégay and Schumm, 2003; Constantine et al., 2010).

Not only do postglacial river planforms reflect landscape scale inputs from tectonic motions, but also spatial variations in surficial geology resultant of patterns of glacial deposition tied to glacial surges, standstills, and recession (Schumm, 1985). The study of planform variations due to alluvial variations in postglacial rivers is important because postglacial rivers are near enough to the date of their establishment so that the overprinting of initially established

fluvial landforms has not yet occurred. In postglacial rivers, variations in river planforms arise from differences in alluvium composition (Lewis and Lewin, 1983), the confinement of river channels (Lewis and Lewin, 1983), local stream power (Phillips and Desloges, 2014; 2015), and initially established fluvial conditions after glacial retreat (Curran et al., 2017).

Although glacial ice had melted away from the North American continent by roughly 8,000 ka (Dyke et al., 2003), ice presently continues to be associated with dynamic changes in those postglacial rivers exposed to freezing temperatures during the winter (Arnborg et al., 1967; Outhet, 1974; Gatto, 1995; Walker and Hudson, 2003). Ice erodes rivers and changes their planform by abrading and gouging bank sediments (Borland, 1959; Smith, 1979; Doyle, 1988; Brooks, 1993; Wuebben, 1995; MacKay and MacKay, 1977; Lotsari et al., 2015), prying away sediments by bankfast ice loading (Ettema, 2002; Zabilansky, 2002), freeze-thaw processes (Anderson et al., 1978; Gatto, 1995; Ferrick and Gatto, 2005; Dagesse, 2013; Edwards, 2013), ice jamming and floods (Smith and Pearce, 2002), and ice grounding (Beltaos, 1995).

This dissertation focuses on the connection between process and landform in postglacial rivers and highlights the influence of spatial and temporal variations in processes and pre-existing conditions on the current fluvial landforms. Studies are focused on the past and present variations in processes leading to small and large scale changes in the planform and path of rivers near the margin of the Laurentide Ice Sheet, on the bed of former glacial Lake Agassiz in the Red River Valley (North Dakota and Minnesota, USA). Organized into three chapters, focus is taken toward 1) small-scale planform changes in the form of meander cutoffs, 2) large-scale channel path changes by channel avulsion, and 3) present-day meander growth by mobile river ice floes.

## Objectives

The objectives of this research focus on the connection between erosion processes and landforms in postglacial rivers, with an emphasis on ice's erosional effect on rivers of the past and present in the low-relief Red River Basin and Red River Valley. Within that scope, focus on particularly erosive temporal periods is taken.

The first objective was identifying variations in fluvial erosion along the Red River, which was performed using an automated GIS tool developed here to map meander cutoffs. Meander cutoffs were of focus because they act as a proxy for fluvial erosion and are influenced by the basin's full postglacial history.

The second objective of this research focused on studying large-scale channel path changes that occur in low-relief, postglacial landscapes from tilting caused by Glacial Isostatic Adjustments. Further concentration is taken toward variables indicated by the work of other researchers to affect the nature of channel path shifts and whether they occur gradually or abruptly.

Finally, the third objective of this research focuses on the present influence of ice on river erosion. Emphasis falls upon the process of abrasion and plucking of mobile river ice floes to begin separating the erosional effects of river ice during the winter-to-spring transition, which is the busiest period of erosion for many postglacial rivers and those that freeze for a portion of the year.

## Literary background

This section organizes content that is relevant to this dissertation. Focus is taken toward the Red River Valley in North Dakota and Minnesota, USA and Manitoba, CAN. Topics covered

in this section include 1) late-Wisconsinan glacial history of the Red River Valley, 2) glacial Lake Agassiz, 3) postglacial isostatic adjustments, 4) postglacial landscape evolution, 5) meandering river erosion, and 6) fluvial ice processes. Throughout this review emphasis is taken toward items that are important in the studies of fluvial geomorphology presented later in this dissertation.

### *Late-Wisconsinan glacial history of the Red River Valley*

The alluvium of postglacial rivers controls their form and process (Curran et al., 2017; Phillips and Desloge, 2014; 2015), which in the Red River Valley is directly related to the late-Wisconsinan glacial history and the palimpsest overprinting of glacial sediments by Glacial Lake Agassiz. The Red River Valley has experienced four major glacial advances during the Pleistocene; the Nebraskan (900–780 ka), the Kansan (640-500 ka), the Illinoisan (350-140 ka), and the Wisconsinan (60-11.7 ka) (Boellstorff, 1978; Bierman et al., 1999). In the Red River Valley most glacial deposits are buried beneath glaciolacustrine Lake Agassiz deposits, but the surficial geology that is exposed at the surface is comprised of the final sequence of late-Wisconsinan glacial tills and moraines deposited as the Des Moines lobe retreated and the Red River Lobes readvanced and then retreated northward during the final deglaciation sequence (Harris, 1987, 1995; Harris and Luther, 1991; Fullerton et al., 2003).

During the late-Wisconsinan glacial advance, the Des Moines Lobe of the Laurentide Ice Sheet (LIS) extended southward, flowing through the Red River Valley as far south as Iowa (Mickelson and Colgan, 2003). During the period of glacial retreat after the deposition of the Bemis moraine at 14 ka BP, glaciers paused for periods and made significant readvances into the Red River Valley (Wright and Ruhe, 1965). During the last sequence of recession, pauses and

readvances in the late-Pleistocene and early-Holocene played a significant role in depositing glacial sediments exposed at the surface of the modern Red River Valley (Harris, 1987, 1995; Harris and Luther, 1991).

Specifically, the standstill resulting in the Comstock ice margin shortly after 14 ka BP (Ruhe, 1969; Clayton and Moran, 1982) but before 13.5 ka BP (Teller and Fenton, 1980), which deposited an unnamed moraine partially buried by the Sheyenne River Delta (referred to as Unit A by Arndt [1975]). This moraine is referred to as the Comstock Moraine in this paper. After the Des Moines Lobe retreated from the Red River Valley for a period, the later Caledonia advance of the Red River Lobe at 13 ka BP (Dyke et al., 2003) resulted in the deposition of the Huot and Falconer formations (also known as the Edinburgh Moraine) in the central Red River Valley (Arndt, 1975; Fullerton et al., 2003) (Figure 1).

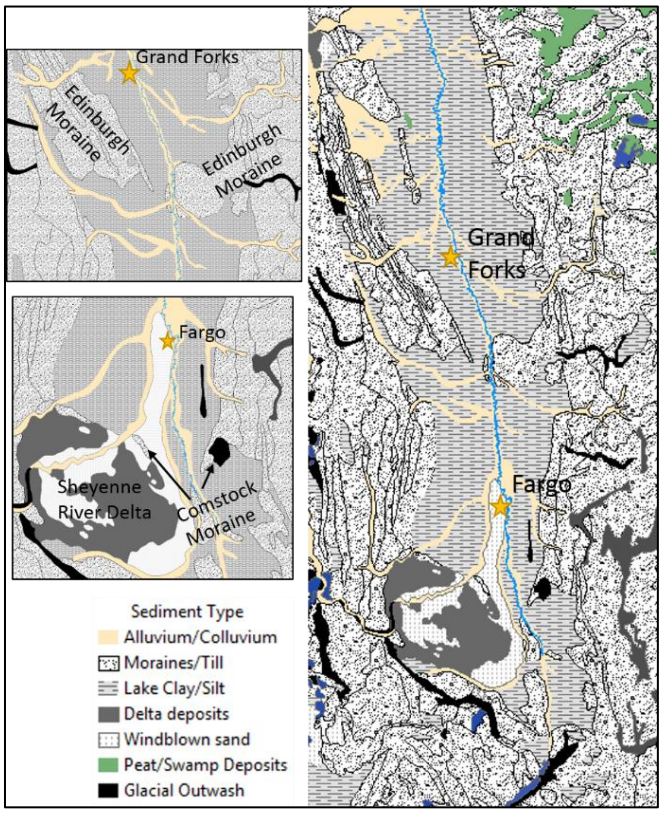


**Figure 1.** Surficial geology of the Red River Valley (produced with data from Fullerton et al., 2003). Much of the Red River Valley is dominated by glaciolacustrine clays, but areas of glacial moraines and deltaic deposits provide local variations in lithology.

The Red River Valley is understood to be dominated by clay-silt glaciolacustrine sediments (Brooks, 2003a) (Area A in Figure 1). Although, to the east of the valley and in the southern end of the Red River valley, where glacial Lake Agassiz was shallow and the landscape was inundated for the shortest period of time glaciolacustrine sediments are thin and highly altered by wave action (Ashworth et al., 1972). Where those deposits are thin and altered, denuded glacial topography is exposed at the surface along with deltaic topography and sediments deposited during the existence of Lake Agassiz (Harris, 1987, 1995; Harris and Luther, 1991; Fullerton et al., 2003) (Areas B and C in Figure 1). In glaciolacustrine areas near the Great Lakes, exposed glacial deposits lead to relatively sandy alluvium, high gradients, and locally high erosive forces that can lead to local fluvial planforms and processes that are anomalous to the otherwise uniform glaciolacustrine lake bottom (Phillips and Desloge, 2014; 2015; Thayer et al., 2016).

### *Glacial Lake Agassiz*

As the Des Moines and Red River Lobes of the LIS receded northward meltwater was dammed between topography to the south and the receding ice sheet to the north, leading to the formation of Lake Agassiz. Lake Agassiz formed first at 12 ka BP and persisted until 8 ka BP, and inundated the Red River Valley until 9.9 ka BP (Clayton and Moran, 1982; Teller and Bluemle, 1983; Bluemle, 1991; Teller and Leverington, 2004; Dilworth and Fisher, 2018). During its existence Lake Agassiz had three general highstands (Cass, Lockhart, and Emerson Phases) and one lowstand (Moorhead Phase) before it was drained from the landscape as the LIS retreated northward in the early Holocene (Figure 2).

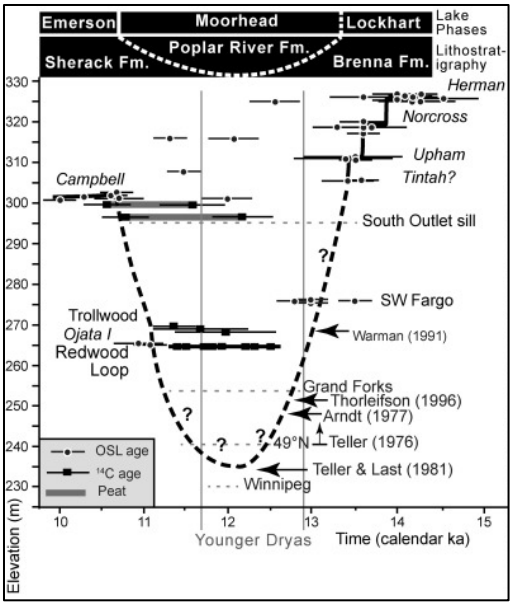


**Figure 2.** Lake Agassiz phases, stages, lithostratigraphy, and dated ages (from Dilworth and Fisher, 2018).

As the LIS went through periods of retreat and readvance, depending on the extent of the ice sheet, Lake Agassiz drained through three different main outlets known at the south, east and west outlets (Leverington and Teller, 2003). The southern outlet drained through the Mississippi River via the present day Minnesota River, the eastern outlet drained through the Great Lakes, and the western outlet through the Mackenzie River basins (Teller and Leverington, 2004).

Lake Agassiz is responsible for the deposition of glaciolacustrine lithologies that are found at the Earth's surface of the majority of the Red River Valley. The units deposited by Lake Agassiz are silty-clays and clays varying slightly in composition. During the early Cass Phase, the Wylie and Argusville Formations were deposited contemporaneously. The Wylie was deposited north of the Argusville Formation, gradationally divided by an undulation of Unit A (Arndt, 1975). Atop the undulation in Unit A the Falconer and Huot Formations (also known as the Edinburgh Moraine), a pebbly clay-loam, was deposited by the Caledonian readvance of the LIS. The Falconer is interpreted to have formed beneath glacial ice, while the Huot formed just south of the ice margin (Arndt, 1975).

After the Caledonian advance receded Lake Agassiz reached its deepest stage, known as the Lockhart Phase. The Lockhart Phase deposited the thick clay-rich Brenna Formation, which is ~25 meters thick in the center of the Red River Valley (Arndt, 1975). The Lockhart Phase lasted for nearly 900 years, but as glacial ice retreated and the east outlet opened the lake's level dropped for nearly 2,000 years (Dilworth and Fisher, 2018). During the Moorhead Phase and the Younger Dryas, the southern shore of Lake Agassiz fell just north of Grand Forks, ND (Breckenridge, 2015). During the Moorhead Phase fluvial activity began south of the shore of Lake Agassiz, and the Poplar River Formation was deposited within the fluvial corridors.

After the Younger Dryas, Lake Agassiz increased in depth and reached as far south as the Sheyenne River Delta once again. During this period lasting for ~900 years the Sherack Formation, a laminated silty clay, was deposited. The Sherack forms the upper-most unit of Lake Aggasiz stratigraphy, and is up to 9 meters thick (Arndt, 1975)

As Lake Agassiz changed outlets, the lake's volume fluctuated. Fluctuations in volume caused the areal extent of Lake Agassiz to fluctuate as well, depositing beach strandlines along the shores. Strandlines stand out among the otherwise flat topography as linear features less than 0.8 km wide (Clayton et al., 1980; Bluemle, 1991). Strandlines were deposited horizontally, recording changes in lake level and the tilt of the landscape as early Glacial Isostatic Adjustments (GIA) acted upon the valley. Due to the GIA-driven tilt, strandlines generally tilt upward at higher latitudes, with a gradually increasing slope to the north (Figure 3).

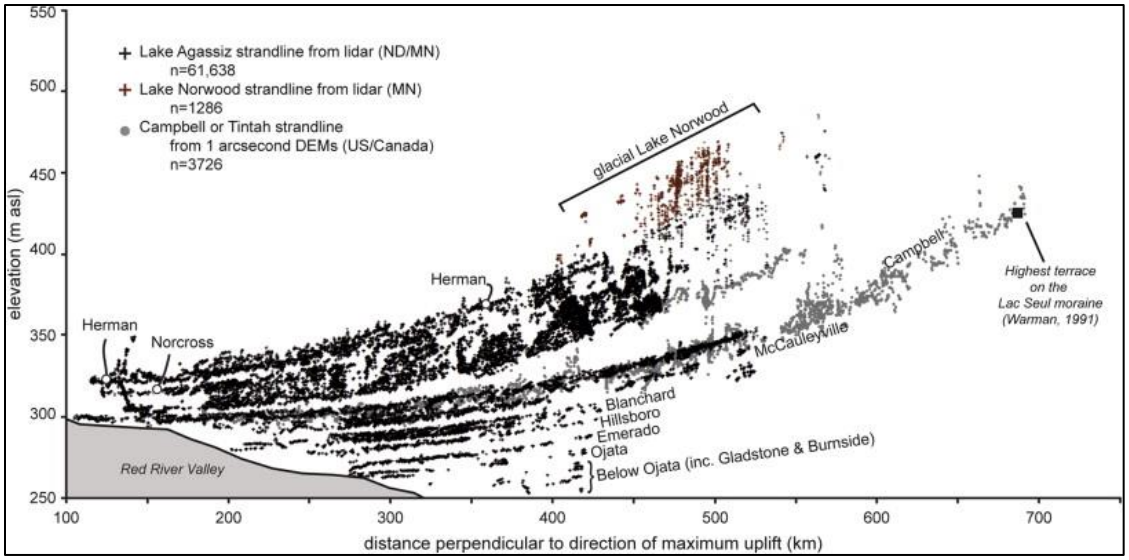


**Figure 3.** Present elevation of Lake Agassiz strandline points. Points show increasing upward tilt with increasing distance in direction of uplift, with older strandlines displaying a greater tilt (from Breckenridge, 2015).

Strandlines deposited during the Lockhart Phase of Lake Agassiz are at a higher elevation display a greater degree of upward tilt, which points to higher stages during the Lockhart Phase and increasing net rebound over time (Breckenridge, 2015). The Lake Agassiz strandlines track the history of GIA across the Red River Valley during the ~4,000 years following the recession of the Lake Agassiz and can grant scientists clues as to how the landscape was tilted soon after the draining of Lake Agassiz from the Red River Valley.

### *Postglacial isostatic adjustments*

Isostasy is the balance between the Earth's mantle and crust, which is pushed out of balance when mountains are built or eroded, when sea-level changes, or when glaciers accumulate or melt. Glacial Isostasy refers to the accumulation of glacial ice at the Earth's surface displacing the underlying lithosphere downward, and in turn the underlying asthenosphere is displaced and flows away from the depressed area. (Figure 4). At the margins of glaciers, the elastic behavior of the lithosphere causes the Earth's surface to bulge upward.

Postglacial Isostatic Adjustments (GIA), occur after glacial ice has melted from the Earth's surface and regional isostasy readjusts from the state of crustal depression brought on by glaciation.

Since the recession of the LIS, the North American continent has been adjusting to its new equilibrium (Upham, 1896). Rebound soon after glacial retreat, regardless of large or small ice mass or the strength of underlying rheology, was most rapid soon after deglaciation and decays with time (Figure 4). Rebound is generally most rapid in areas where glacial ice was thickest, and requires between 10,000 and 20,000 years for a new equilibrium to be reached (Walcott, 1970; Peltier, 2004). The temporal requirement for the relaxation of the mantle means that GIA is still active today.

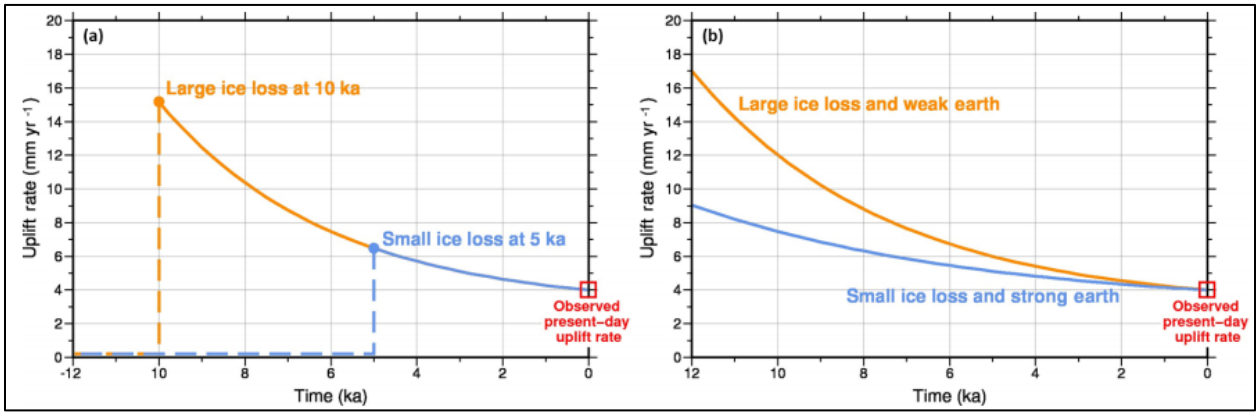


**Figure 4.** Postglacial isostatic rebound rate over time. Shown with a) comparisons of varying ice thickness and b) comparisons of varying ice loss and rheological strength which shows the exponential decay of rebound rates over time (from Whitehouse, 2018).

In North America the current rates of GIA are greatest where ice was thickest (Figure 5). Current rates of isostatic adjustment are greatest just east of the Hudson Bay (Paulson et al., 2007) where the center of mass of the LIS was located during the late-Wisconsinan (Peltier, 1989). In the interior of North America in the Red River Valley, the adjustments occurring along the axis of the valley show signatures of both rebound and collapse (Figure 6).

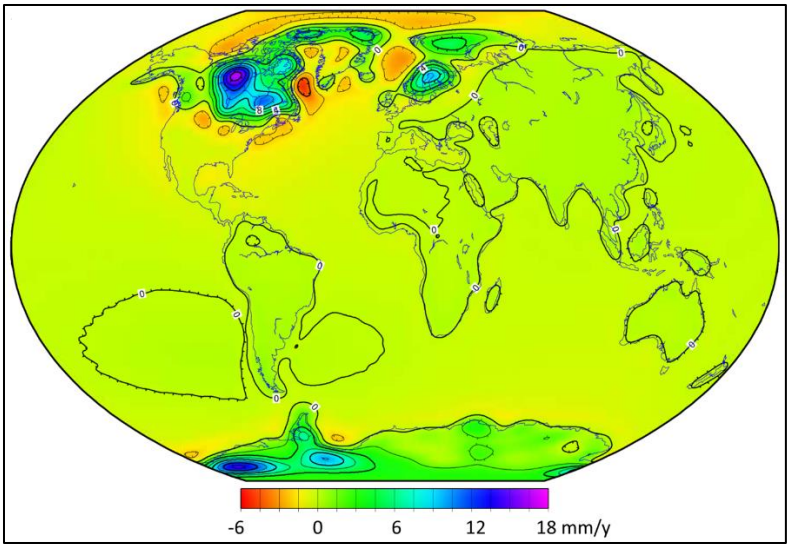


**Figure 5.** Current rates of Glacial Isostatic Adjustments. Rates based on satellite remote sensing data (from Paulson et al., 2007). Current rates are greatest (~18 mm/yr) east of the Hudson Bay where the LIS was thickest during the late-Wisconsinan glaciation. Surrounding areas of rebound, forebulge collapse is active with rates up to ~6 mm/yr.

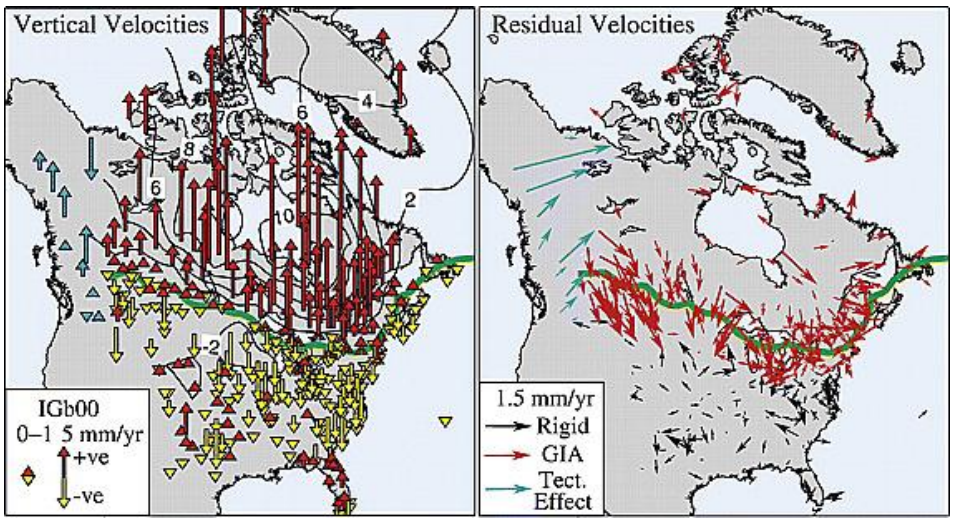


**Figure 6.** Vertical and horizontal isostatic adjustment velocities of North America (from Sella et al., 2007). Vertical velocities in the Red River Valley are –2 mm/yr in the southern valley and +1 mm/yr in the northern valley.

In the Red River Valley, Lake Agassiz's existence during the initial period of isostatic rebound was important in recording the early stages of land-surface adjustments. Beach strandlines, considering their horizontal deposition and current upward tilt to the north, can be used to reconstruct the paleotopography when a given strandline was deposited (Leverington and Teller, 2003). Using these reconstructions in combination with rebound rate data we can estimate

the effects of GIA on landscape and river evolution since glaciers and Lake Agassiz have receded from the Red River Valley.

### *Postglacial landscape evolution at ice sheet margins*

In continental settings, areas at the margins of ice sheets are typically subjected to glacial deposition (Brown et al., 1998; Colgan et al., 2003). Deposition during the last glacial period filled valleys and produced relatively flat, low relief till plains with hydrologically isolated pothole lakes at their heads (Lai and Anders, 2018). As glacial ice melted, glacial outburst floods created rapid incision events (Lord and Kehew, 1987; Leverington and Teller, 2003; Belmont et al., 2011; Hajic, 1990; Wayne and Thornbury, 1951) as meltwater ran off over a land surface adjusting to a new isostatic equilibrium (Koppes and Montgomery, 2009; Belmont et al., 2011; Gomez and Livingston, 2012; Gran et al., 2013; de Quay et al., 2018).

Over time, landscape evolution and incision rates decrease as knickpoints propagate upstream (Gomez and Livingston, 2012; Gran et al., 2013). Incision leaves behind elevated terraces such as those observed on the Le Sueur River in Minnesota, USA that can be age-dated to track the progression of incision through valleys and watersheds (Figure 7) (Gran et al., 2013). The Le Sueur River, incising through glacial till, is best modeled as a detachment-limited system rather than a transport limited system. Behavior as a detachment limited system means that any material detached from the bed or banks of the river will be transported and the glacial till erodes similarly to a weak bedrock due to its overconsolidation (Boulton and Paul, 1976; Gran et al., 2013; Lai and Anders, 2018).

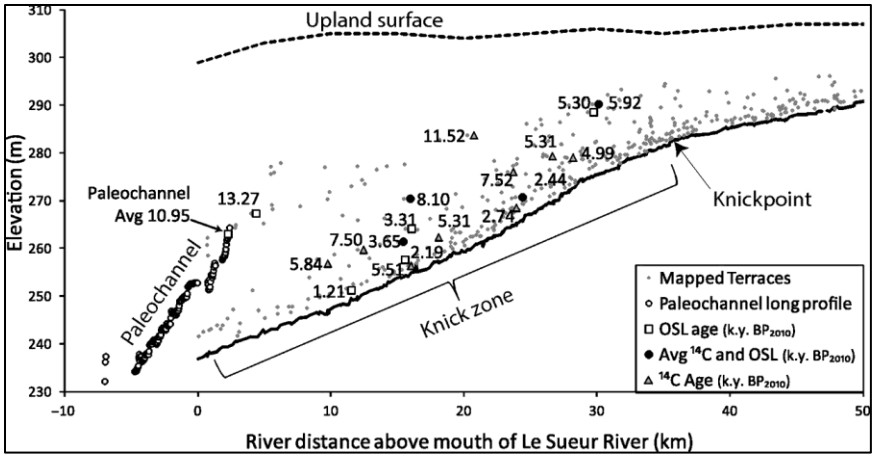


**Figure 7.** Le Sueur River terrace elevation and dates. Terraces were age-dated to track the upstream progression of knickpoint migration through the postglacial river valley (from Gran et al., 2013). Terraces at a greater elevation in relation to the modern river elevation are typically older, while terraces similar to the modern river's elevation have formed more recently.

In areas not effected by glacial meltwaters and outburst floods, the initial stages of landscape evolution begin as disconnected ponds and integration of traditional drainage patterns takes longer (Lai and Anders, 2018). The ways disconnected ponds contribute flow to rivers was investigated through numerical modeling using a Landscape Evolution Model, and findings displayed the importance in variations in overland or subsurface flow and the rate of incision (modeled as the fluvial incision coefficient, *K*) (Lai and Anders, 2018). Figure 8 shows the results of network integration (as a percentage of total domain area) and the net erosion rates given different incision rates and hydrologic connectivity.

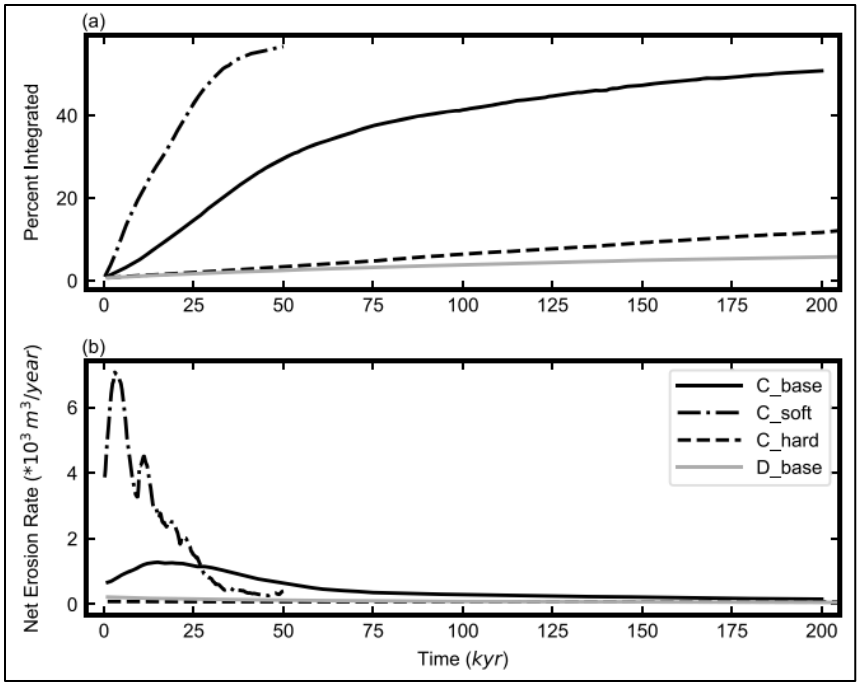


**Figure 8.** Modeled landscape integration and net erosion rates (from Lai and Anders, 2018). Three scenarios C_base, C_soft, and C_hard show connected hydrology where flow overtops pools and contributes to overland flow, incision, and eventual network integration (with K = 0.0001, 0.001, and 0.00001, respectively). The D_base scenario shows a case where precipitation contributes to groundwater rather than runoff, and has a incision coefficient of K = 0.0001. Integration occurs most rapidly, causing the most erosion, in the case of hydrologic connectivity and a low K-value.

In the Red River Valley, during the period when postglacial rivers to the south were incising from meltwater releases the valley was inundated by Lake Agassiz. Landscape evolution outside of the valley has proceeded similarly to the case of the Le Sueur, with incision through glacial tills, but in the Red River Valley incision has been dampened by thick, resistive, glaciolacustrine clay sediments (Brooks, 2003a). The dampening of incision from resistive sediments and lack of meltwater floods has led to the Red River's slow development of a valley up to 15 meters deep (Brooks, 2003b; 2005).

The Red River's geomorphic development, and the Red River Valley's landscape evolution, is largely controlled by meandering and incision (Brooks, 2003b). Over the history of the Red River since its original establishment ~8.5 ka in Southern Manitoba meandering rates

have slowed. Initial meandering rates were 0.35 m/yr between ~7.9 ka and 7.4 ka, decreased to 0.18 m/yr between ~7.4 ka and ~6.2 ka, and have remained between 0.04 and 0.08 m/yr since ~6.2 ka (Brooks, 2003b). In regard to incision, since ~8.1 ka the Red River has only been incising 0.4 to 0.8 m/ky, leading to very slow valley development (enlarging of 0.7-2% over the last 1000 years) (Brooks, 2003b).

***Meandering river erosion***

The meandering river is ubiquitous in terms of river planforms, especially in low-relief landscapes (Howard, 2009). Meandering rivers typically are associated with low valley slopes and transport sediments as suspended load (Schumm, 1985). The meandering river planform arises from helicoidal flow patterns in the channel that are brought on by centripetal acceleration and the effect of friction at varying depths (Dietrich, 1987). In meander bends, flow near the top of the channel is less effected by the overlying weight of water and thus flows laterally toward the outside bank (Figure 9) (Blanckaert and de Vriend, 2004). The momentum toward the outer bank creates a pressure gradient across the channel which causes superelevation of the outer bank and flow at the bottom of the channel to circulate toward the inner bank (Knighton, 1998).

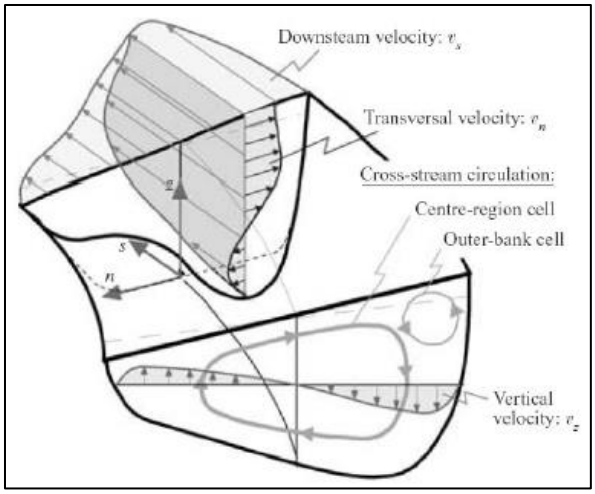


**Figure 9.** Secondary flow characteristics in meander bends. Secondary flow circulation results in helicoidal flow (from Blanckaert and de Vriend, 2004).

In meandering rivers, the distribution of shear stress is produced by flow patterns in addition to channel depth. Shear stress at the outer bank is typically large compared to inner banks because of a greater flow depth and downstream gradient (Markham and Thorne, 1992). The area of the greatest shear stress is usually found just downstream of the bend apex where secondary circulation is greatest (Figure 10) (Ursic et al., 2012). Helicoidal flow weakens as flow exits bends and is dissipated prior to entering the next downstream bend, but strengthens again as it flows around the next bend.

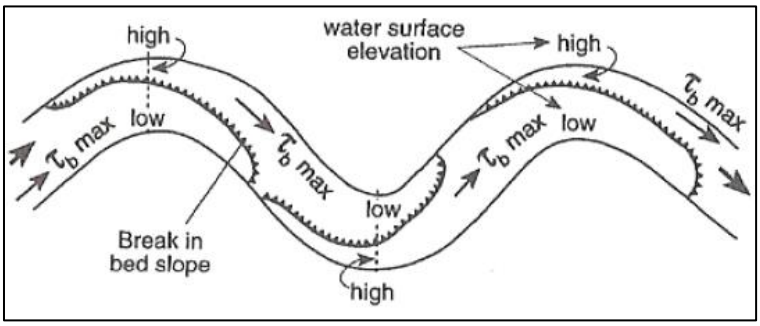


**Figure 10.** Bed shear stress distribution in simplified meandering channels (from Knighton, 1998). The greatest shear stresses are found at the outer bank downstream of the bend apex where the water surface is superelevated. Lower shear stress is present at the inner banks of bends, where flow is slow and the channel is shallow.

In meandering rivers, erosion occurs at the outer bank of meander bends while deposition occurs at the inner bank (Hooke, 1975). Erosion at the outer bank occurs as a two-step process.

Bank undercutting at the outer bank occurs until a bank failure occurs, supplying material to the bank toe. In temperate or polar environments, freeze-thaw processes can also contribute to the accumulation of material at the bank toe (Kelly and Belmont, 2018). Then, only when the fluid shear stress exceeds the critical shear stress of the material at the toe is that material entrained and transported (Thorne 1991; Constantine et al., 2009; Schwendel et al., 2015). Bank erosion processes vary in space and are affected by the local shear stress distribution (Sin et al., 2012; Ursic et al, 2012) curvature of meander bends (Ippen et al., 1962), the relative resistivity of bed and bank sediments (Hicken and Nanson, 1984), characteristics of helicoidal flow (Blanckaert and de Vriend, 2004; Camporeale et al., 2008) and vegetation (Shields et al., 2009).

As erosion processes continue over time, meander bends migrate. The spatial variations in meandering processes change in relation to long term shifts in regional- and watershed-scale inputs such as changes in valley slope (Schumm, 1977; Schumm, 1985; Holbrook and Schumm, 1999; Piégay and Schumm, 2003), sediment input, climate change resulting in hydrologic or ice regime changes, and vegetal growth. Changes in any of the inputs above result in responses in river planform and sinuosity (Schumm, 1985). Sinuosity responds to changing inputs through meandering. Meander bends can grow by translating up or downstream, rotating, extending outward, or by lobing and compound growth (Figure 11).

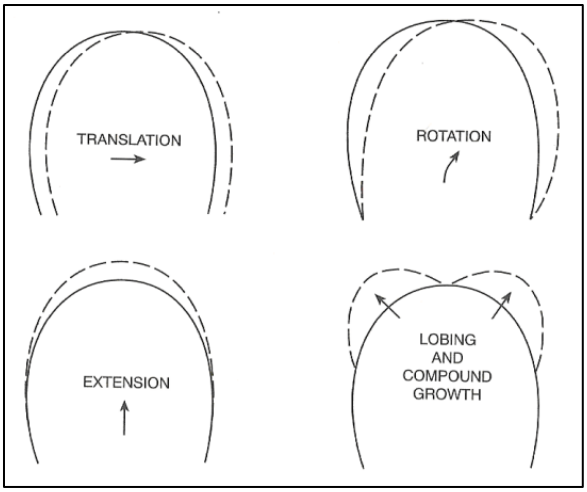


**Figure 11.** Meander growth processes (from Knighton, 1998). Bends evolve by four main mechanisms including translation, rotation, extension, and lobing/compound growth.

Meander bend growth sometimes results in the formation of meander cutoffs. Meander cutoffs temporarily decrease sinuosity (Schumm, 1969; Schumm, 1977; Schumm, 1986; Holbrook and Schumm, 1999; Hooke, 1995), cause other nearby meanders to erode (Camporeale et al., 2008), release sediment into the river (Zinger et al., 2011), and produce oxbow lakes (Constantine and Dunne, 2008). Meander cutoffs form either by the intersection of two adjacent meander bends (neck cutoffs) (Figure 12) (Hooke, 2003; Schwendel et al., 2015).

or by overland flow and the erosion of a chute (chute cutoffs) across the neck connecting two meanders (Figure 13) (Gay et al., 1998; van Dijk et al., 2014).

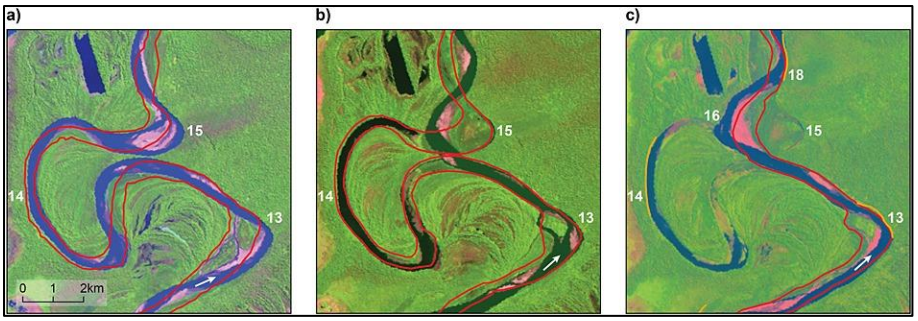


**Figure 12.** Evolution of a neck cutoff on the Rio Beni (from Schwendel et al., 2015). Progression from left to right shows the intersection of two adjacent meander bends and eventual cutoff resulting in the formation of an oxbow lake.

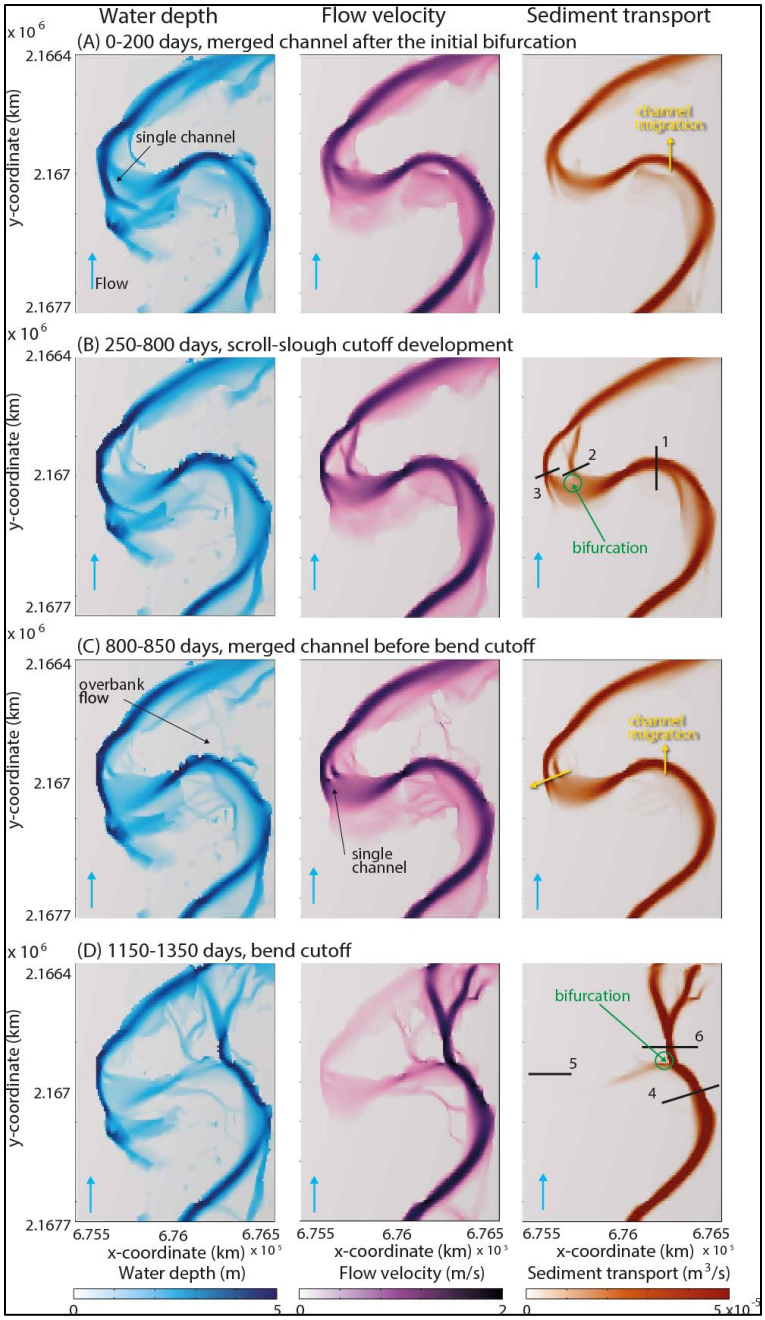


**Figure 13.** Development of a chute cutoff in an experimental setting (from van Dijk et al., 2014). Chute cutoff progression (top to bottom) shows initial development of a bifurcation and subsequent overland flow resulting in the erosion of a chute across the neck between meander bends.

### *Mobile ice erosion processes in fluvial systems*

Although the LIS has receded from the North American continent, ice is still a major contributor to erosion in most postglacial rivers. In some cases ice is noted as the dominant process in driving erosive processes in mid- and high-latitude landscapes and rivers that freeze for a period of the cold season (Lawler, 1993; Smith and Pearce, 2002; Beltaos et al., 2018; Payne et al., 2018) because the greatest amount of sediment is mobilized from hillslopes and carried by rivers during the snowmelt and ice thaw period (Walker, 1959; Milburn and Prowse, 1996; 2002; Barnes et al., 2016). Ice causes erosion throughout the winter and transition into spring, when the breakup- and floe-related processes of anchor and bankfast ice heaving and rafting (Reimnitz et al., 1990; Kempema et al., 1993; Kempema and Ettema, 2011; Kalke et al., 2017), pressurized flow under ice (Wankiewicz, 1984; Ettema, 2006), grounded and hanging ice dams/jams (Turcotte et al., 2011; Carr and Vuyovich, 2014; Turcotte et al., 2017; Beltaos, 2018; Lindenschmidt et al., 2018), and abrasion by mobile ice (Borland, 1959; Smith, 1979; Doyle, 1988; Brooks, 1993; Wuebben, 1995; MacKay and MacKay, 1977; Lotsari et al., 2015).

During breakup, river ice is mobilized by hydraulic forcing and thermal decay (Gray and Prowse, 1993; Beltaos, 1997, 2003). During their initial mobilization river ice contributes to bank erosion by heaving sediment from the banks (Ettema, 2002; Zabilansky, 2002). After mobilization, river ice largely matches the flow dynamics of surface water (Browne et al., 2019). Because of this, river ice is subject to the same bottlenecking effects and centrifugal forces that flowing water experiences, which can result in ice jams and bank abrasion in river bends or areas of channel with narrow widths (Smith and Pearce, 2002).

Ice jams create temporary dams that have adverse effects on erosion. Upstream of an ice jam, flow velocities are temporarily reduced and flooding causes deposition of any transported

sediment (Eardley, 1938; Moore and Landrigan, 1999). River ice jams can form anywhere on a river, but channel constrictions (Andres et al., 2005), meander bends (Sui et al., 2008), islands, confluences (Tuthill and Mamone, 1997; Ettema and Muste, 2001), and man-made structures (Knack et al., 2010) are all features commonly associated with ice jams (Beltaos, 1995; Turcotte et al., 2011). When ice jams occur on meandering rivers, flooding can lead to gullying and scour on floodplains which contributes to the formation of chute cutoffs (Smith and Pearce, 2002). These dams usually form at the entrance of bends where flow is concentrated toward the outer bank, causing damming that floods across the neck of bends and requires multiple ice jam floods to cut off the meander bend (Figure 14).

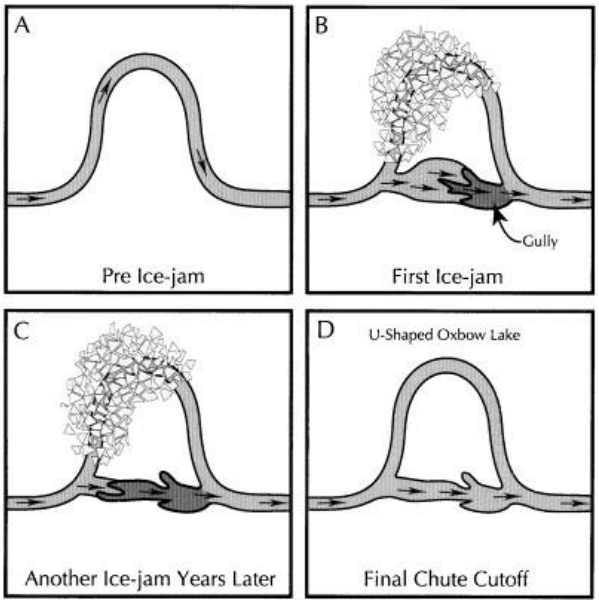


**Figure 14.** Progression of ice jam chute cutoff process (from Smith and Pearce, 2002). Ice accumulates at the outer bank at the entrance to the bend and causes flooding and gullying across the neck of the cutoff. Repeated ice jams in the same area cause eventual cutoff of a meander.

Gouging and abrasion processes contribute to meandering and meander cutoff processes by expediting erosional processes during the transition from winter to spring (Ettema, 2002), but the degree to which gouging and abrasion contribute to erosion is currently unknown (Beltaos, 2018). Channel geometries that are most significantly affected by mobile river ice are sinuous point bar channels, sinuous braided channels, and braided alluvial channels (Ettema and

Zabilansky, 2004). In channels where bank gouging and abrasion is significant, banks are steepened above the waterline (Prowse, 2000), features extending into the middle of the channel are smoothed by seasonal ice floes (Ettema, 2002), and bank vegetation is stripped away (Prowse and Culp, 2003).

# CHAPTER II: AUTOMATED MEANDER CUTOFF MAPPING, CUTOFF DISTRIBUTION, AND CONNECTIONS TO RIVER MORPHOLOGY AND PALIMPSEST CONDITIONS


## Abstract

The Red River (of the North) drains a portion of the low-relief, ice marginal, post-glaciolacustrine Central Plains into Lake Winnipeg. Meander belt topography along the Red River was analyzed using geomorphometric techniques to compare fluvial landforms to extents of late-Wisconsinan deposits of the Laurentide Ice Sheet. Specifically, a high-resolution digital elevation model (DEM) and a new semi-automated workflow was used to map the number and extent of meander cutoffs. Summary statistics and maps describe the relation between the cutoff distribution, lithology, sinuosity, slope, and incision along the river. A new variable called Incision-Normalized Relief (INR) accounts for the positive relationship between river incision and cutoff relief and provides a framework for further interpretation of the effects of lithology and palimpsest conditions on river meandering. Results suggest the spatial distributions of slope, relict glacial landforms, and glaciolacustrine sands have influenced and continue to influence differential incision and, hence, the spatial distribution and relief patterns of meander cutoffs along the Red River. This work provides a new method of mapping meander cutoffs at the river scale and exemplifies the ways in which the distributions of meander cutoffs can be interpreted against attributes such as lithology, river incision, sinuosity, and slope.

## Introduction

Rivers established in low-relief landscapes display morphologic variability over relatively short distances due to variations in alluvium composition (Güneralp and Rhoads, 2011; Schwendel et al., 2015, Bogoni et al., 2017), slope (Schumm, 1977), sediment input (Schumm, 1968; Constantine et al., 2014), hydrology (Schumm, 2007), tectonic motions (Piégay and Schumm, 2003), and biologic/human alterations (Schumm and Winkley, 1994). In postglacial landscapes, variations in river morphology are often linked to lithologic variations in/between glacial deposits (Phillips and Desloges, 2014; 2015), base-level change, and tectonic motions from Glacial Isostatic Adjustments (GIA) (Teller and Leverington, 2004; Sella et al., 2007; Gowan et al., 2016). A meandering river's response to those variations is recorded in the floodplain landscape and deposits after alteration by processes such as meandering and meander cutoff (Arbogast et al., 2008; Constantine et al., 2010), channel avulsion (Cook, 2018), incision (Gran et al., 2013), aggradation (Stewart and Desloges, 2014), and flood deposition (Gendaszek et al., 2012).

Meander cutoffs are classified by the processes by which they are formed (i.e. neck or chute cutoffs). Loop or neck cutoffs occur by the outward erosion and intersection of adjacent meander bends (Gagliano and Howard, 1984; Constantine and Dunne, 2008; Van Dijk et al., 2014). Loop or neck cutoffs form by the fundamental process of meandering, in which outward erosion is driven by helicoidal, secondary flow acting on the outer bank of meander bends (Camporeale et al., 2008) leading to the elongation and eventual intersection of neighboring bends as erosional perturbations propagate up- and downstream. Chute cutoffs form by scour, incision, or headcutting between the up- and downstream ends of adjacent bends (Johnson and Paynter, 1967; Gay et al., 1998; Peakall et al., 2007, Constantine et al., 2010, Grenfell et al.,

2012). Chute cutoff formation can be partially caused by downstream flow restrictions from woody debris or ice jams (Keller and Swanson, 1979; Gay et al., 1998; Smith and Pearce, 2002; Constantine et al., 2010), channel bars (Bridge et al., 1986; Li et al., 2019), changes in bend orientation from blockages, or restriction from resistive cohesive material (Lewin and Brindle, 1977).

The formation of a meander cutoff initiates dynamic instabilities in meandering rivers (Camporeale et al., 2008), controls the production of oxbow lakes (Constantine and Dunne, 2008), causes the release of sediment pulses (Zinger et al., 2011), and temporarily decreases the local sinuosity (Schumm, 1969; Schumm, 1977; Schumm, 1986; Holbrook and Schumm, 1999; Hooke, 1995). Fluvial landscape features like meander cutoffs create sediment variations along floodplains which can be preserved for millions of years (Harden, 1990), making them significant features to consider when interpreting past geomorphic settings and how rivers have responded to periods of shifting equilibriums (Peakall et al., 2000; Kasai et al., 2001; Hooke, 2004; Toonen et al., 2012; Gran et al., 2013).

In single-thread meandering rivers, new meander cutoffs (oxbows) become sediment sinks along the floodplain landscape. Sediment deposited in an oxbow is supplied by a main channel through a connecting tie-channel (Rowland et al., 2005) or by intermittent overbank floods (Wolfe et al., 2006; Oliva et al., 2016). Sedimentation in the cutoff decreases the relief of meander cutoffs as they age among the landscape until lateral meandering or periods of sustained floodplain aggradation erase them from floodplain topography (Gore and Shields, 1995). While cutoff features commonly occur on meandering rivers around the world, relatively undeveloped, slowly evolving rivers offer a unique opportunity to study fluvial landscapes prior to major, topography-erasing secondary processes. Well-developed rivers, or those in never-glaciated

areas, have likely meandered over their histories to effectively cover up the cutoffs that were recorded earlier in their histories. Therefore, studying recently established, slowly evolving rivers provides a good record of how morphologic variations are established and preserved in fluvial topography.

The overall goal of this study was to build on the current manual methods of mapping and interpreting the distribution of meander cutoffs at the river scale, for which studies have traditionally used historical satellite/air photos and maps (Lewis and Lewin, 1983). Methods developed here map cutoffs at the river scale using a semi-automated procedure, and the resulting spatial distribution of cutoffs, relief, and the newly recommended INR variable were used to support geomorphic interpretations of the postglacial, unconfined, meandering Red River in connection to palimpsest lithology and glaciostatic adjustments.

**Postglacial rivers in the Holocene**

Studies of Holocene fluvial records of mid-latitude rivers have complications in identifying erosional trends post-glaciation (Starkel, 1991; Knox, 1995). Such complications arise from combinations of postglacial fluvial processes tied to deglaciation (Cordier et al., 2017), climate change (Knox, 2000; Macklin et al., 2012), GIA-induced tectonic movements (Nanson, 1980), and human impact (Macklin, 1999). With deglaciation, GIA, and base-level changes, many postglacial rivers have incised into a landscape of complex glacial deposits that make up relatively low-relief landscapes (Phillips and Desloges, 2014; Lai and Anders, 2018). The legacy effect of former glaciers and their deposits persist for long periods, which is evident in both modern examples (Curran et al., 2017) and those dating back to Pleistocene glaciation (Lewis and Lewin, 1983; Phillips and Desloges, 2014; 2015).

### *Exit Glacier's modern control on river morphology*

Curran et al. (2017) recorded a modern example of how landforms left behind by modern melting glaciers affect river morphology, which displayed how variations in river morphology are established soon after deglaciation. Exit Glacier (Alaska, USA) has been receding since the early-1800's (Wiles and Calkin, 1994, Cusick, 2001), and during its retreat has left behind moraines that were noted to cause variability in the morphology of the meltwater channel (Curran et al., 2017). The meltwater channel is braided over much of its length but reaches flowing over moraines were recorded as being single thread, reverting to a braided pattern downstream before being bottlenecked by the next, downstream moraine.

The influence of those moraines was also evident in the sediment load of the channel, with relatively more sediment being supplied to the channel in reaches flowing over moraines. That additional sediment being added to, and carried through, moraine reaches was deposited downstream, causing aggradation of the downstream reaches. Over time, the effect of the glacier and its sediments on river morphology have waned, which is evident in the more permanent channel locations observed with increasing distance from the modern glacial extent (Curran et al., 2017).

### *Rivers of Wales and the Borderlands*

Meander cutoff distribution was studied by Lewis and Lewin (1983) for 14 of the larger rivers in Wales and the Borderlands totaling 964 km of river, finding a total of 145 cutoffs using a series of historic maps and air photos (0.15 cutoffs $km^{-1}$). Many of the rivers included in that study are examples of postglacial rivers bound by valley walls in their uplands, but transition to broad unconfined lowlands downstream. Rivers like the Usk and Wye were found to exhibit few

cutoffs due to being located almost entirely in confining valleys. Others, like the Rheidol, Severn, Teme, and Tywi, have clusters of cutoffs as the rivers transitioned from the more confined, high slope, low sinuosity uplands to the unconfined lowland reaches.

The location of meander cutoffs in Lewis and Lewin (1983) was also reliant on the character of meandering, with areas of extending, translating meander loops displaying clustered cutoffs while straighter, more actively meandering reaches produced few cutoffs. Reaches were also classified by sinuosity and stability, showing that meander cutoffs tended to form in high sinuosity, actively meandering reaches (0.355 cutoffs $km^{-1}$), while high sinuosity, stable reaches (0.080 cutoffs $km^{-1}$) produce a lower number of cutoffs per length that is similar to low sinuosity reaches (0.071 cutoffs $km^{-1}$) (Lewis and Lewin, 1983).

***Rivers of peninsular southern Ontario, Canada***

The rivers of peninsular southern Ontario are examples of low relief, postglacial and post-glaciolacustrine rivers established atop a thick mantle of Pleistocene glacial sediments including sandy sub-glacial tills and ice contact moraines, outwash, and glaciolacustrine clays (Phillips and Desloges, 2014). On that low relief landscape, the most prominent landscape features are erosive scarps and moraines deposited 12-13 ka BP (Barnett et al., 1998). Although they are low relief landforms, the moraines were found to have a modern influence on specific stream power (Phillips and Desloges, 2014), contributing to specific stream powers that were up to five times as high as in reaches established on till or glaciolacustrine plains (Phillips and Desloges, 2015). The increase in stream power near moraines was associated with variations in channel geometry and locally high slopes (Phillips and Desloges, 2015).

The moraines were also found to influence the morphology of downstream reaches, causing variations in sediment load through the contribution of coarse material to the overall load (Thayer et al., 2016). The variations found in these studies show that the effects of glaciers, and their deposits, on rivers are persistent among low relief landscapes for at least 12-13 thousand years, even in areas that have experienced inundation by postglacial lakes.

**Physical setting**

Established in the interior plains of North America northward of the margin of the Des Moines Lobe of the Wisconsinan Period Laurentide Ice Sheet (LIS) (Figure 15a) on the low slope, low relief former bed of Lake Agassiz, the 885-km long Red River flows north from the confluence of the Bois de Sioux and Otter Tail Rivers with an irregular sinuosity of 2.18, draining ~290,000 $km^2$ of land from the Central Plains of North America into Lake Winnipeg (Figure 15B). Straddling the US-Canada border, the Red River is a mid-latitude river north of the LGM margin with a low slope of 0.00014 (14 cm $km^{-1}$) (Brooks, 2017) and is incised relatively little (~15 m in southern Manitoba) (Brooks, 2003b).

The entire Red River Valley was periodically inundated by Lake Agassiz, and aside from its initial filling and final draining water levels fluctuated mostly between the high-water line of the Campbell Stage and temporary low-stand of the Moorhead Stage (Figure 15c; Dilworth and Fisher, 2018). The fluctuating lake levels led to a wide range of thicknesses of the resulting glaciolacustrine clay deposits, ranging from 10-80 m (Remenda et al., 1994). In the areas where surficial geology is not dominated by glaciolacustrine deposits, the Red River flows atop the wave-planed late-Wisconsinan Edinburgh Moraine (Figure 15d) that has been mixed with clay/silt lake sediments (Harris et al., 1974; Clayton and Moran, 1982; Harris, 1987). Upstream

(south) of 47°N, the Red River is established atop a mix of glaciolacustrine clays and sands (some aeolian) from the Sheyenne River Delta (deposited during the period of Lake Agassiz) and late-Wisconsinan Comstock Moraine (Figure 15d).

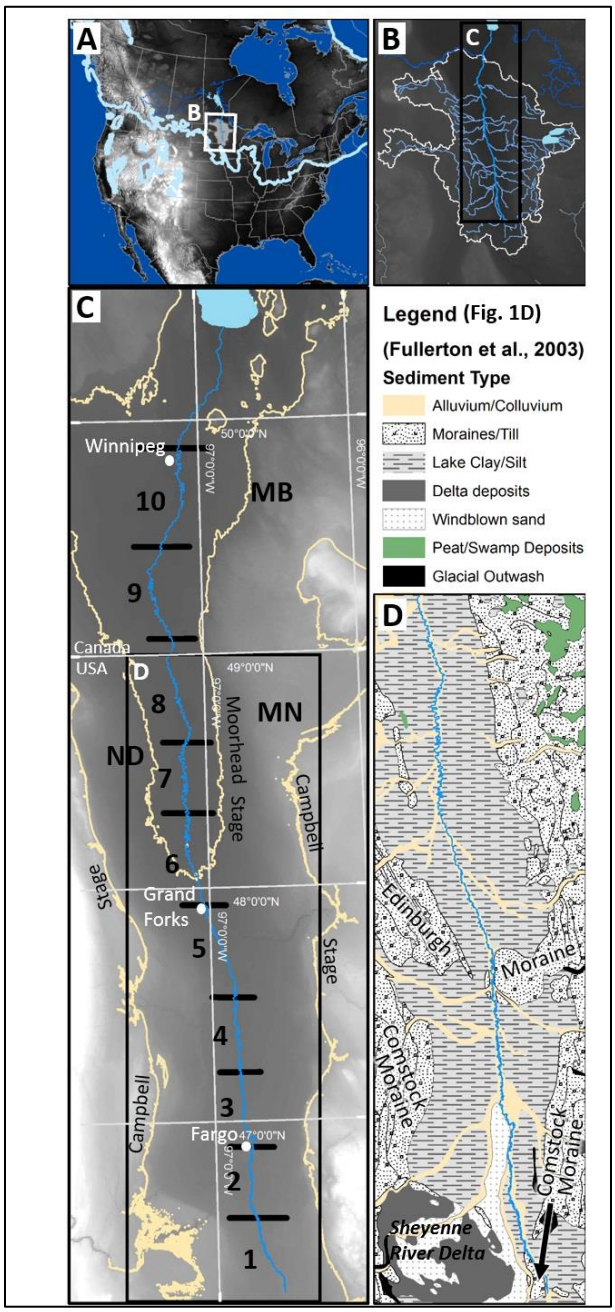


**Figure 15.** Red River study area maps. Shown are A) the location of the study area in North America, north of the LIS LGM margin (Ehlers et al., 2011), B) the Red River Basin and contributing rivers, C) the path of the Red River, topography of the Red River Valley, Campbell and Moorhead Stages of Lake Agassiz, cities, and reach divisions, and D) the surficial geology of the Red River Valley

Consolidated clays deposited by Lake Agassiz have higher erosional thresholds and require greater critical shear stresses or flow velocities for their entrainment in comparison to sandy units (Constantine et al., 2009). Areas where clay units extend well below the base-level of the Red River are typically located in low-slope reaches where the river produces shear stresses that are lower than the threshold for erosion. Clay resistivity and low fluid shear stresses each lead the dampening of incision in clay-rich reaches, leaving the marginally sandier reaches to be relatively more erosive and allow some incision.

After the draining of Lake Agassiz abrupt channel shifts were most common due to rapid GIA and high sediment supply, but over time GIA slowed (Gowan et al., 2016) and Red River meandering slowed (Brooks, 2003). The area in which the Red River was established was last fully inundated by Lake Agassiz ~10 ka (Dilworth and Fisher, 2018). By 7.9 ka Lake Agassiz had receded from the study area and, in southern Manitoba, the Red River had established a single-threaded, meandering channel (Brooks, 2003). From 7.9 to 7.4 ka cal BP the lateral erosion rate of meandering, as exemplified by a pair of meanders in southern Manitoba, was ~0.35 m $yr^{-1}$. The rate decreased to ~0.18 m $yr^{-1}$ between 7.4 and 6.2 ka cal BP and slowed further to 0.04-0.08 m $yr^{-1}$ from 6.2 ka cal BP to present (Brooks, 2003). Among meandering rivers, the Red River is known to have comparatively low meandering rates due to its low stream power, cohesive silt banks, and overbank aggradation (Brooks, 2017). Ultimately, the resistive clay-rich sediments, low erosion rates, and recent date of establishment (~7.9 ka) cause the modern Red River to have a relatively simple meander-belt topography exhibiting little incision, few paleochannels, meander cutoffs, and no meander cutoff stacking.

## Methods and spatial data

To improve on methods of cutoff mapping based on manual surveys of maps and air/satellite photos, a set of semi-automated GIS methods were developed to determine the location, extent, and relief of meander cutoffs using high-resolution topographic data. An example of how the methods are applied, and how the resulting meander cutoff distribution can be used to support geomorphic interpretations, is presented below. The surficial geology (Fullerton et al., 2003) is used in the results and discussion sections for the interpretation of results. Required inputs for the analyses included high-resolution DEM's and a channel centerline for the study area (National Hydrography Dataset, 2010). This study used a 3-m DEM for the American Portion (International Water Institute, 2010), a 5-m DEM for the Canadian portion (Manitoba Conservation, 2005a; 2005b), and a 10-m DEM of the entire river for the analyses (USGS, 2017).

### *Meander cutoff mapping*

Meander cutoffs were mapped using a geomorphometric methodology for analyzing high-resolution DEM's in ESRI ArcGIS Desktop 10.7. These methods require input of a high-resolution DEM and a channel centerline file and output a set of vector polygons representing meander cutoffs. A Local Relief Model tool (Bofinger and Hesse, 2011; Novák, 2014) designed for use in Archaeological studies is applied along with other readily available tools in ArcGIS 10.5 to map cutoffs (Figure 16). The fully automated tool, known as MC Mapper, is available on the author's website (https://zphillipsgeo.weebly.com/), by email, and in script in Appendix A.

The high-resolution DEM was clipped to a buffer of the river centerline so that only the near-channel floodplain topography was further analyzed. In this case, an iterative procedure was

used to select a 1500-m buffer of the channel centerline that sufficiently included all relevant meander cutoff topography. The near-channel DEM was smoothed to filter small topographic features from the DEM. This smoothed, clipped DEM was then input to the LRM Tool (Bofinger and Hesse, 2011; Novák, 2014).

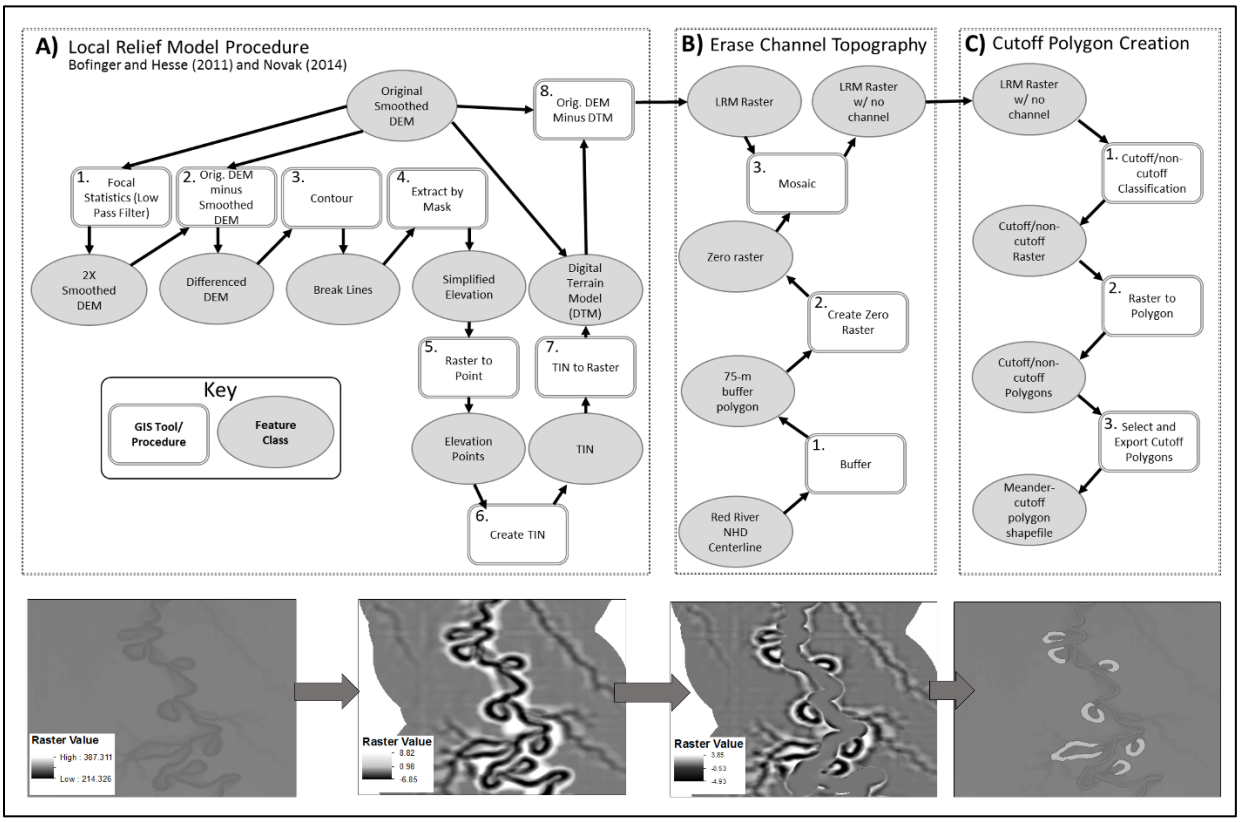


**Figure 16.** Diagram of the cutoff mapping procedure. Part A shows steps applied in the LRM Tool (Bofinger and Hesse, 2011; Novák, 2014), Part B erases the channel topography and makes cutoff classification more accurate, and Part C converts LRM raster values to discretely mapped polygons.

The LRM Tool (Figure 16, section A) enhances topographic features of the DEM while removing the trend of valley slope and making the topographic signature of all the meander cutoffs uniform over the length of the river. The LRM Tool smooths the input DEM, subtracts the resulting smoothed DEM from the input DEM, and then contours the difference raster. The LRM Tool then transforms those contours into points and uses the contour points as breaklines to create a TIN. Finally, the TIN was converted to a terrain raster and that terrain raster was

differenced from the input DEM to create the final LRM raster. Because the LRM values for the channel and cutoffs are similar, the modern channel topography was removed from the LRM raster. It was determined that a 75 m buffer from the centerline sufficiently covered the width of the modern channel without erasing meander cutoff topography. A constant zero raster was created within this buffered area, and the zero raster was mosaicked to the LRM raster (Figure 16, section B). This step made the classification of topography better at distinguishing meander cutoff topography from modern river and non-cutoff topography.

Next, the LRM raster was converted into polygons so that meander cutoffs were discretely mapped (Figure 16, section C). The Image Classification Toolbar was used to isolate meander cutoff topography from other meander belt areas. One sample of LRM raster values was gathered from a number of spatially dispersed meander cutoffs, and another sample of LRM values was taken from all topography not representing cutoffs. The LRM raster was classified based on those sample values and the resulting classified raster was converted into polygons signifying the meander belt topography. The meander belt topography polygons that were not initially classified as cutoffs were deleted and that set of polygons was thinned until the only remaining polygons were those representing meander cutoffs. Cutoffs were only included in the count if they were entirely separated from the modern channel (i.e. chute or loop/neck cutoffs), excluding partial cutoffs and instances of channel shifting. Additionally, polygons were surveyed for quality and accuracy and polygons not accurately representing meander cutoffs were manually edited to best represent the extent of the cutoff to remove extra areas of secondary drainage that were classified as meander cutoff polygons, which was conducted only to improve the accuracy of the relief calculations. Accurate extents were unattainable for some of the cutoffs

in areas of urban development or relatively complex fluvial topography, but because of manual editing imperfect extents did not further complicate the relief calculation.

### *Geomorphic attributes*

Channel sinuosity for the Red River was calculated for ten equal lengths of river (further referred to as reaches) and compared to the cutoff count, cutoff density (cutoffs per length of channel), incision, slope, mean cutoff relief and incision-normalized relief (INR). The sinuosity was calculated by dividing the flow length by the direct distance between the beginning and end of each of the ten equal length reaches as to avoid selection bias. The count of Cutoff counts per flow length were calculated for each reach for comparison to each of the other reaches.

Meander cutoffs were overlain on the profiles for channel and floodplain elevation to compare the meander cutoff distribution to slope and incision over the length of the river. The channel elevation profile was created by extracting elevations from the DEMs to points spaced at 1-km intervals along the river's centerline. The channel slope and elevation profiles were measured using a moving-window average of the extracted elevations. The floodplain elevation longitudinal profile was extracted from a 10-m DEM (Archuleta et al., 2017; USGS, 2017) with a vertical accuracy of less than +/- 3.04 m at 100-m intervals immediately adjacent to the meander-belt (Gesch et al., 2014). Incision was then calculated by subtracting the channel elevation from the floodplain elevation, giving a maximum possible error for the incision of +/- 6.08 m.

***Relief and incision-normalized relief (INR) calculations***

The relief of meander cutoffs was measured by comparing the elevation within meander cutoff polygons to the elevation in a 100-m buffer outside of the cutoff (Figure 17a). Topography within cutoffs sometimes contained modern, incised drainage gullies or urban topography like roads or raised land for buildings or bridges, so the mean elevation of the cutoff was extracted from the DEM to minimize the effect of those features on the elevation calculation. Within the boundaries of most of the cutoff buffers, the actual topography was found to be a misrepresentation of the upper floodplain elevation because most of the buffers contained the topographic signature of parts of the modern channel, paleochannels, roads, railroad beds, buildings, levees, drainage ditches, and tributaries. To correct for the topographic signatures of these objects the maximum elevation was extracted from the smoothed DEM that was originally input to the LRM Tool. Profiles of the smoothed topography versus the actual topography determined that the maximum value of the smoothed buffer elevation best represented the elevation of the actual floodplain (Figure 17b). Meander cutoff relief was calculated by subtracting the mean cutoff elevation from the maximum smoothed elevation of the buffer (representing the upper floodplain). DEM values calculated from each the 3-m United States DEM and 5-m Canadian DEM are accurate to less than +/- 15 cm (Manitoba Conservation, 2005a; 2005b; International Water Institute, 2010), so the maximum possible error for relief values equates to a maximum of +/- 30 cm.

Incision normalized relief (INR) was calculated by extracting the nearest incision value for each cutoff (Figure 17c). Then, the relief for that cutoff was normalized by the extracted incision value. In an ideal scenario this normalization should return INR values between zero and one that compare relief (a product of pre-cutoff incision and post-cutoff sedimentation) to the

total amount of incision. INR values close to zero signify that the total modern river incision is much greater than cutoff relief, which points to a significant base-level drop after cutoff formation. INR values close to one signify that cutoff relief and the total incision are similar (i.e. no change in base-level since cutoff formation).

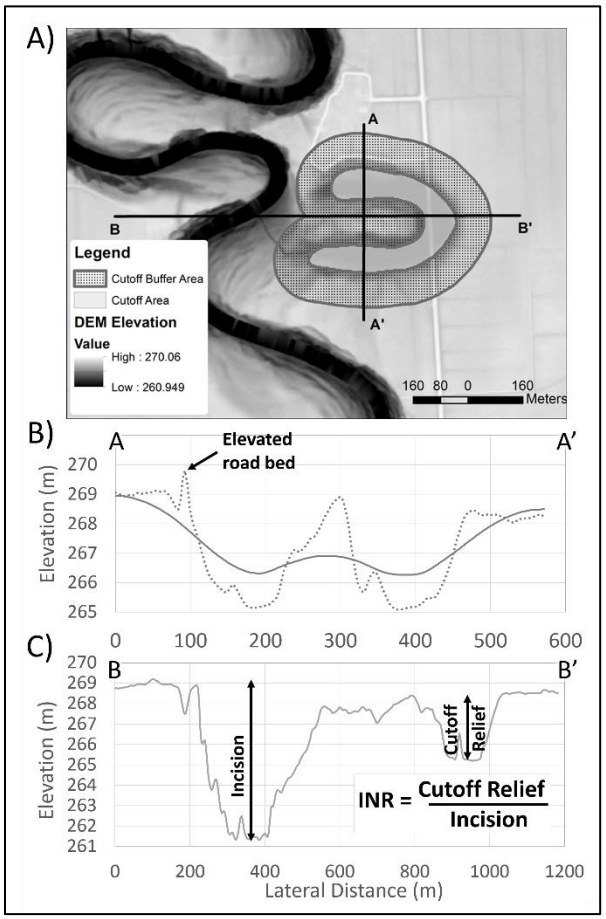


**Figure 17.** Example calculation for relief and INR. Included are the areas and topography for relief and INR calculations showing A) cutoff and buffer polygons, B) elevation profiles prior to (dotted line) and after adjustment of topography by smoothing (solid line), and C) example profiles of topography included in the INR calculation.

Knowing that incision is a slow process on the Red River (Brooks, 2003b), low INR values signify cutoffs occurring soon after river formation (prior to incision) and high values signify the most recently formed cutoffs (after incision, when incision of paleochannel was locally similar to the modern channel). INR values over one indicate instances where cutoff relief is greater than incision, signifying recent cutoff formation (i.e. oxbows), post-cutoff river

aggradation, or human alteration within cutoff topography. INR values over one that were deemed to be because of discrepancies between Canadian and US topographic data are mapped in results but Canadian cutoffs were omitted from further interpretations. With the maximum possible error for incision noted above (+/- 6.08 m) and cutoff relief values ranging from 1.19 to 10.03 m, this leads to INR errors that may possibly range from ~60% to 510% if errors are uniform across the 10-m DEM. In further investigation of this, elevation values were compared between the 10-m and 3-m DEM's in which values did not vary more than ~50 cm between the two DEM's (which suggests that 10-m DEM errors are lower than suggested and that possible INR errors are likely in the 10-100% range).

## Results

The cutoff mapping methods identified 153 of the 158 (96.8%) meander cutoffs on the Red River (0.173 cutoffs $km^{-1}$), which was verified by manually counting the cutoffs that the semi-automated methods failed to map (see Supplementary Data for polygon shapefile) (Figure 18a). Because DEM's of two different cell-sizes were used in the methods do not produce consistent relief calculations, the six Canadian cutoffs were only included in mapping results and were omitted from relief-based interpretations.

### *Cutoff mapping and distribution*

Meander cutoffs have a greater frequency per river length in the upstream reaches of the Red River, with 120 of the cutoffs being located upstream (south) of 48°N in Reaches 1 thru 5 (Figure 18a). In relation to the stages of Lake Agassiz, 127 of the 153 cutoffs are located above 247 m a.s.l., the most recently constrained elevation for the Moorhead Phase (Figure 15c)

(Dilworth and Fisher 2018). By reach, cutoffs have the highest frequency per river length in Reach 3 and lowest frequency in Reach 10. Reaches 1 thru 5 each have more than 20 cutoffs, Reach 6 has 17 cutoffs, and Reaches 7 thru 10 each have fewer than 10 cutoffs (Table 1).

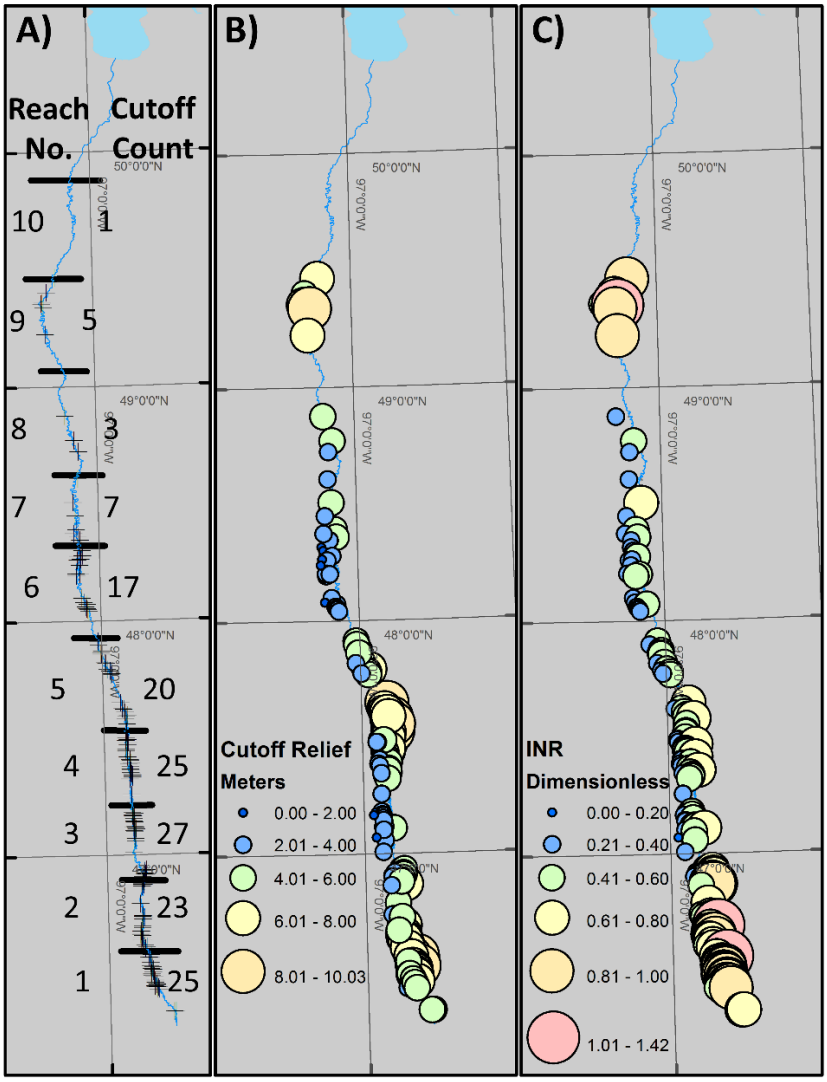


**Figure 18.** Results of cutoff mapping, relief, and INR. Shown are the actual location of cutoffs (A) and, for purposes of displaying all values, shifted results for relief (B) and INR (C).

**Table 1.** Reach summaries and cutoff attributes

| Reach | Cutoffs | Density (cutoffs/km) | Sinuosity | Slope (cm/km) | Mean Incision (m) | Relief (m) | INR |
|---|---|---|---|---|---|---|---|
| **1** | 25 | 0.31 | 2.18 | 18.09 | 6.88 | 5.96 | 0.82 |
| **2** | 23 | 0.28 | 2.38 | 11.87 | 8.06 | 5.68 | 0.7 |
| **3** | 27 | 0.33 | 2.29 | 10.01 | 7.87 | 3.46 | 0.44 |
| **4** | 25 | 0.31 | 2.29 | 10.15 | 9.72 | 4.73 | 0.46 |
| **5** | 20 | 0.24 | 1.78 | 7.42 | 14.31 | 5.97 | 0.44 |
| **6** | 17 | 0.21 | 1.84 | 7.80 | 7.69 | 2.51 | 0.35 |
| **7** | 7 | 0.09 | 2.47 | 4.60 | 8.26 | 3.41 | 0.43 |
| **8** | 3 | 0.04 | 1.63 | 5.02 | 9.69 | 4.13 | 0.42 |
| **9** | 5 | 0.06 | 1.83 | 2.18 | 7.61 | 6.2 | 0.86 |
| **10** | 1 | 0.01 | 1.71 | 3.95 | 2.9 | 6.11 | 0.87 |

### *Sinuosity and cutoff distribution*

The mean sinuosity of the Red River reaches ranges from 1.63 to 2.47, where sinuosity is generally greatest where the channel slope is high. Those high-slope, high-sinuosity reaches are also those with greater cutoff frequency per river length in comparison to low-slope, low-sinuosity reaches (Figure 19 and Table 1). Reach 7 is an anomaly within the trend of more sinuous reaches having a greater cutoff frequency, being the most sinuous reach but containing only seven cutoffs. Reaches 1–4, with a high sinuosity and high cutoff frequency, are also those reaches that are established atop areas of palimpsest conditions comprised of clay-sand mixtures associated with 1) the Comstock moraine (Lower Red Lake Falls Formation) deposited during the stepped recession of the late-Wisconsinan Des Moines Lobe of the LIS and 2) the Sheyenne River Delta, which may contribute to the abundance of meander cutoffs in these reaches.

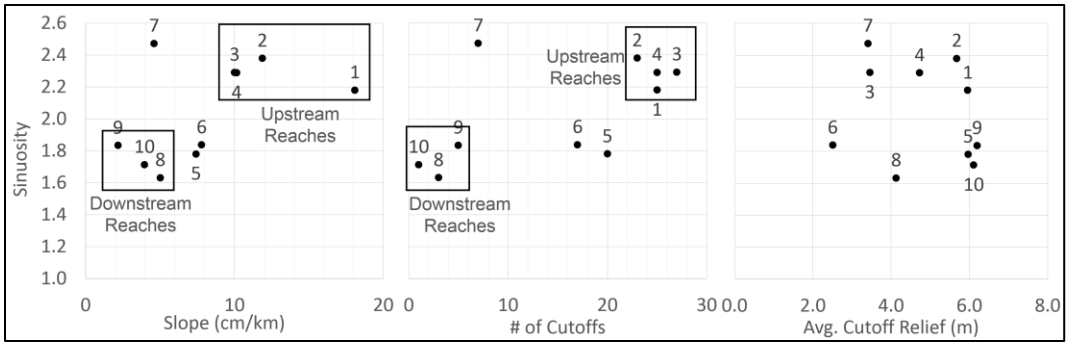


**Figure 19.** Reach-averaged sinuosity versus slope, cutoff count, and mean relief. Clear differences are observed between southern/upstream and northern/downstream reaches when comparing sinuosity to slope and the cutoff count, while mean cutoff relief does not show as distinct of a difference between upstream and downstream reaches.

### *Incision, slope and cutoffs*

The Red River is not deeply incised over its length, with a maximum incision of ~16 m (Figure 20a and b). The area near river km 480 and the Edinburgh Moraine (Falconer Formation), associated with the re-advance of the late-Wisconsinan Des Moines Lobe during the concurrent Moorhead Lowstand and Younger Dryas period, is most deeply incised (Figure 20a and b, Figure 21, area B). Being centered on the Edinburgh Moraine, Reach 5 has the greatest mean incision. The second area of relatively high incision is in Reaches 1 and 2 near river km 720 and the Sheyenne River Delta and Comstock Moraine, where the Red River is incised ~10 m (Figure 21, area C). The farthest downstream reach, Reach 10, has the lowest mean incision (Table 1). In Reaches 8 and 10 there are three smaller topographic undulations among the otherwise flat floodplain which may signify the presence of smaller or buried moraines deposited earlier in the Wisconsinan. Those areas of minor undulations are incised 5–10 m.

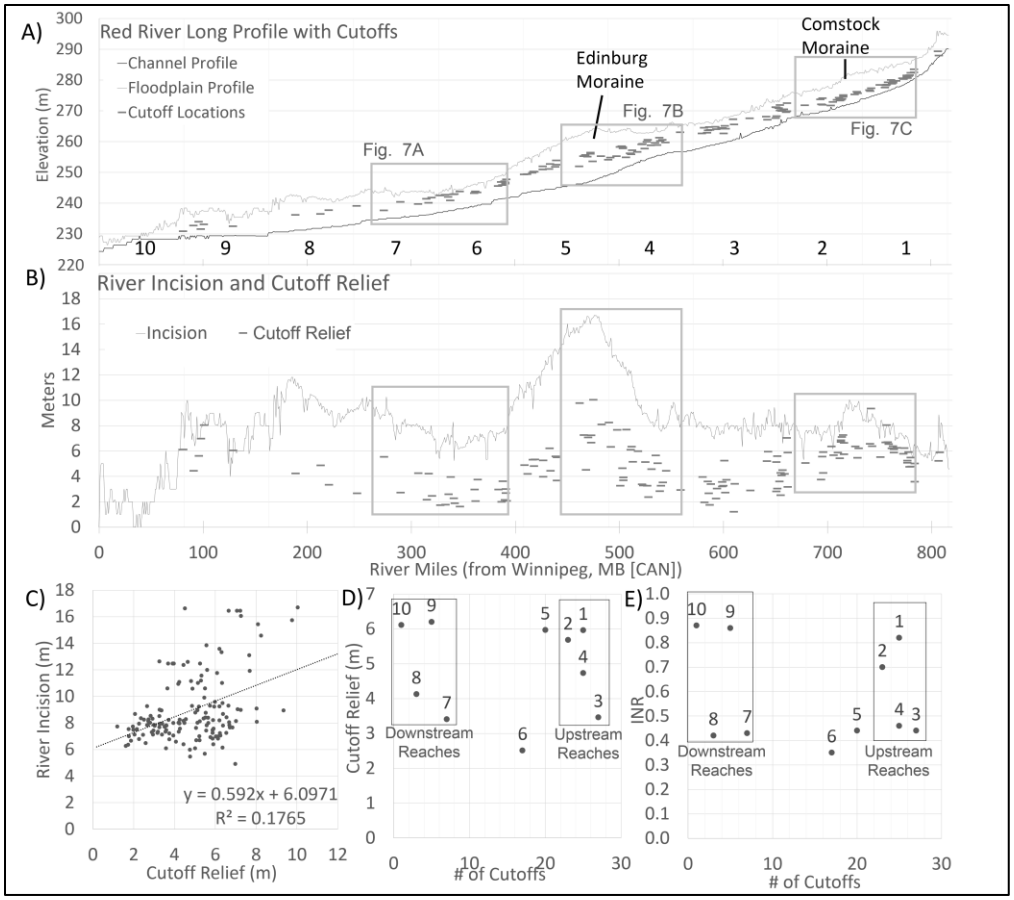


**Figure 20.** River and floodplain profiles, attributes and cutoff distribution. Elevation profiles (A), incision and cutoff relief (B), cutoff relief vs. river incision (C), cutoff relief vs. cutoff count (D), and INR vs. cutoff count. Profiles (A) and (B) show the channel and floodplain elevations and cutoff locations as related to areas A-C in Figure 21 and the Edinburgh and Comstock Moraines with reach numbers correlating to Figure 18. (C) depicts a weak, positive relationship between incision and relief. Both relief (D) and INR (E) show distinctive differences in cutoff counts between upstream and downstream reaches.

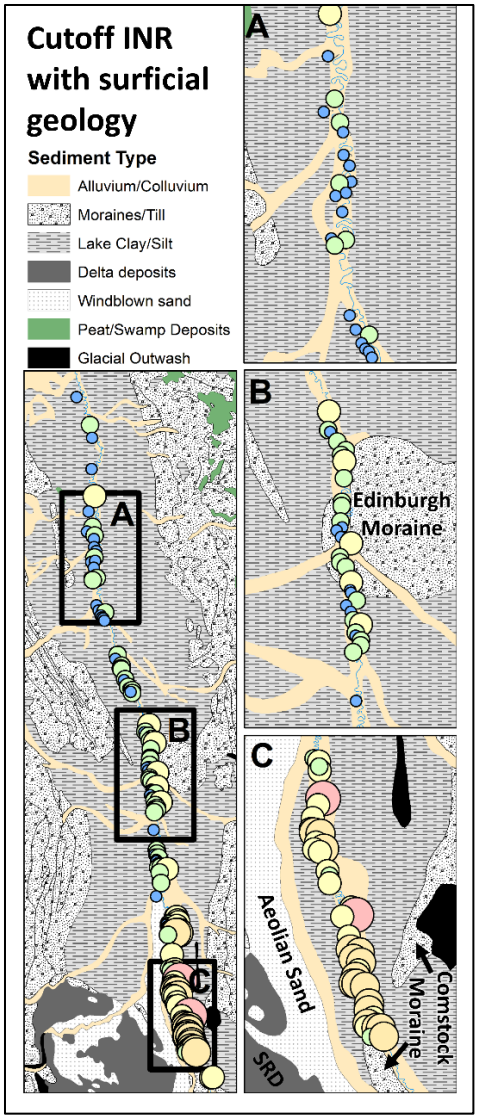


**Figure 21.** Meander cutoff INR and surficial geology (Fullerton et al., 2003). Inlay A depicts low INR cutoffs in an unincised reach established in glaciolacustrine clays deposited by Lake Agassiz (A). Inlay B displays low-medium INR cutoffs in a reach incised into the late-Wisconsinan Edinburgh Moraine. Inlay C shows medium-high INR cutoffs in a reach incised into sediments of the Sheyenne River Delta (SRD), windblown sands, and the late-Wisconsinan Comstock Moraine (each mapped in Figure 15D).

The channel and floodplain elevation long profiles for the Red River reflects the low slope nature of the floodplain and river, which generally decreases from upstream to downstream with slight undulations and possible minor knickpoints (Figure 20A and B, Table 1). The frequency of meander cutoffs per river length is generally greater in river segments with higher slopes. The high slope reaches are mostly those established atop palimpsest lithologies

associated with the Des Moines lobe of the late-Wisconsinan LIS. For example, Reaches 1 thru 4 have mean slopes that are over 10 cm $km^{-1}$ and are established atop the clay-sand sediments associated the Sheyenne River Delta and Comstock Moraines (Figure 21, area C). Where the cutoff frequency is lower, the low slope Reaches 8 thru 10 are established in the predominantly offshore areas of Lake Agassiz (Figure 21, area A) in areas of relatively homogenous glaciolacustrine sediments located far downstream of the major depositional areas of the late-Wisconsinan Des Moines Lobe of the LIS.

***Cutoff relief and INR distribution***

The relief of meander cutoffs for the Red River ranges from 1.19 to 10.03 m, with a mean of 4.76 m (Figure 22). Cutoff relief is positively skewed, where most cutoffs have 5-6 m of relief. Geographically, relief varies spatially with incision. Reaches with a greater mean cutoff relief typically coincide with more incised reaches. Individual reaches are typically dominated by either high or low relief meander cutoffs (as in Figure 18b). Low relief cutoffs (relief < 4 m) are widespread over the length of the river, but absent upstream of 47°N. High relief cutoffs (relief > 6 m) are most common upstream of 48°N, in Reaches 1 thru 5. Cutoffs with an exceptionally high relief (relief > 8 m) are clustered in two areas of river, both upstream (south) of 48°N and associated with locations of mixed clay-sand lithologic units deposited by the late-Wisconsinan Des Moines Lobe. Areas of high relief cutoffs in Reach 4 and 5 are located proximate to the Edinburgh Moraine (Figure 20a and b and Figure 21, area B). High relief cutoffs in Reaches 1 and 2 are located near the Sheyenne River Delta and late-Wisconsinan Comstock Moraine (Figure 20a and b and Figure 21, area C). In areas void of moraines, the relief of meander cutoffs is typically low.

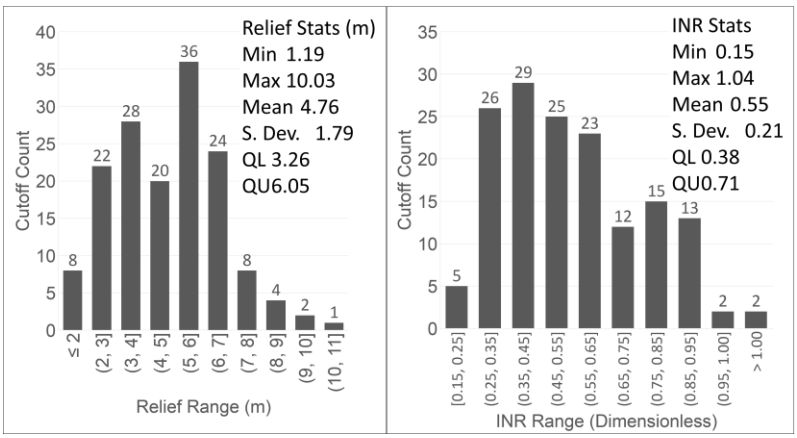


**Figure 22.** Histograms and descriptive statistics of relief and INR. Cutoffs show positive skews in both relief and INR.

Rivers are not typically incised uniformly over their lengths, so for such rivers the relief of meander cutoffs may not be adequate to suggest relative cutoff timing. The INR variable may help extend cutoff-based interpretations over greater distances by accounting for some of the spatial variability in incision by comparing the relief of meander cutoffs to the net depth of incision of the modern river. INR values near zero suggest that the cutoff relief is much less than the total modern river incision while INR values near one suggest that cutoff relief is similar to modern incision. The INR values for the Red River range from 0.15 to 1.03 with a mean of 0.55, after removing the outlier value of 1.42 (a cutoff in southern Manitoba with no DEM coverage resulting in an anomalous value) (Figure 22). INR is positively skewed, with the few cutoffs with high INR (INR > 0.6) values located toward the southern, upstream reaches (Figure 18c, Figure 20e) and low INR (INR < 0.4) located downstream. Like relief, INR values are typically greater in incised reaches, but the distributions of relief and INR differ locally from one another. Three cutoffs were found to have an INR over one (where relief was found to be greater than the calculated incision) which may signify recent formation (i.e. oxbow lakes), management (i.e. dredging of oxbows), secondary drainage development within the cutoff, influence of

unreconcilable urban topography, or may be an artifact of errors and omissions in the topographic data used for extracting river and floodplain profiles.

## Discussion

The spatial distribution of the 153 mapped Red River meander cutoffs reveal the results of a complex relationship between pre-set lithologic conditions and the history of geomorphic perturbations. To elaborate on this we further discuss 1) the meander cutoff distribution as related to GIA and pre-set palimpsest conditions from the Late-Wisconsinan LIS and overprinted by Lake Agassiz deposits, 2) the interpretation of GIA history in relation to meander cutoff relief, and 3) the use of the INR variable in interpreting relative chronologies for meander cutoff formation on incised/incising rivers.

### *The meander cutoff distribution, GIA, and palimpsest conditions*

Considering the regional trend of GIA, the Red River Valley has decreased in slope since river establishment with northern areas having the greatest net rebound and the greatest slope decreases (Figure 23) (Teller and Leverington, 2004). Decreases in valley slope typically cause rivers to decrease their sinuosity by meandering or forming meander cutoffs (Schumm, 1969; Schumm, 1977; Adams, 1980; Schumm, 1986; Hooke, 1995, Holbrook and Schumm, 1999). In a river undergoing differential slope decreases it would be expected that the spatial distribution of cutoffs would be skewed toward the areas that have undergone the greatest slope decreases. With this it would be expected that the highest frequency of cutoffs per river length would be in northern reaches of the Red River where glaciostatic rebound has caused the greatest valley slope decreases. Instead, the Red River's cutoff distribution is more closely related to spatial variations

in the river's pre-set lithologic conditions relating to the palimpsest of the late-Wisconsinan Des Moines lobe of the LIS, and aeolian and deltaic sands of the Sheyenne River Delta that have been overprinted by Lake Agassiz clay deposits.

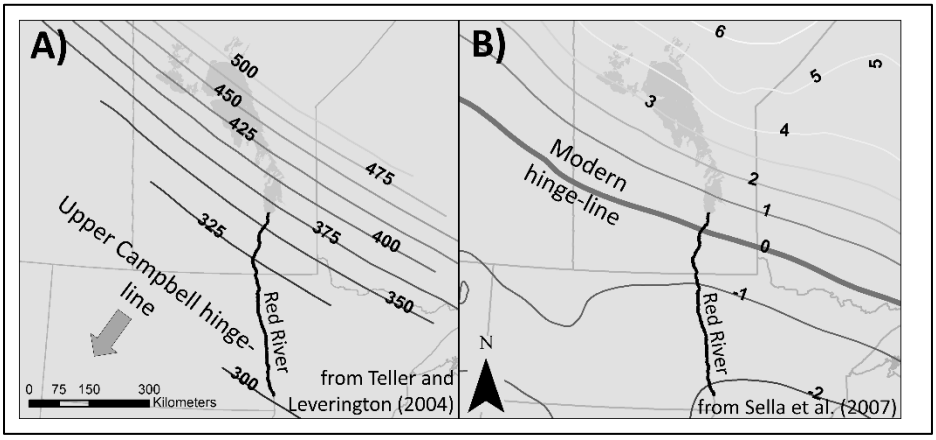


**Figure 23.** Holocene hinge line migration diagram. Shown are A) net rebound surface at the Upper Campbell Stage of Lake Agassiz depicting a hinge-line southward of the study area and B) modern rebound velocities determined by GPS stations showing relatively rapid rebound in the upstream reaches of the Red River and a hinge-line that has migrated northward to near the mouth of Lake Winnipeg.

Prior work on meandering rivers (Constantine et al., 2009; Schwendel et al., 2015) suggest that the Red River meander cutoff distribution is skewed toward erodible reaches because resistive lithologic units tend to dampen or inhibit the propagation of perturbations. This occurrence was also documented on the Rio Beni (Brazil) where clay-rich units in the otherwise sandy alluvium inhibited river meandering in reaches established in clays (Schwendel et al., 2015). Most of the Red River is established in thick, resistive glaciolacustrine clays, but the frequency (per river length) of cutoffs is highest in areas of late-Wisconsinan glacial deposits from the Des Moines Lobe of the LIS; and deltaic sands deposited by the Sheyenne River Delta (Figure 15D and Figure 21, areas B and C). These sandy units have been overprinted by thinner Lake Agassiz glaciolacustrine clays and create local areas in which erosional perturbations are able to proceed up- or downstream through the palimpsest reaches.

Perturbations are able to propagate through the sandy palimpsest reaches because the relatively sandy deposits cause the critical sheer stress (or velocity as related to the Hjulstrom-Sundborg diagram [Costa, 2016]) required for mobilization of alluvium to be locally lower than surrounding clay-rich reaches. Constantine et al. (2009) displayed the effects of consolidated material and clays on estimated bank erosion rates, finding greater critical shear stresses for alluvial clays and consolidated bank material in comparison to reaches with sandy alluvium. The propagation of meandering and incision processes through palimpsest reaches causes a higher cutoff frequency per river length throughout the palimpsest reaches. Conversely, reaches established in clay-rich alluvium have their erosional perturbations dampened because of the relatively high critical shear stress required to erode the cohesive clay deposits (Figure 20 and 21), which leads to lower cutoff frequencies.

As related to GIA, the meander cutoff distribution and the work of Constantine et al. (2009) and Schwendel et al. (2015) suggests that the glaciolacustrine clay sediments making up much of the Red River alluvium are resistive enough to remain relatively stable in northern reaches where slopes have diminished most throughout the Holocene. But, in the more erodible palimpsest areas of the Edinburgh and Comstock Moraines, farther south where postglacial net rebound and slope decreases have been less prominent the channel was able to adjust its sinuosity to the decreasing slope and form more cutoffs per length of channel (Table 1 and Figure 21).

### *Relief-based interpretations*

Meander cutoff relief can be used to interpret past channel conditions (i.e. bed and bank elevations) and infer the effects of slope decreases from GIA on erosional river perturbations.

Meander cutoff relief estimates the difference between the former bank top and the present-day level of infill within a cutoff. Cutoff relief calculations accurately represent the former bank top elevation for all cutoffs, but former bed elevations are buried beneath sediment deposited within the cutoffs. The present-day elevation of sediment in a cutoff is interpreted to be dependent on 1) the level of river incision upon formation of a given cutoff and 2) the amount of cutoff sedimentation since its formation. A channel that is incised upon cutoff formation yields preservation of high-relief cutoffs because, in comparison to an unincised channel, the starting bed elevation within the cutoff was much lower than the top of the bank when the cutoff formed. Cutoff sedimentation also affects relief, with more recently formed cutoffs being relatively void of sediment and earlier-formed cutoffs being mostly filled. Because in almost all cases of Red River cutoffs some local incision has occurred following cutoff formation (Figure 20B), the cutoffs never infill to the pre-cutoff bank level. This means that, in incising rivers, both the amount of pre-cutoff incision and level of post-cutoff sedimentation lead to interpretations agreeing that recent cutoffs are high relief and early cutoffs are low relief.

Although we acknowledge the importance of palimpsest conditions and lithology in controlling the overall meander cutoff distribution, applying relief-based interpretations to the Red River reveals the effect of post-LIS GIA on cutoff formation in the distant and recent past. Constraining rebound rates from early in the Red River's history (~7.9 ka BP) (Brooks, 2003b) is difficult, but rebound is understood to have been most rapid in the northern, downstream reaches (Reaches 6-10) during this time (Teller and Leverington, 2004; Gowan et al., 2016). Although there are relatively few cutoffs preserved in Reaches 6-10, most of these cutoffs have a lower relief than cutoffs in the southern reaches (omitting the six Canadian cutoffs due to holes in DEM coverage). We interpret the low relief cutoffs in northern reaches as forming soon after

river formation, during the period of rapid rebound in Reaches 6-10. During this time (~7.9 ka BP; Brooks, 2003b) channels would be relatively unincised prior to cutoff formation and the resulting cutoffs would have a relatively long period of post-cutoff sedimentation. The combined effect of there being little incision prior to cutoff formation and a long period of sedimentation after cutoff formation causes most of the cutoffs in downstream reaches to have a relief less than that of upstream cutoffs.

Whereas rapid, early slope decrease can be associated with the mostly low relief northern cutoffs, the mostly high relief southern cutoffs are associated with more recent trends of GIA-driven slope decrease. Over time, the forebulge hinge of post-LIS GIA has migrated northward over 300 km, causing the area of relatively rapid slope decreases to shift southward (Figure 23; Teller and Leverington, 2004; Sella et al., 2007). The entire length of the valley is still decreasing in slope, but now northern reaches are rebounding (decreasing slope by about 1 mm $yr^{-1}$) while southern reaches are collapsing (decreasing slope by about 2 mm $yr^{-1}$). Earlier post-Agassiz rates of rebound are unknown in the southern Red River valley, but recent forebulge migration and the subsequent slope decreases should lead to decreases in sinuosity and increases in meander cutoff formation in the southern reaches. The timing of these events would cause relatively recent formation of cutoffs, which would be supported by the fact that most cutoffs in southern reaches (Reaches 1-4) are high relief. This would point to their recent formation, forming after/during river incision with relatively little time for cutoff sedimentation to decrease their relief to that of northern, downstream cutoffs. In both the case of early rapid rebound in northern reaches and recent rebound in southern reaches (causing slope decreases, decreases in sinuosity, and cutoff formation), these results agree with the work of Schumm (1977) and Adams

(1980) who noted decreases in sinuosity (by meandering and cutoff formation) in midcontinent rivers that had experienced slope decreases.

***Further use of the INR variable***

The INR estimates the ratio of pre-cutoff river incision plus post-cutoff sedimentation, divided by the total present-day incision (Figure 17C). For rivers/reaches where the total depth of incision is much greater than the thickness of cutoff-filling sediments, the INR more closely resembles a ratio of pre-cutoff incision to total incision. In such cases, the INR is a good estimate of relative chronology because the INR provides a measurement of the percentage of incision that had occurred upon cutoff formation. But, coring efforts should be made to identify the depth of cutoff-filling sediments prior to making any use of the INR variable.

The use of the INR variable to estimate cutoff chronologies is improved with prior knowledge of the cutoff deposit thickness or deposition rate for the cutoff/reach/river being investigated. With knowledge of cutoff deposit thickness, the INR calculation can be corrected by adding the cutoff deposit thickness to the relief. Adding deposit thickness to the relief to correct for cutoff deposit thickness would act as removing the cutoff deposits and reconstructing the paleochannel elevations. For example, a cutoff with a relief of 9 m (calculated for a single cutoff using the methods presented in this paper) and cutoff deposit thickness of 4 m would have formed when the paleochannel incision was at 13 m. Then, if the total incision for the adjacent, modern channel was 18 m the corrected INR value would be 0.72 for that cutoff and it could be said that 72% of the total incision had occurred upon that cutoff's formation.

The example correction calculation above could be repeated for other cutoffs within the reach, where total incision is similar and has likely occurred at a common rate between

neighboring cutoffs. Within the same reach, cutoffs with a smaller corrected INR would have formed first and cutoffs having a larger corrected INR would have formed later. If rates of incision can be estimated numerically, the corrected INR could then be used to form an incision-based interpretation of cutoff chronology without finding any datable material within cutoff deposits.

## Conclusions

This work displays that even in relatively homogenous lithologies, the legacy effect of glacial deposits and palimpsest conditions affects each the location, relief, and INR of cutoffs. Each incision, sinuosity, slope, and meander cutoff distribution display that the Red River's geomorphic characteristics are reflective of underlying glacial deposits and reflect a complex history of GIA in the region. We estimate that rapid, early glaciostatic rebound in the Red River Valley contributed to the formation of downstream, low relief cutoffs. Later, after the LIS forebulge had migrated northward to near Lake Winnipeg, slope decrease due to forebulge collapse in the upstream reaches has contributed to more recent cutoffs that are preserved as high relief cutoffs.

This study provides new methods of mapping meander cutoffs and gives examples of how results from cutoff mapping support geomorphic interpretations against tectonic history. The mapping method provides an advance over traditional methods by decreasing time necessary for mapping cutoffs at the river scale. At their current stage of development, the cutoff mapping methods are best applicable in low relief landscapes in areas of simple floodplain topography.

The method of calculating relief and INR does so uniformly at the river-scale, which makes it useful in forming river-scale geomorphic interpretations. Because incision is a factor in

controlling cutoff relief, relative chronologic interpretations are limited to adjacent segments of river that are similarly incised and would not be applicable in forming river-scale cutoff chronologies between incised and un-incised reaches. Considering such, interpretations would be best formed after correcting the INR for cutoff deposit thickness. INR-based chronologies could then be confirmed using dating methods of materials in the basal deposits of cutoffs.

# CHAPTER III: APPLICATION OF SIMPLE TILT FUNCTIONS FOR ESTIMATING GIA-DRIVEN RIVER AVULSION PATHS, LENGTH, AND TIMING USING PALEOTOPOGRAPHIC RECONSTRUCTIONS


## Abstract

Postglacial rivers are commonly affected by lateral tilting due to Glacial Isostatic Adjustments (GIA) that cause lateral tilting and slope reduction sometimes resulting in river avulsion. Here we present methods for reconstructing paleotopography from beach strandline elevation data, applying tilt to landscapes, and detecting channel path changes in the Landlab modeling library. We apply these methods to a case study of the Red Lake River basin (Western Minnesota, USA) which shows evidence of Holocene avulsions. Using the results of 60 model runs, we test the relationships between the independent variables of GIA tilt rate, incision level, landscape roughness, and initial tilt, and dependent variables including the length and timing of channel avulsions. Results show that 1) the timing and length of channel avulsions are significantly affected by the rate of GIA tilt and incision, 2) the landscape roughness effects the length of avulsions but not the timing, and 3) the initial tilt (based on three late Lake Agassiz stages) does not significantly affect avulsion length or timing. This work provides new ways to apply land-surface tilting in the Landlab modeling library and reveals significant controlling variables for the character of channel avulsions.


## Introduction

Rivers typically show two types of responses to land surface tilting, abrupt avulsions and gradual shifts or migration (Peakall et al., 2000). River avulsions are mostly associated with alluvial fans, braided rivers, lowland riverine plains, and deltas, and occur by the preference and stabilization of one flow path over another (Kleinhans et al., 2013). There are three distinct types

of avulsions; a) those caused by annexation of flow by an existing abandoned channel, b) avulsion by incision of a new channel that intersects with the active channel, and c) avulsion by progradation of the active channel (Slingerland and Smith, 2004).

For an avulsion to occur there must be some change in the ratio of resistance to flow between the active and avulsion path, which can arise because of 1) an increase in the ratio of avulsion course slope to the existing channel slope produced by a decrease in the gradient of the existing channel, 2) an increase in the ratio of avulsion course slope to the existing channel slope produced by an increase in the slope of the avulsion path, or 3) a change in sediment or water capacity of the existing channel that is not related to slope (Jones and Schumm, 1999). Also important are boundary conditions such as floodplain substrate composition and channel distributions (Autin and Blum, 2005), which can control the character and rate at which avulsion processes occur.

Past studies of avulsions have led us to understand that avulsion periods range from $10^1$ to $10^4$ years for natural systems (Mohrig et al., 2000; Stouthammer and Berendsen, 2001; Jerolmack and Mohrig, 2007; Hajek and Wolinsky, 2012). Studies of flow-path selection, however, are more rare. Stratigraphic observations suggest that flow-path selection varies from random (Chamberlin et al., 2016) to compensational (Straub et al., 2009; Wang et al., 2011) to clustered (Sheets et al., 2007; Hajek et al., 2010; Chamberlin and Hajek, 2015), but model-based and experimental work has shown that flow-path selection is dependent on the fluvial topography near the active channel (Jerolmack and Paola, 2007; Reitz et al., 2010; Reitz and Jerolmack, 2012). Despite the advances in our understanding of avulsions, results of experimental studies still do not agree with what is observed in nature (Edmonds et al., 2016).

In postglacial landscapes, avulsions occur because of landscape tilting due to GIA as global isostasy rebounds toward equilibrium in response to the removal of the overlying glacial burden. In GIA-effected landscapes, tilt causes the ratio of gradient between existing channels and avulsion paths to decrease and make avulsions more likely to occur. In studies reporting channel avulsions at field scale, ratios of lateral to axial slope range between 0.35 and 1.16 (Peakall et al., 2000 and references within). Studies reporting channel migration had a lateral to axial slope ratio of 0.85 to 4.41.

The isostatic adjustments driving landscape tilting last for tens of thousands of years due to the viscoelastic relaxation of the earth's mantle, with the most rapid rates of adjustment occurring soon after deglaciation (Steffen and Wu, 2011; Gowan et al,. 2016). In North America, GIA-driven tilt has occurred since the melting of the Laurentide Ice Sheet (LIS). Between 17 and 10 ka, the LIS lost ~$7e^6$ $km^3$ of ice (Gowan et al., 2016), and as the associated overlying mass was removed the Earth's surface began to vertically rebound causing uplift. Isostatic uplift in turn caused decreasing tilts of Earth's surface across much of Canada and the American Upper Midwest, Great Lakes, and Northeast regions (Gowan et al., 2016). The greatest rates of vertical rebound occur at the former centers of mass of the LIS, causing the upward tilting of topography trending toward those centers. The dominating center of mass of the LIS throughout much of the Pleistocene was positioned to the northeast of the Hudson Bay, thus trends of land surface tilt is oriented toward an area to the northeast of the Hudson Bay.

As the LIS melted, portions of meltwater collected to form Glacial Lake Agassiz which persisted between 12 and 8 ka (Clayton and Moran, 1982; Teller and Bluemle, 1983; Teller and Leverington, 2004). As Lake Agassiz fluctuated in size from changes in meltwater volumes and opening/closing lake outlets, beach deposits were abandoned to be preserved among the

otherwise flat topography. These deposits, originally horizontal, are now found at greater elevations in northern areas of Lake Agassiz. Although estimates suggest that up to 73% of the total rebound may have occurred prior to the deposition of any strandlines, the trends of the current strandline elevations display an estimate of the landscape's tilt since the deposition of beach strandlines (Brevik and Reid, 2002). The pattern of their tilt shows that the greatest amount of rebound is to the northwest, causing a general decrease of drainage corridors associated with the present-day Red River Basin.

Past avulsion-related work in the Lake Agassiz basin has focused on compaction ridges, or paleochannels sandwiched between units of glaciolacustrine clay deposited during the two highstands of the lake (Dilworth and Fisher, 2018). The path of those compaction ridges, in comparison to the modern channel paths on the bed of Lake Agassiz, show that channel paths have shifted considerably since the early-Holocene.

Here we take a systematic, steepest descent approach to modeling, focusing on channel avulsions driven by land-surface tilting. We describe the use of the LandLab Landscape Evolution Modeling library and ESRI ArcMap 10.7 in recreating paleotopography and predicting the relative timing, frequency, and lengths of channel avulsions produced by tilting associated with GIA. We provide two simple numerical tilt functions for tilting paleotopography recreated from strandline tilt trend surfaces using strandline elevation points from three late stages of Lake Agassiz (Breckenridge, 2015). With those reconstructions and tilt functions, we simulate tilting on the Red Lake River Basin (MN) and test the hypotheses that the rate of GIA tilt, incision constant, topographic roughness, and initial tilt of topographic reconstructions are all significant controls of the timing and length of channel path changes.

## Methods and model

The timing, location, and length of GIA-driven channel avulsions were estimated for recreated paleotopography by utilizing numerical landscape evolution models in the Landlab modeling library (Hobley et al., 2017). Starting with topographic reconstructions late in the history of Lake Agassiz, a tilt function is applied to topography at each timestep so that the tilt of the landscape is reduced flattens at each timestep and the final modeled topography matches the modern DEM at the end of the simulation. Tilt functions are applied to topography prior to fluvial and hillslope erosion at each timestep, resulting in differential uplift and rerouting of flow paths throughout the modeling period. These models assume that reduced tilting due to isostatic rebound is the dominant process driving channel avulsion, so channel incision is held constant and hillslope erosion is kept at a minimum while deposition and aggradation are ignored in modeling. Exemplary scripts are located in Appendix B

### *Topographic reconstructions from strandline or gage elevations*

These methods exemplify topographic reconstructions conducted using strandline elevation data, but these methods would also be appropriate for elevational data from geodesic GPS stations or lake stage gages (Teller and Leverington, 2004). Topographic reconstructions were conducted using the Landlab landscape evolution modeling library, for which the initial topographic tilt was determined by creating a first order best-fit surface those points using the Trend tool in ESRI ArcMap 10.7.

Slopes in the x- and y-directions were measured (Table 1) and reconstruction functions were applied to the modern topography by multiplying the x- and y-coordinates at the center of

each cell (known as a node in Landlab) in the modern DEM by the negative of the present-day strandline tilt (Eq. 1 and Eq. 2):

$$z_0 = z - (S_x * x) \quad \text{(Equation 1)}$$

$$z_0 = z - (S_y * y) \quad \text{(Equation 2)}$$

where $z_0$ is the reconstructed topographic elevation (at t = 0), z is the modern topographic elevation, $S_x$ and $S_y$ are the slope of the best fit surface of the strandline points, and x and y are the x- and y-coordinates associated with the center node of each cell of the modern DEM, relative to the origin in the southwest corner of the bounding box of the DEM at (0m, 0m, 0m).

***Landscape evolution model***

Fluvial and hillslope erosion were modeled using the stream power and linear diffusion theories, respectively. The model applied here ignores deposition and aggradation, simulating only the processes of landscape tilting, fluvial incision, and hillslope erosion. GIA tilt is applied by multiplying coordinates of the center node of each raster cell by an adjustment factor resulting in differential uplift which changes the steepest slope in the model's flow routing algorithm.

*Tilt functions*

Assuming no uniform, vertical, regional uplift, scenarios for varying reconstructions and rebound (tilt) rates and orientations were tested and compared to a control scenario with no tilting. Tilt functions were designed to simulate decaying postglacial GIA tilting and constant GIA tilting. The control scenario erodes the reconstructed topography and applies no tilting. Each simulation finishes with the resulting topography matching the tilt of the modern topography.

Decaying tilt functions were applied at each model timestep by multiplying the x- and y-coordinates of each DEM node by an adjustment factor that decreases incrementally with each timestep (Eq. 3 and Eq. 4) where $z_{t(x,y)}$ is the elevation at each node of the raster grid at time t (in either the x- or y-direction), $z_{t-1}$ is the elevation of each raster grid node at the prior timestep and $t_i$ is the time of the current timestep. With this, the differential decaying tilt functions in the x- and y-directions are:

$$z_{tx} = z_{t-1} + \frac{S_x}{t_i} * x \quad \text{(Equation 3)}$$

$$z_{ty} = z_{t-1} + \frac{S_y}{t_i} * y \quad \text{(Equation 4)}$$

The constant, differential tilts were applied using functions that divide the slope of the topographic reconstructions in the x- and y-directions ($S_{x,y}$ in Table 1) equally over the number of timesteps. Those values are divided by the total number of timesteps ($t_n$) and then multiplied to the x- and y-coordinates of the reconstructed DEM nodes prior to being added to the elevation of each DEM node at the prior timestep ($z_{t-1}$) (Eq. 5 and Eq. 6).

$$z_{tx} = z_{t-1} + \frac{S_x}{t_n} * x \quad \text{(Equation 5)}$$

$$z_{ty} = z_{t-1} + \frac{S_y}{t_n} * y \quad \text{(Equation 6)}$$

*Governing equations*

This landscape evolution model simulates fluvial incision and hillslope erosion to recreated, tilting topography, in which topography erodes by detachment-limited fluvial incision and linear hillslope diffusion. Both cases signify the shifting of river channels from post-Agassiz paths to those followed by modern channels. Simulations follow the conservation of mass to determine changes in elevation, z, measured relative to a base-level, which gives:

$$\frac{dz}{dt} = U - \nabla \cdot q \qquad \text{(Equation 7)}$$

where *t* is time, *q* is the volume flux of sediment per unit width of land surface, *U* is the rate of uplift relative to an arbitrary base level, and ∇ is the divergence. In this case we hold *U* as zero but instead apply tilt functions (see "Tilt functions" section above) within the model script to subject the land surface grid model to differential isostatic adjustment. We make U = 0 because here we are concerned only with channel shifting, and not incision of channels due to isostatic uplift. The total sediment flux, q, includes fluvial and hillslope processes. The total flux can then be expressed as the sum of the sediment flux from the river, $q_f$, and hillslope flux, $q_h$:

$$\nabla \cdot q = \nabla \cdot q_f + \nabla \cdot q_h \qquad \text{(Equation 8)}$$

In fluvial systems, the transport of material and channel incision requires the detachment of bed material and its subsequent entrainment. As prior modeling efforts in other postglacial basins have, we assume that fluvial sediment transport, $q_f$, is detachment-limited and that all eroded material is transported out of the model domain and no deposition occurs (Gran et al., 2013; Lai and Anders, 2018). This is simulated using the stream power law, applying a threshold to simulate the critical stream power, $\theta_c$, required to initiate sediment erosion (Howard, 1994; Whipple & Tucker, 1999). This makes the fluvial sediment flux:

$$\nabla \cdot q_f = K(A^m S^n - \theta_c) \qquad \text{(Equation 9)}$$

where *K* is the fluvial erosion constant, *A* is upstream drainage area, *S* is slope, and *m* and *n* are positive, case-specific constants with a ratio *m/n* of ~0.5 (Whipple and Tucker, 1999).

Hillslope erosion is modeled here using a diffusion equation, which is common with low-relief landscapes with low-gradient hillslopes that are typical of postglacial topography (Perron et al., 2008; Lai and Anders, 2018). Using this theory makes the hillslope sediment flux proportional to the slope, which is calculated as:

$$q_h = -D\nabla \mathrm{h} \qquad \text{(Equation 10)}$$

where *D* is the diffusivity of the hillslope and $\nabla h$ is the topographic slope. Modeling landscape evolution assuming an uplift, *U*, of zero yields:

$$\frac{dz}{dt} = -K(A^m S^n - \theta_c) + D\nabla^2 \mathrm{h} \qquad \text{(Equation 11)}$$

The fluvial erosion constant (K) is varied in this study to test the effect of incision on the character of channel path changes, but is held to low values (K > 0.0001) to simulate postglacial landscapes. In this series of model runs we test the sensitivity of the fluvial erosion constant (K), which simulates varying levels of river incision (Table 1).

**Table 2.** Fluvial erosion constants (K) for model runs

| **Incision Values** | |
|---|---|
| **Incision Level** | **Fluvial Erosion Constant (K)** |
| Low | 1.00E-08 |
| Medium Low | 1.00E-07 |
| Medium | 1.00E-06 |
| Medium High | 1.00E-05 |
| High | 1.00E-04 |

***Landscape smoothing***

The above landscape evolution model and tilt functions are also applied to test the effect of landscape roughness on channel path changes. We test the original topographic roughness and a smoothed version more similar to a simple, flat model domain. The original topography was smoothed with a low-pass filter using the Filter Tool in ArcMap 10.7, which removed anthropogenic topography such as urban areas, road and rail beds, and drainage ditches. The smoothed topography was produced using a 1500-m circular smoothing window in the Focal

Statistics Tool. The resulting smoothed topography serves as a simple model domain with no eroded river valleys and only mimics the large-scale undulations of the original topography.

### *Detecting channel path changes*

Channel paths were mapped as discrete rasters which show nodes where a channel is present or not present. This was done by setting a flow accumulation threshold in the LandLab script. Any cells above that threshold were mapped as a channel, with a raster value of one. Any cells that did not exceed the threshold were designated a raster value of zero. The threshold value can be lowered to show lower order streams or increased to show only the main stem of a basin. Changes in channel paths were calculated by differencing raster layers from each set of two consecutive timesteps. Lengths of those changes were calculated by converting the discrete rasters into polylines and measuring their length in ESRI ArcMap 10.6 (script provided in Appendix B).

### *Statistical testing*

Using the avulsion results we tested the hypotheses that the independent variables of rate of GIA tilt, incision constant, topographic roughness, and topographic reconstructions are significant controls of the dependent variables, which were the timing and length of channel path changes. The hypotheses being tested were:

- Null hypothesis: The independent variable (reconstruction, GIA rate, incision, or topographic roughness) is not a significant control on the dependent variable (avulsion length or timing).

- Alternate hypothesis: The independent variable (reconstruction, GIA rate, incision, or topographic roughness) is not a significant control on the dependent variable (avulsion length or timing).

Assuming no interaction between independent variables, we test for the rejection of the null hypotheses using a One-way Analysis of Variance (ANOVA) at a significance level of $\alpha = 0.05$ to compare each independent variable's effect on each dependent variable.

**Example application of landscape reconstructions and tilt functions for mapping channel path changes**

Here we exemplify the reconstruction methods, tilt functions, and channel path changes as applied to a case study of channel path changes of the Red Lake River and Red Lake River drainage basin (Figure 24). Reconstruction methods detailed above were used to recreate the topography that would have been present at three different late stages of Lake Agassiz, which resulted in the deposition of the Tintah, Ojata, and Campbell strandlines, using strandline elevation points (Breckenridge, 2015).

Tilt functions were used to apply a topographic tilt adjustment to each reconstructed topography so that the ending topography matches the modern DEM. The model results were used to estimate the timing, length, and location of channel path changes at the river scale and focus on the timing of one well-known avulsion, the Red Lake River- Grand Marais Creek avulsion [located at (47.8105°, -96.8185° DD), Figure 24].

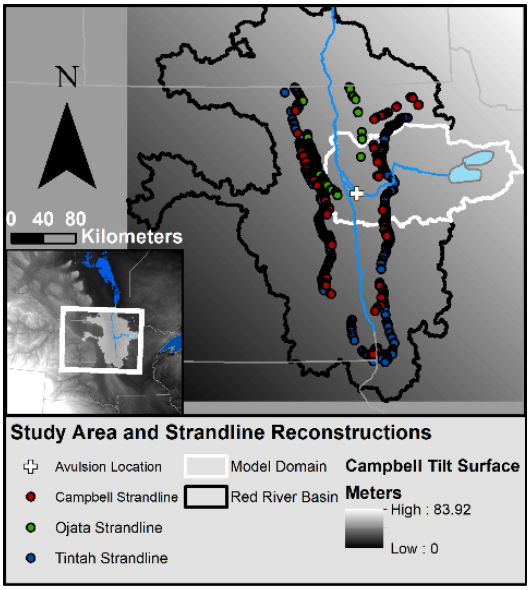


**Figure 24.** The Red Lake River model domain area (white). Also shown are the Red River Basin (black), late-Lake Agassiz Campbell, Ojata, and Tintah strandline point locations (from Breckenridge, 2005), and the location of the Red Lake River-Grand Marais Creek avulsion (white cross). Exemplary tilt surface shown for the Campbell landscape reconstruction.

The Red Lake River's source is Red Lake. Red Lake is a remnant of glacial Lake Agassiz at its fullest extent, which have capped glacial tills comprising the surrounding area of Red lake with a layer of silty clays. The contributing watershed area includes postglacial uplands composed of complex sequences of Late-Wisconsinan glacial tills, moraines, and pothole lakes. The Red Lake River flows west from Red Lake, through predominantly low relief areas dominated by glacial tills to lowlands established in clay-rich sediments and very low-relief topography once inundated by Lake Agassiz.

***Strandline-based topographic reconstructions***

Best-fit surfaces of Lake Agassiz strandlines show dynamic topographic tilt during the last ~2.8 ky that Lake Agassiz was present south of the Canadian border (Figure 25). Tilt from ~13.5 ka to ~10.7 ka is dynamic in both rate and direction of tilt (Table 3). The slope of the best-fit surfaces varies in the x- and y-direction. Slope in the x-direction decreases by $2.7 \times 10^{-5}$ m/m

between the deposition of the Tintah and Ojata strandlines and remains constant between the deposition of the Ojata and Campbell strandlines. Slope in the y-direction decreases by $2.8x10^{-5}$ m/m between the deposition of Tintah and Ojata strandlines, but between the deposition of the Ojata and Campbell strandlines slope in the y-direction decreases by $1.5x10^{-5}$.

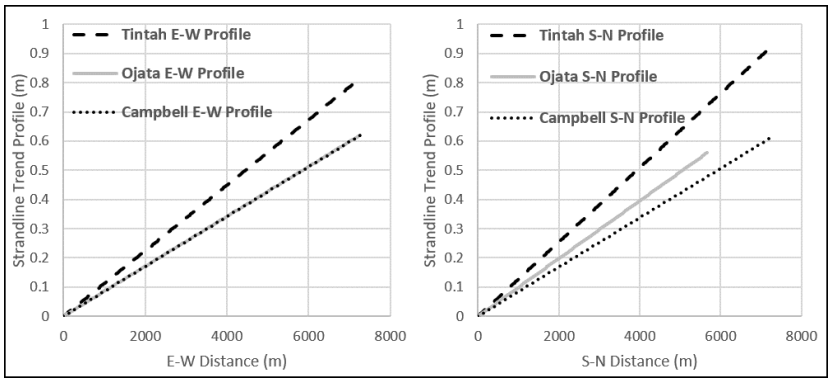


**Figure 25.** Strandline tilts of the Tintah, Ojata, and Campbell beaches. Initial tilts in the x-direction (left) and y-direction (right) for the last three major strandlines of Lake Agassiz.

**Table 3.** Strandline tilt, plunge bearing, and date summaries

| **Strandline** | **$S_x$** | **$S_y$** | **Slope (m/m)** | **Plunge Bearing (°E of N)** | **Date (yrs ka) (Dilworth and Fisher, 2018)** |
|---|---|---|---|---|---|
| Tintah | 1.12E-04 | 1.27E-04 | 0.0170 | 40.75 | 13.5 |
| Ojata | 8.50E-05 | 9.90E-05 | 0.0130 | 45.2 | 11.2 |
| Campbell | 8.50E-05 | 8.40E-05 | 0.0120 | 41.4 | 10.7 |

The bearing direction of the plunge lines from the best-fit tilt surfaces created using the Tintah, Ojata, and Campbell strandlines shifts eastward 4.45° between the deposition of the Tintah and Ojata strandlines. Between deposition of the Ojata and Campbell strandlines the plunge bearing shifts northward 3.8° (Table 3). Taking strandline ages into account, the mean rate and direction of changes in the plunge line's bearing each reverse between the deposition of the Tintah and Ojata strandlines and the Ojata and Campbell strandlines.

Topographic reconstructions of the area of the Red Lake River/Grand Marais Creek channel avulsion estimate that the slope of the Grand Marais Creek was 37% steeper than the

path of the Red Lake River during the deposition of the Campbell strandline (Figure 26). Fluvial topography of the Red Lake River upstream of the avulsion location displays more complex, developed topography when compared to fluvial topography downstream of the avulsion. Upstream, more meander cutoffs and terraces are present whereas downstream there are no meander cutoffs or terracing.

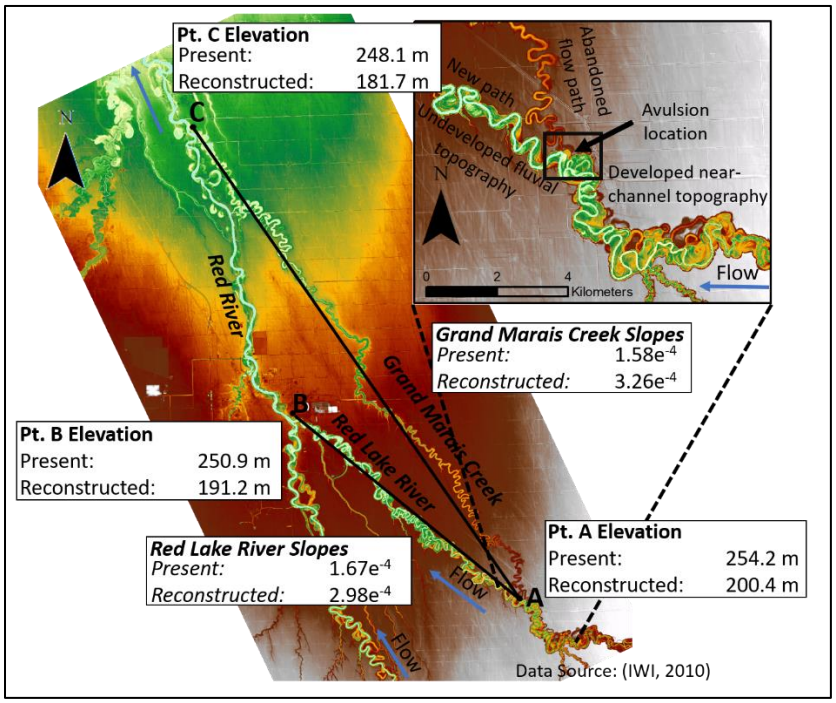


**Figure 26.** Topography of the Red Lake River-Grand Marais Creek avulsion. A more developed near-channel topography upstream of the avulsion and less developed near-channel topography downstream suggests that this is a channel avulsion. Slopes for pre- and post-tilt channel paths show that the steepest flow path has shifted from the Grand Marais Creek path to the Red Lake River path, as based on the Campbell strandline tilt.

### *Results: Summary and statistical tests*

For the 60 total model runs, 1,633 channel path changes occurred with an average length of 6.073 km (Table 4). One-way ANOVA tests for each combination of independent and dependent variables rejected the null hypotheses on three of the four independent variables as related to the length of avulsions and two related to the timing of avulsions at a significance level

of $\alpha = 0.05$ (Table 5). Animations of examples are available digitally through the link found in Appendix C.

Overall, the timing and length of channel path changes was found to be most affected by variations in the rate of GIA ($P = 0.025$ and $P < 0.0001$, respectively) (Table 5). The incision constant (K) was also an important factor in the count, timing ($P < 0.0001$), and length of channel path changes ($P = 0.005$). Landscape roughness was deemed to be an important factor in the length of channel path changes ($P = 0.01$) but not the timing of channel path changes ($P = 0.563$). The initial tilts tested here from the Tintah, Ojata, and Campbell strandlines did not have a significant effect on the count, timing ($P = 0.085$), or length ($P = 0.085$) of channel path changes. Even though the effect was not statistically significant, reconstructions beginning with a greater tilt, and thus having a greater tilt rate, were found to create marginally more avulsions (Table 4).

**Table 4.** Summarized avulsion model results grouped by parameter

| Modeling Results | | | | | | |
|---|---|---|---|---|---|---|
| | **Avulsion Count** | **Avg Length (km)** | **Avg. timing (model yr.)** | **Std. Dev. Length (km)** | **Std. Dev. timing (model yr.)** | **Sum (Length [km])** |
| **All Runs** | 1633 | 6.07 | 3230 | 9.80 | 3196 | 9917.79 |
| **Modeling results grouped by Reconstruction** | | | | | | |
| **Tintah** | 617 | 6.41 | 3455 | 10.24 | 3210 | 3955.75 |
| **Ojata** | 522 | 6.45 | 3075 | 10.41 | 3182 | 3365.70 |
| **Campbell** | 494 | 5.26 | 3114 | 8.45 | 3188 | 2596.33 |
| **Modeling results grouped by GIA Rate** | | | | | | |
| **Decaying** | 975 | 5.41 | 2031 | 10.77 | 2031 | 6356.21 |
| **Constant** | 658 | 6.52 | 5007 | 8.11 | 5007 | 3561.58 |
| **Modeling results grouped by Incision Level** | | | | | | |
| **High** | 285 | 4.27 | 4369 | 7.40 | 3754 | 1217.45 |
| **Medium High** | 165 | 7.09 | 2672 | 11.60 | 3050 | 1169.05 |
| **Medium** | 187 | 6.19 | 1784 | 9.56 | 2697 | 1156.87 |
| **Medium Low** | 495 | 5.95 | 3393 | 9.56 | 3052 | 2944.53 |
| **Low** | 501 | 6.85 | 3146 | 10.54 | 2957 | 3429.88 |
| **Modeling results grouped by Landscape Roughness** | | | | | | |
| **Smoothed** | 1186 | 5.71 | 3202 | 9.71 | 3202 | 6772.04 |
| **Normal** | 447 | 7.04 | 3305 | 9.80 | 3305 | 3145.75 |

**Table 5.** One-way ANOVA test results

| | **Length (km)** | | **Timing (yr)** | |
|---|---|---|---|---|
| **Ind. Variable** | **P-value** | **Reject Null (Y/N)** | **P-value** | **Reject Null (Y/N)** |
| Reconstruction | 0.085 | N | 0.085 | N |
| GIA Rate | 0.025 | Y | <0.0001 | Y |
| Incision Level | 0.005 | Y | <0.0001 | Y |
| Topographic Roughness | 0.015 | Y | 0.563 | N |

### *Channel avulsions for varying strandline reconstructions*

The strandline-based reconstructions performed here did not significantly affect the timing or length of channel avulsions (Table 5, Figure 27). Most cutoffs were produced by the

Tintah reconstruction, which had the greatest initial tilt and therefore the greatest tilt rates throughout the modeling period. The fewest channel path changes were produced by the Campbell reconstruction, which had the lowest initial tilt and tilt rates. The three reconstructions produced similar avulsions with similar average lengths (Figure 28). The avulsions were similarly timed, occurring mostly early in the modeling period.

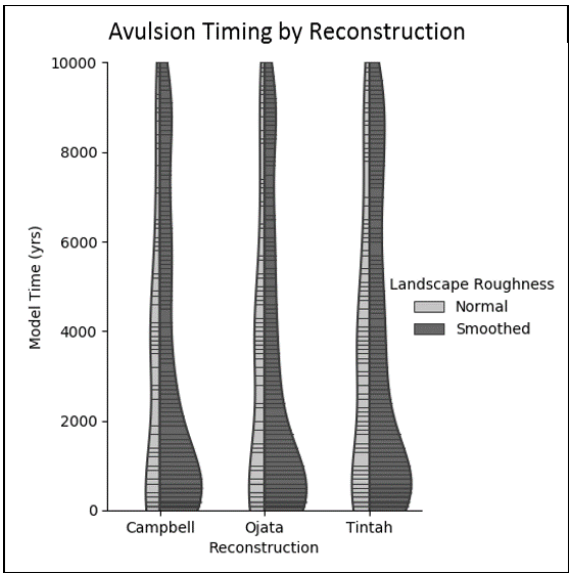


**Figure 27.** Violin plot: Avulsion timing grouped by reconstruction. Plots show the timing of channel path changes, with distance from the center axis of each plot representing the count of avulsions at each timestep (i.e. the wider the violin the more avulsions at a given timestep). Lines within the violins represent the time of occurrence for each of the individual avulsions. Plots show the variation in avulsion timing among the reconstructions and between the normal and smoothed topographies.

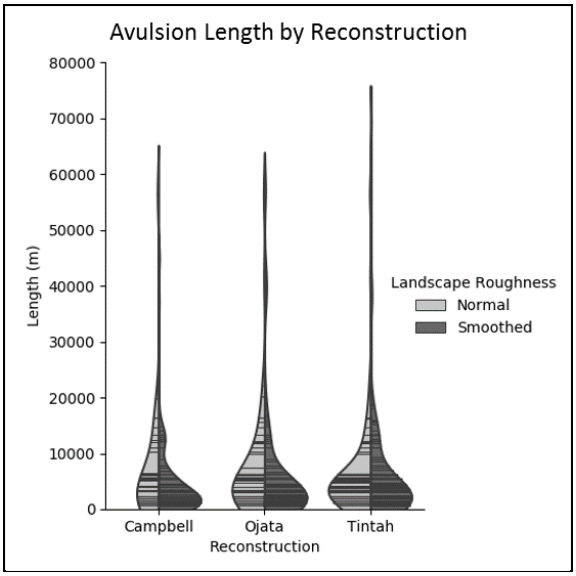


**Figure 28.** Violin plot: Avulsion length grouped by reconstruction. Generally, most of the channel path changes are short. Reconstructions with greater initial tilts produce more short avulsions, while the long avulsions remain the same regardless of initial tilt. Topographic roughness is significant in controlling the distribution of avulsion lengths, with the normal topography producing more prominent groupings of avulsion lengths.

### *GIA rate variation and avulsion properties*

The rate of tilt, whether decaying or constant, significantly affects the timing and length of modeled channel path changes (Table 5). The decaying tilt scenario produces tilt rates that are initially one magnitude greater in both the x- and y-directions than the constant tilt scenario (Figure 29). This leads to most of the avulsions in the decaying GIA scenario to be clustered early in the modeling period, whereas avulsions in the constant tilt scenario are more evenly spaced throughout the modeling period (Figure 30).

More avulsions were produced during the decaying rate simulations, and those avulsions are more tightly grouped toward the beginning of the modeling period. The average length of avulsions is similar, but because avulsions in the decaying GIA scenario are more common the total length of avulsions produced in the decaying GIA scenarios is ~56% greater than with

constant GIA. Similar avulsions occur in both decaying and constant tilt scenarios, though the timing of avulsions is generally later in the constant tilt scenarios.

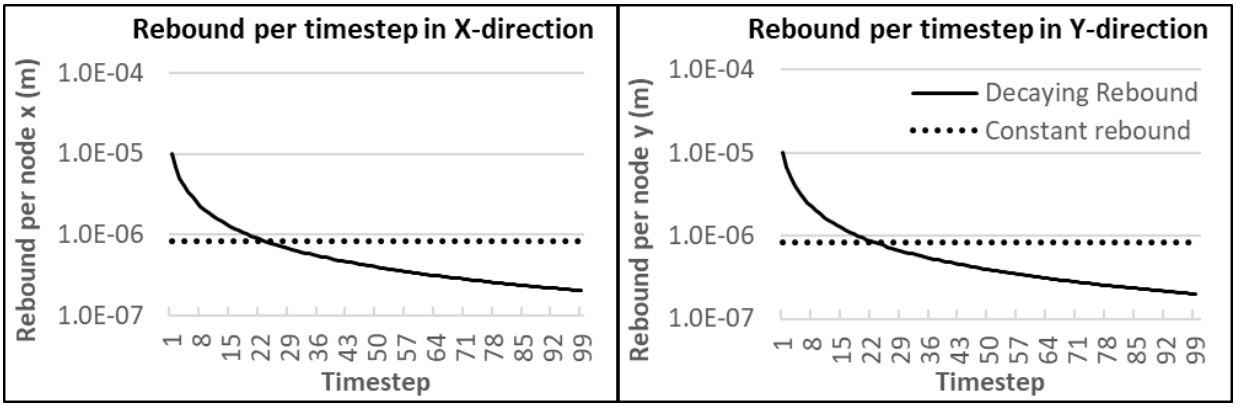


**Figure 29.** Rebound tilt per timestep in x- and y-directions. Tilt rate per meter in the x- and y-direction over the 100-year timesteps (10,000 years) for the Decaying (solid) and Constant (dotted) tilt scenarios. Based on landscape reconstructions, these equations are so that the greatest uplift is present in the northeast area of modeling domains.

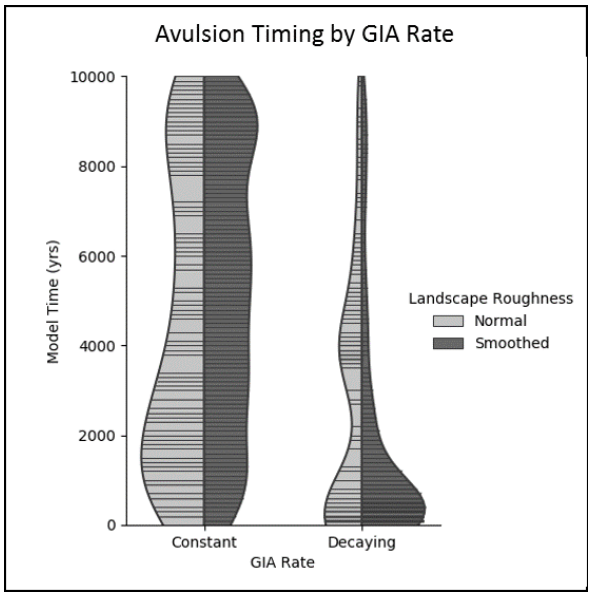


**Figure 30.** Violin plot: Avulsion timing grouped by GIA rate. Plots show the temporal variation of avulsions between the constant and decaying GIA model runs. Topographic landscape roughness affects the timing of avulsions, causing more periods with no avulsions in the normal topography as compared to the smoothed topography.

The length of channel avulsions is also dependent on the rate of GIA tilt (Figure 31). Avulsions are more commonly shorter than 10 km for both constant and decaying tilt rates. Long

avulsions account for the major channel path changes in individual simulations, but when summing the 60 simulations most of the channel path changes are short in both the constant and decaying GIA scenarios. Decaying GIA creates more avulsions that are longer that have a shorter average length, but greater maximum length than constant GIA.

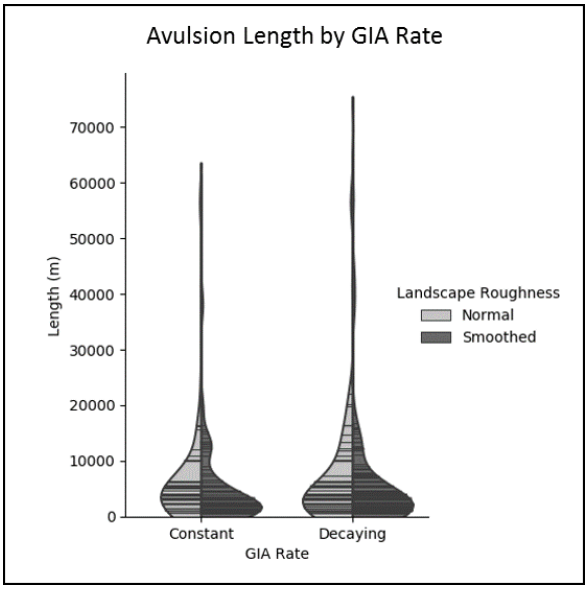


**Figure 31.** Violin plot: Avulsion length grouped by GIA rate. Avulsion length was found to be significantly dependent on GIA rate. Smoothed topography is more clearly effected by the GIA rate, with longer avulsions occurring on normal topography in comparison to smoothed topography.

### *Sensitivity testing of incision and effects on avulsions*

The relationships between incision and channel avulsions were tested by varying the incision constant (K) across five magnitudes (Table 2). The rate of incision was found to affect the timing and length of channel path changes. The earliest and latest average channel path changes were produced by the medium and high incision scenarios, respectively (Figure 32). On average, the shortest and longest avulsions were caused by the high and medium-high incision scenarios, respectively (Figure 33, Table 4).

The most realistic scenarios for the Red Lake River case study are either the medium-low or low incision model runs with normal topography and decaying GIA. These scenarios produce channel path changes that are most common early in the modeling period, with most channel path changes occurring before 1000 model years and very few occurring after 5000 model years.

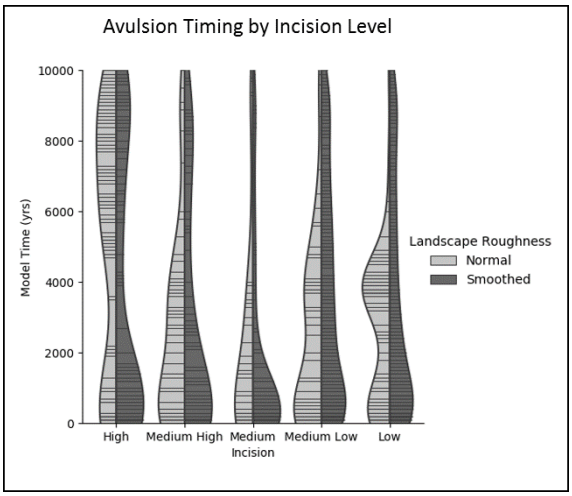


**Figure 32.** Violin plot: Avulsion timing grouped by incision level. Incision was determined to be a significant factor in controlling the timing of avulsions. Avulsions occur in two different styles related to either incision or GIA tilting. Combinations of GIA and incision cause the medium incision scenario to have the earliest avulsions, with other scenarios showing a division in the timing of avulsions caused by GIA and those caused by incision.

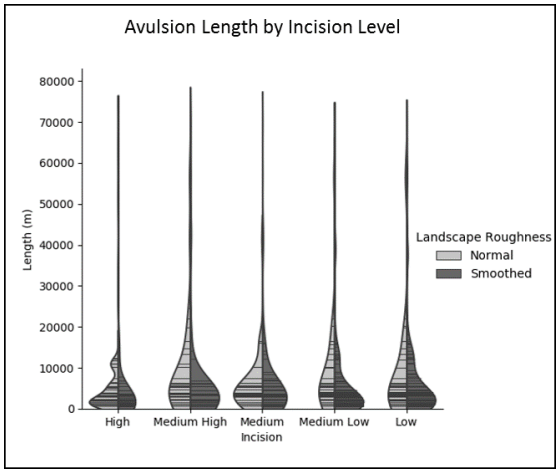


**Figure 33.** Violin plot: Avulsion length grouped by incision level. Although most avulsions are short, incision was found to be significant in controlling the length of avulsions. The shortest avulsions occurred in the high incision scenarios and the longest avulsions occurred in the medium-high scenario. The maximum avulsion length for each of the incision levels occurred in the runs with normal topography.

The length of avulsions, regardless of the level of incision, is more frequently short rather than long. Most of the recorded avulsions are short (less than 10 km long) and display gradual channel shifting behavior rather than abrupt avulsions. Long avulsions, greater than 20 km long, are relatively infrequent (fewer than five per model run) but account for the greatest proportion of path changes. Model runs with low incision on normal topography do not exhibit any downward incision, but the channel abruptly changes paths to completely new locations. For model runs with high incision on normal topography, the channel is laterally stable and displays downward incision with little lateral shifting.

### *Effects of landscape roughness on avulsions*

Topographic roughness is important in determining the timing, number, and length of channel avulsions (Table 5). The major variation between channel path changes on normal and smoothed topography is the characteristic of channel path changes. Smoothed topography allows for gradual shifting of channel paths, usually to neighboring cells, whereas normal topography causes longer, more abrupt shifts a greater distance from the original flow path. Smoothed topography produces almost three times as many avulsions as normal topography, but the length of cutoffs is shorter on smoothed topography rather than normal topography. Channel path changes are subtle in model runs with smoothed topography, with channel locations shifting gradually over the landscape rather than producing path changes to completely different drainage corridors like what is seen in the case of the Red Lake River–Grand Marais Creek avulsion (Figure 26). On smoothed topography, there are typically no long avulsions and avulsions never result in a shift to new drainage corridors.

Topographies with a normal initial roughness produce cutoffs that occur in more prominent temporal groupings, while smoothed topographies produce cutoffs that are more evenly spaced throughout the modeling period. Runs on normal topography produce a channel that more abruptly shifts over the landscape, with channel paths changing to completely different drainage corridors.

Comparisons of starting and ending topography and channel paths for the significant independent variables show that the ending topography and channel locations vary for each of the different combinations of GIA rate, incision level, and topographic roughness (Figures 34 and 35). Runs with similar topographic roughness and incision, but different GIA rates produce a different avulsion patterns and different final channel paths despite having the same ending topographies.

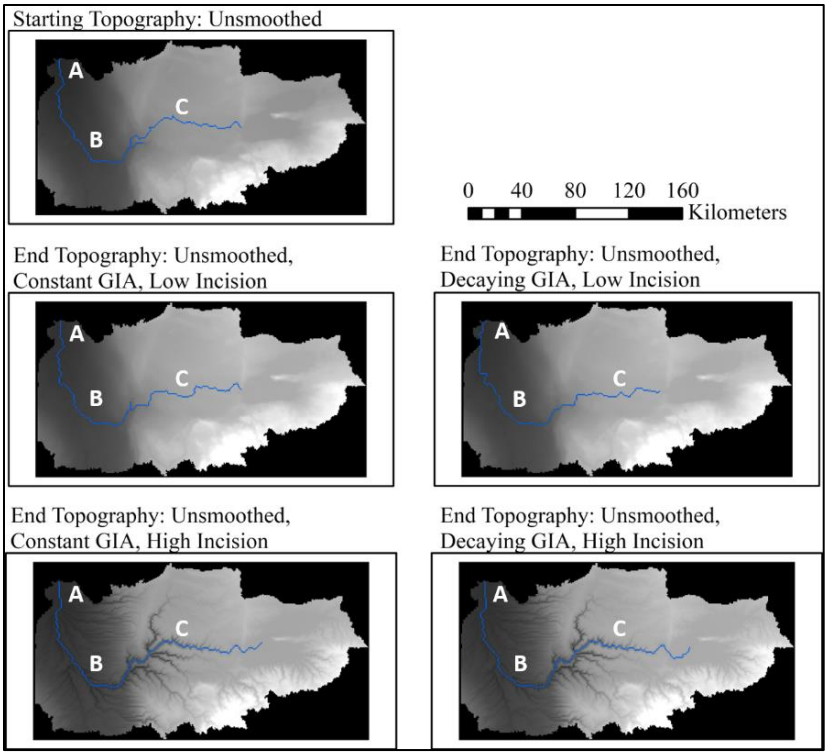


**Figure 34.** Starting/ending unsmoothed topography/channel path comparisons. A, B, and C label areas of major channel path variations. The starting channel paths (upper left) differ from the final channel paths for all simulation runs. Low incision runs (center row) show no visible incision and few, lengthy channel avulsions. High incision runs for constant GIA scenarios (bottom left) have channel paths that are the most like the starting channel paths.

On smoothed topography, starting and ending topography and channel paths are similar when compared to the unsmoothed topography. The channel path near the outlet, in the lowest relief area of the model domain, displays the effect of gradual channel shifting (Figure 35, A) that has resulted in westward channel migration. For both levels of GIA and incision, ending channel paths are different from the starting channel path but show major similarities to other ending channel paths.

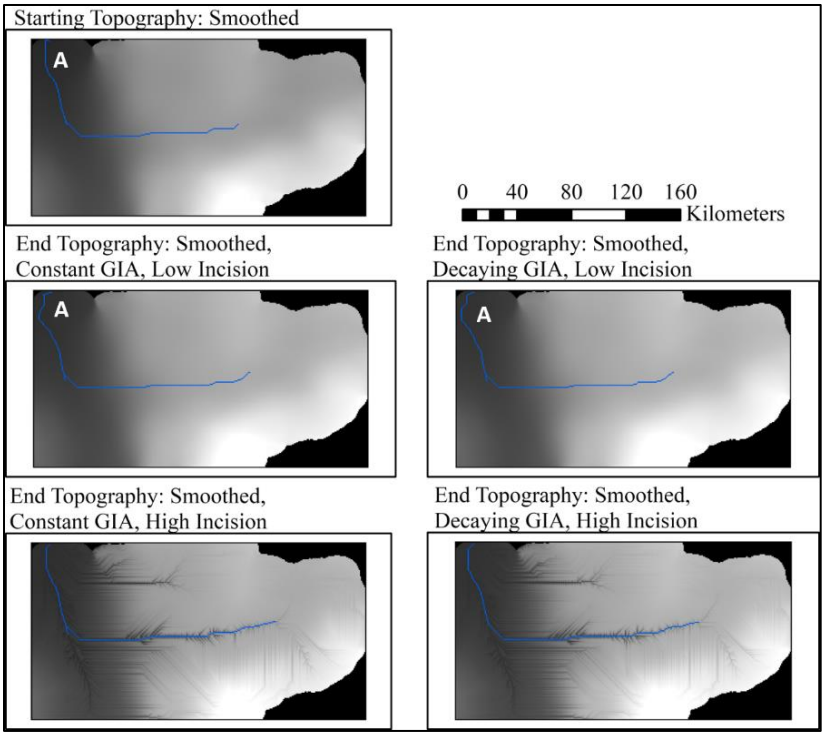


**Figure 35.** Starting/ending smoothed topography/channel path comparisons. Starting topography and channel path (upper left) largely matches the end topography in the low incision scenarios aside from near the outlet (A). Ending channel paths for high incision runs largely matches the initial channel path, but narrow, linear valleys have incised.

## Discussion

This numerical modeling exercise focused on the switching of channel paths under the circumstances of land-surface tilting resulting in a reduction of the overall tilt. Past studies of avulsion behavior have found two distinct styles; abrupt (Reid, 1992; Peakall, 1995, 1998; and Smith et al., 1998) and gradual (Nanson, 1980; Leeder and Alexander, 1987; Alexander et al., 1994; Boyd and Schumm; 1995). This work has highlighted three important factors in determining the characteristic and frequency of avulsions: 1) the rate of incision as studied here by varying the fluvial incision constant), 2) the rate of tilt (either constant and slow or rapidly decaying), and 3) the topographic roughness.

Although many other works focus on depositional processes (such as differential deposition or progradation) as the mechanism for avulsions (Mohrig et al., 2000; Morozova and Smith, 2000; Jerolmack and Mohrig, 2007) our modeling results display that abrupt, significant avulsions are possible in postglacial incising river reaches undergoing rapid GIA-driven tilting and no significant deposition. The model applied here (a stream power incision model with minimal hillslope erosion) simulates no deposition but results show similar styles of avulsion as past field studies. We acknowledge the importance of depositional processes in contributing to avulsions (Törnqvist et al., 2002; Taha and Anderson, 2008), but these results suggest that the steepening of avulsion paths (relative to the active channel) is also an important process in causing avulsions.

Peakall et al. (2000) discussed the distinct variations of channel path changes being abrupt or gradual in relation to the tilt rate for scenarios of discontinuous tectonic processes (faulting or caldera collapse/inflation). Here we simulate tilt in a scenario in which tilt is known to be continuous for upwards of 10 ka and find that lateral channel responses can be both abrupt or gradual in cases of continuous tilt. Contrary to Peakall et al. (2000), we find topography and incision levels to be important factors in whether channels migrate slowly or abruptly shift, and not solely the tilt rate. Such a variation in the type of fluvial response may show the importance of alluvial composition in determining the type of lateral response.

Due to variations in alluvial composition between the glaciolacustrine lowlands and glacial till uplands, incision in the study area being modeled is differential. However, we model incision at the same level across the entire model domain. Reaches established atop the former Lake Agassiz lakebed have little to no vertical entrenchment with valleys a maximum of 10 m deep. These reaches are most like model runs at the medium-low to low incision level. Upstream

of these reaches, outside of the lakebed, the rivers cut through post-glacial till and moraines and are incised up to 30 m. These reaches are more typical of incising post-glacial rivers, which would be most like our medium-high or high incision model runs.

In cases where incision levels were great enough to cause eventual entrenchment of the active channel, tilt rates early in the modeling period were required to be great enough to force steepening of the avulsion path prior to the entrenchment of the active channel by incision. Conversely, slow, constant tilting allowed entrenchment of the active channel before the avulsion flow path could become steeper than the active flow path. Because of this, in most model runs with rapid, decaying rebound early in the modeling period causes abrupt avulsion of the active channel.

Compared to other rivers, the tilting simulations of the Red Lake River ($1.69 \times 10^{-3}$ radians per thousand years) compare most closely with other rivers with abrupt avulsion responses to tilting. The Owens River (Reid, 1992) and Walker River (Blair and MacPherson, 1994), with tilt rates of $7.5 \times 10^{-3}$ and $2.9 \times 10^{-2}$ radians per thousand years each had abrupt avulsions form that are similar to the modeling performed here. Rivers with lower radial tilt rates such as the Madison (Leeder and Alexander, 1987), Beatton (Nanson, 1980), and Mississippi (Russ, 1982) have shown migratory response to tilting (Peakall et al., 2000). The major difference between this work and rivers included in Peakall et al. (2000) was that tilt in this modeling exercise is known to be continuous with time rather than tilting in discontinuous increments.

Topography was found to be important in determining the style of avulsion in this study, with gradual channel shifts occurring in the cases of smoothed topography and abrupt avulsions occurring in cases of normal topography. This result is concurrent with Dietrich et al. (1999) and

Jerolmack and Paola (2007), who noted the importance of floodplain topography in controlling avulsion paths.

**Conclusions**

- The count, timing, and length of avulsions are minimally affected by the initial tilt and tilt rates produced by landscape constructions from the late stages of Lake Agassiz, but the relationship is not statistically significant. Reconstructions with greater tilt and corresponding greater rebound rate cause slightly more avulsions with the longest total length.
- Relatively rapid, early GIA tilt produces more, longer avulsions than slow, constant tilt. The timing of avulsions in the decaying tilt scenarios also occur earlier in the modeling period in comparison to the constant tilt scenario. Long avulsions lead most of the channel path change to occur earlier with decaying tilt, whereas long avulsions occur later under conditions of slow, constant tilt.
- Greatest lateral channel stability occurs at/near $K = 1.0e^{-6}$ for both smoothed and normal topography. Suggests that both incision ($K > 1.0e^{-6}$) and avulsions (when $K < 1.0e^{-6}$) can cause the lateral shifting of channels. Channel shifts associated with incision lead to valley widening, whereas avulsion-related shifts abandon the prior valley.
- Topographic roughness is important in controlling the number and length of avulsions, but not their timing. Without topographic roughness, channels are free to gradually shift to other preferred paths that are near the former channel path. When a natural roughness is present, avulsions are forced to shift a greater distance from the former path which requires a longer avulsion.

- The major avulsions within the Red Lake River basin are estimated to have occurred in the first 700 years after the Red Lake River established its initial drainage. Since then, channel path changes are likely minor due to the entrenchment of channels in the glacial upland and the slowing of GIA tilt.

# CHAPTER IV: QUANTIFYING THE EFFECTS OF MEANDERING RIVER PLANFORM METRICS ON ICE-BANK IMPACTS AND BANK EROSION


## Abstract

For temperate and polar rivers there are many active processes that contribute to erosion during the spring thaw, which makes it hard to quantify the input from any single process. This work quantifies bank erosion due to mobile river ice collisions considering the frequency of collisions in relation to river planform metrics commonly used to describe meandering channels. To control as many variables as possible, physical experiments using paraffin wax as ice were conducted for multiple channel geometries, using the metrics of sinuosity, wavelength, amplitude, bend radii and bend length for comparison to the frequency of ice-bank impacts and the erosion occurring because of impacts. Here, the Impacts per Block per Banklength (IBB) metric is created to normalize the impact frequency by the number of wax blocks sent through the channel for each experiment, and the bank length of each experimental channel. Results show that, of the five planform metrics tested, the IBB variable relates most strongly to the bend length metric. The volume eroded during the period of wax additions best related to the sinuosity and IBB variables. Erosion was greatest during periods of wax (ice) additions. This study shows that erosion due to mobile river ice impacts is a contributor to erosion, displays the most common areas of ice-bank impacts to be the outer banks of bends, and allows us to begin to quantify the forces exerted on banks by flowing ice. As applied to full-scale rivers, more frequent bank impacts are expected in channel reaches with longer bends and a higher overall sinuosity leading to more rapid bank erosion in those reaches.

## Introduction

The transition from winter to spring is a highly dynamic period for rivers of temperate and polar regions, which often leads to most of a river's annual erosion occurring during the spring thaw (Arnborg et al., 1967; Walker and Hudson, 2003; Outhet, 1974). As a contributor to the geomorphic changes occurring during the thaw, the interactions between river ice floes and riverbanks is an important geomorphic element which is sometimes neglected in understanding river dynamics (Prowse and Culp, 2003).

River ice affects 56% of rivers on Earth but has declined by up to 4.3% since the 1980's (Yang et al., 2020). Ice cover on rivers is directly related to air temperature and precipitation and is a clear indicator of shifting climate regimes (Prowse et al., 2002). As climate warms river ice breakups occur earlier in the spring and shift from mechanical to thermal breakups (Beltaos, 2003; Cooley and Pavelsky, 2016). The shift from mechanical to thermal breakups may reduce the risk and severity of ice jams, but negatively effects the transportation of nutrients and sediment to downstream environments (Scrimgeour et al., 1994; Emmerton et al., 2008; Guo et al., 2012). Importantly disregarded in other work is the condition of the banks during breakup, which in the case of thermal breakups banks are more likely to be thawed, allowing for erosion from mobile river ice.

Flowing river ice causes the detachment of bank sediments and uprooting of streamside vegetation, increasing bank erosion during flood events and causing reduced protection of banks for several years (Sigafoos, 1964; Keller and Swanson, 1979; Beltaos, 1995, Zabilanksy et al., 2002). In meander bends, both water and flowing ice are carried toward the outer banks by inertial and centrifugal forces (Apmann, 1964). Furthermore, river ice increases irregularities in

channel planform (Ettema and Daly, 2004), partly due to the scouring of channel banks (Lotsari et al., 2015).

Recent advances in understanding mobile river ice has been mostly dedicated to the process of ice jamming and the associated floods (Carr and Vuyovich, 2014; Turcotte et al., 2017; Beltaos, 2018; Lindenschmidt et al., 2018). Some have quantified river ice dynamics (Browne et al., 2019) but have not focused on the interactions between mobile river ice and banks. Other studies have focused on erosion from mobile ice processes but reach-scale studies have not been explicitly addressed until recently (Vandermause, 2018). All studies regarding the erosional effects river ice processes generally agree that quantifying erosion from any one of the many contemporaneous ice and flow processes during the spring thaw is very difficult.

The first numerical and experimental studies of flow through river bends set the theory for forces and dynamics experienced by liquids moving through a river bend and resulted in the scientific recognition of helicoidal flow patterns (Thomson 1879; Darrigol; 2017). Apmann (1964) summarized the experiments, stating that water flowing through bends experiences friction, centrifugal, and inertial forces that causes flow to act as separate lower and upper layers. Because boundary friction has less of an effect on the surface layer, the upper layer of water has the highest velocity and inertia toward the outer bank (Apmann, 1964).

Just as water experiences inertial and centrifugal forces that carry it toward the outer banks of meander bends, solids flowing in water experience similar forces. Frazil river ice flowing around a river bend experiences inertial and centrifugal forces that carry the ice toward the outer bank (Sui et al., 2008). Important factors in determining river ice's arching path through a meander bend are channel geometry, floe concentration, floe shape, and ratio of floe size to channel width (Johnson and Kostras, 1980; Sui et al., 2008). Because more sinuous

channels have tighter bends, a greater flow length in comparison to similar valley lengths, and a higher meander amplitude and shorter wavelength, centrifugal forces cause ice to impact banks more in channels with greater sinuosity.

In this study physical experiments were used to focus on the erosional effects of bank abrasion and gouging from mobile river ice. The effects of abrasion and gouging were studied in channels of planform geometries in relation to ice-bank impact frequencies. Experiments were highly controlled so that all other erosion processes that are typical during the period of ice breakup were not factors in erosion during experimental runs. It was expected that experimental runs with a greater frequency of ice-bank interactions have a greater eroded volume. Further, it was also expected that the frequency of ice-bank interactions are related to planform metrics.

**Methods**

Meander planform can be defined quantitatively by the sinuosity ($S$) (the ratio of flow length ($L_F$) to valley length ($L_V$), meander amplitude ($2A$), bend length ($L_B$) (distance between inflection points or apices), bend radii ($r$), and meander wavelength ($\lambda$) (Guneralp and Marston, 2012; Figure 36). Here, the relationships between the number of ice-bank interactions and these meander planform variables was analyzed through a series of physical experiments. Results were subjected to regression analyses to further describe the relationships between meandering river metrics and ice-bank interactions.

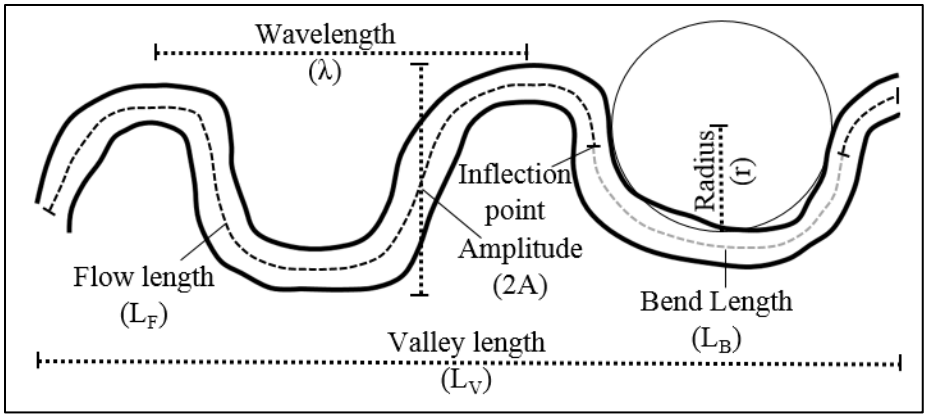


**Figure 36.** Meandering channel planform metrics diagram (adapted from Guneralp and Marston, 2012).

***Physical experiments***

Twelve physical experiments were performed to study ice-bank interactions in channels of varying sinuosities ranging from 1 (straight) to 2.32 (Table 6). A uniform, single phase, equiwidth, semicircular channel with a cross-sectional radius of 5 cm was carved into very fine sand (d = 0.0609 mm) with a critical shear stress of $\tau_c$ = 0.11-0.14 N/m$^2$. In addition, one experimental channel was designed to have a non-uniform meandering planform (Experiment 9). The sand substrate was laid to have a thickness of 10 cm and was leveled using a bubble level. The substrate was made uniform prior to each experiment by inundating it with water and using vibration to settle the sand and remove air pockets. Discharge was held constant at 3.2e$^{-3}$ cfs (5.38 liter per minute) for each of the experiments (Figure 37).

**Table 6.** Meandering planform metrics of river ice experiments

| Experiment No. | Sinuosity (S) | Valley Length (m) | Flow Length (m) | Wavelength (λ) (m) | Amplitude (2A) (m) | Bend Radius (r) (m) | Bend length (LB) (m) |
|---|---|---|---|---|---|---|---|
| **Exp. 1** | 1.00 | 1.89 | 1.89 | NA | NA | NA | NA |
| **Exp. 2** | 1.15 | 1.85 | 2.08 | 0.58 | 0.25 | 0.18 | 1.16 |
| **Exp. 3** | 1.24 | 1.93 | 2.38 | 0.64 | 0.31 | 0.13 | 1.00 |
| **Exp. 4** | 2.32 | 1.86 | 4.03 | 0.40 | 0.45 | 0.09 | 2.23 |
| **Exp. 5** | 2.01 | 1.74 | 3.38 | 0.36 | 0.44 | 0.09 | 1.48 |
| **Exp. 6** | 1.53 | 1.78 | 2.72 | 0.41 | 0.32 | 0.10 | 1.90 |
| **Exp. 7** | 2.30 | 1.84 | 4.23 | 0.38 | 0.50 | 0.09 | 2.34 |
| **Exp. 8** | 1.46 | 1.75 | 2.56 | 0.41 | 0.30 | 0.10 | 1.57 |
| **Exp. 9** | 1.71 | 1.81 | 3.10 | 0.40 | 0.34 | 0.09 | 2.10 |
| **Exp. 10** | 1.00 | 1.78 | 1.78 | NA | NA | NA | NA |
| **Exp. 11** | 1.17 | 1.76 | 2.06 | 0.75 | 0.28 | 0.22 | 1.18 |
| **Exp. 12** | 1.52 | 1.78 | 2.71 | 0.77 | 0.48 | 0.22 | 1.79 |

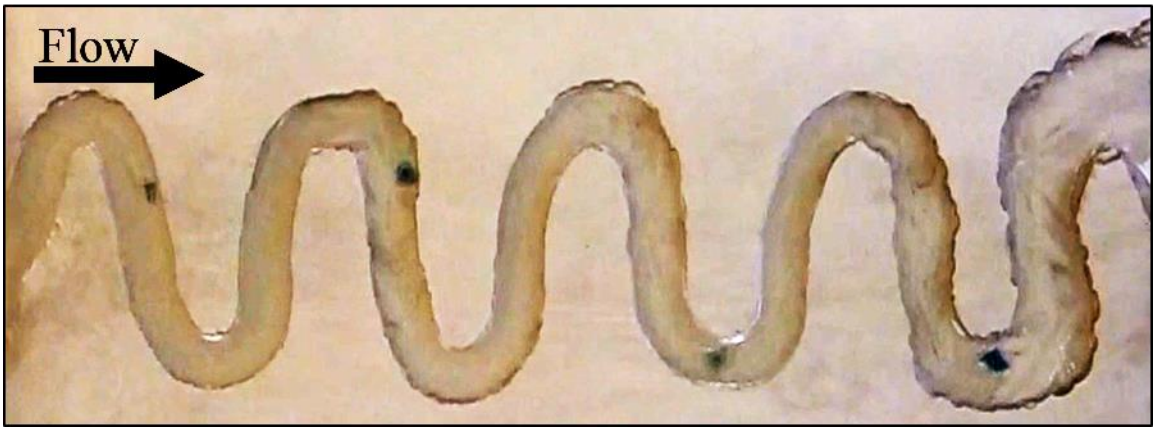


**Figure 37.** Example image of river ice experiment. Geometry and wax platelets (green-black) during Experiment 7. Each channel was diagrammed to fit a specific wavelength and amplitude prior to excavation, resulting in sinuosities ranging from 1 to 2.45.

Experiments were conducted in four, five-minute increments. The first three five-minute periods allowed for erosional stabilization of the channel. Paraffin wax (density = 0.9 g/cm$^3$), used as a substitute for ice, was added during the fourth five-minute period. Throughout the 12 experiments, a total of 208 paraffin wax platelets were added to the experimental channels at 15-

second intervals to simulate mobile river ice (Figure 38). Paraffin platelets were sized to 0.1 to 0.5 channel widths and a thickness of 0.5 cm, with masses ranging from 1.3 to 5.92 g (Table 7).

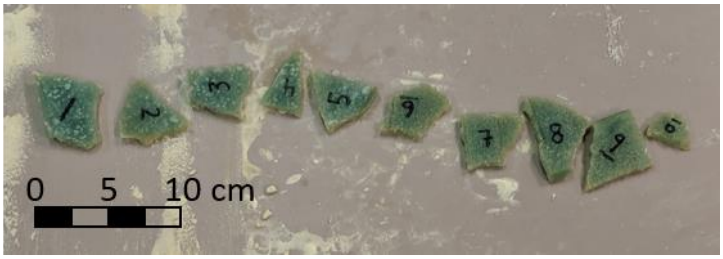


**Figure 38.** Wax platelet image and sizing. Image of the ten paraffin wax platelets designed to simulate river ice in experimental runs.

**Table 7.** Wax platelet addition count and mass

| Wax/Ice Block Identifier | No. of Additions | Mass (g) |
|---|---|---|
| 1 | 18 | 5.92 |
| 2 | 22 | 3.54 |
| 3 | 24 | 3.95 |
| 4 | 22 | 2.45 |
| 5 | 21 | 3.51 |
| 6 | 24 | 3.4 |
| 7 | 24 | 3.72 |
| 8 | 19 | 4.99 |
| 9 | 16 | 4.95 |
| 10 | 18 | 1.3 |

***Channel planform measurements***

Metrics for channel planforms were measured in ArcMap 10.7 using Orthoimagery of the final channel geometry for each experimental run. Measurements included the wavelength ($\lambda$), amplitude ($A$), bend radius ($r$), bend length ($L_B$), flow length ($L_F$), valley length ($L_V$), and sinuosity ($L_F/ L_V$) (Figure 36). In addition to those traditional meandering river planform metrics, the number of bends (B), bends per flowlength ($B_L$), and ratio of bend length to straight length (BSL) were also included in statistical modeling.

### *Ice-bank impact mapping*

Ice-bank impacts were mapped as points in ESRI ArcMap 10.7 using video records. Attributes were assigned to each point with the identifying number for each wax platelet, the mass of each wax platelet, and which bank (inner or outer) were impacted by the platelets in bends, or whether the impact occurred in a straight. Here, straights are defined as the length of channel between the downstream apex of each bend and the upstream apex of the next downstream bend. Ice-bank impact density maps were created for each experiment run using the Point Density Tool.

Counts of bank impacts were normalized to the number of blocks added to the channel in each experiment and the bank length for each experiment, resulting in the Impacts per Block per Bank length (IBB) variable. The creation of the IBB variable allowed for comparison between experiment runs with varying numbers of ice block additions and varying flow lengths. The independent variables were subjected to a multiple linear regression to determine which variables explained most of the variance in the dependent impacts per block per flow length variable.

### *Erosion mapping*

Erosion was measured for five of the 12 experiments by conducting Structure-from-Motion Photogrammetry for series of photos captured between each of the five-minute periods, prior to the start of each experiment run, and at the end of each experiment run. Agisoft Metashape was used to create Digital Elevation Models (DEM's) from photogrammetry data. Eroded volumes and DEM's of Difference (DoD) for each period were calculated through use of the Geomorphic Change Detection Software (Wheaton et al., 2010) set at a 1 cm detection threshold to account for possible errors in the DEM surfaces.

## Results

Overall, 280 wax platelet ice blocks were sent through the 12 experimental channels, resulting in 1,822 ice-bank impacts for averages of 151 ice-bank impacts per experiment and 6.35 impacts per block (Figure 39). More massive blocks were found to impact banks more frequently than smaller blocks (Figure 40). Erosion was monitored for five of the 12 experiments and eroded areas and volumes relate to the location and frequency of ice-bank interactions.

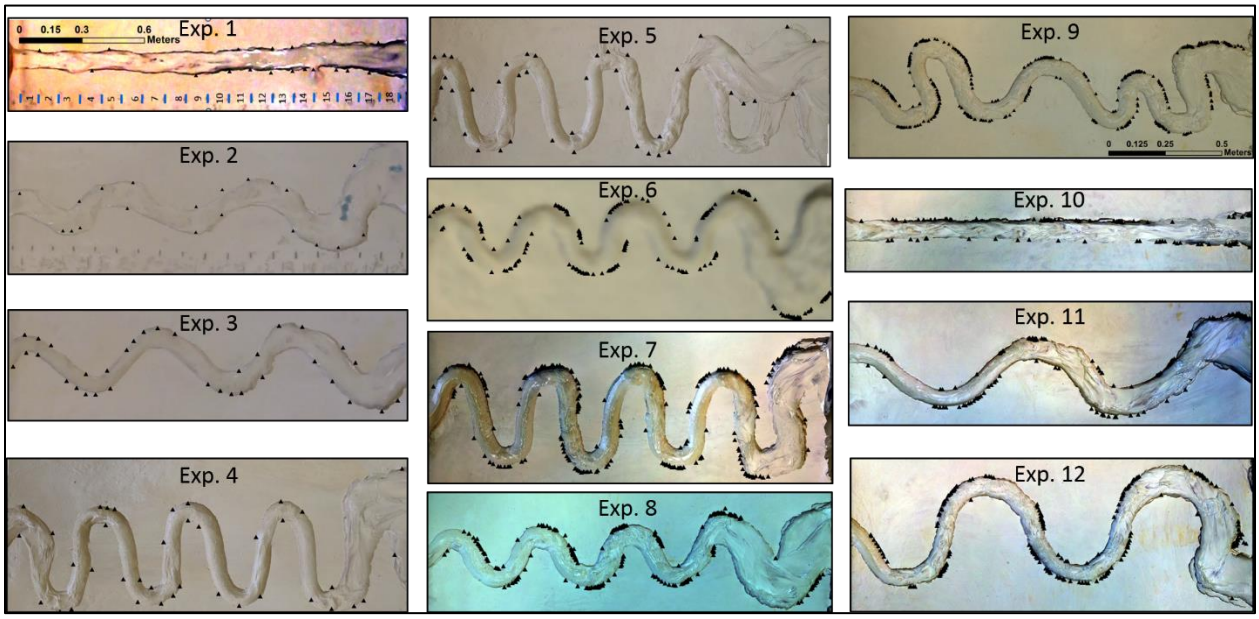


**Figure 39.** Mapped ice-bank impact locations. Shown are ice-bank impact locations (black points) for the 12 experimental channels. In tight bends, ice impacts tend to cluster and in gradual bends are dispersed throughout the bend.

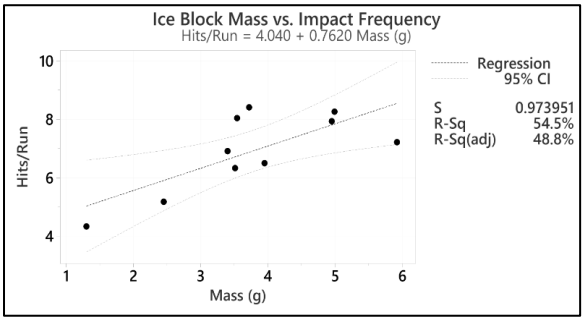


**Figure 40.** Experimental ice block mass vs impact frequency regression. Scatter plot and regression of ice block mass and impact frequency showing a moderate positive relationship. This relationship demonstrates that more massive blocks of ice impact the banks more frequently.

### *Ice-bank impact locations*

Most ice-bank impacts occur on the outer banks within bends (Figures 41 and 42). Of the 1,822 ice-bank impacts, 74% (1,342) of impacts occurred in river bends and 26% (480) occurred in straights. Of the total number of ice-bank interactions, 67% (1,215) occurred at the outer bank of bends and only 7% (127) occurred at the inner bank. There was no relationship between sinuosity and where ice-bank interactions occur, meaning that regardless of sinuosity there are similar proportions of ice-bank interactions that occur at the outer bank, inner bank, and within straights. Sinuosity does impact the density of impacts where ice-bank impacts tend to cluster in tight bends while being more dispersed in bends with greater radii.

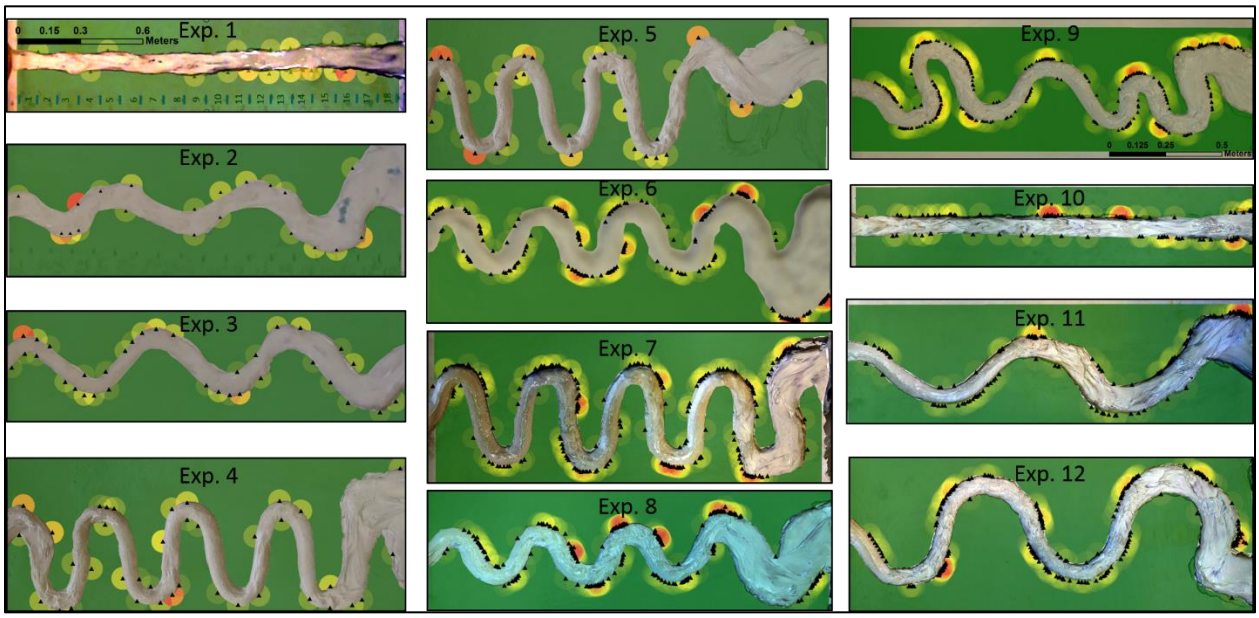


**Figure 41.** Experimental ice-bank interaction heat maps. Shown are density maps for each of the 12 experimental runs. The green-to-red color scheme indicates areas of few/no ice-bank impacts (green), areas with medial impact frequencies (yellow), and high-frequency impact areas (red). High-frequency areas are mostly located at the outer banks of channel bends, clustered in tight bends and dispersed in gradual bends.

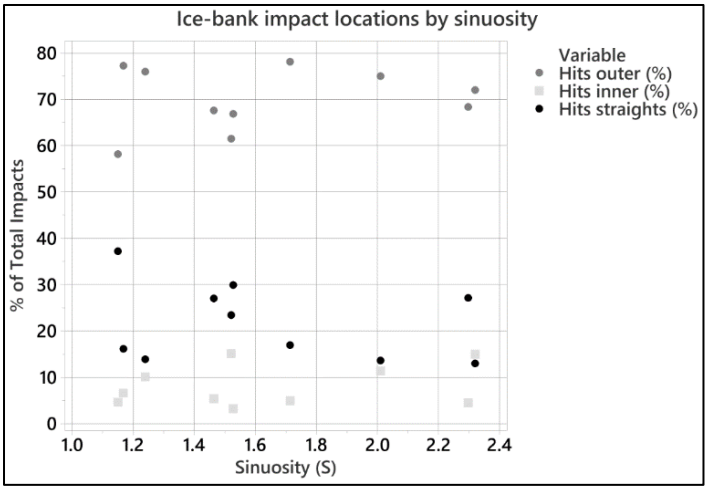


**Figure 42.** Ice-bank impact locations by sinuosity. Graph of ice-bank impact locations showing that at least 58% of ice-bank interactions occur on the outer banks within river bends for each of the experimental runs.

### *Channel geometry metrics and ice-bank impact frequency*

At the 95% Significance Level, of the five channel geometry metrics tested, bend length was the only independent variable to have a significant relationship with the IBB variable ($P = 0.018$) (Figure 43). After the bend length, the next strongest relationships existed between the IBB variable and the wavelength, amplitude, and bend radius (standardized coefficients of 1.24, 1.9, and 3.21, respectively) but their relationships were not significant ($P > 0.05$). A multiple linear regression test performed using the included five geometric variables was able to describe 81.5% of variance in the IBB variable.

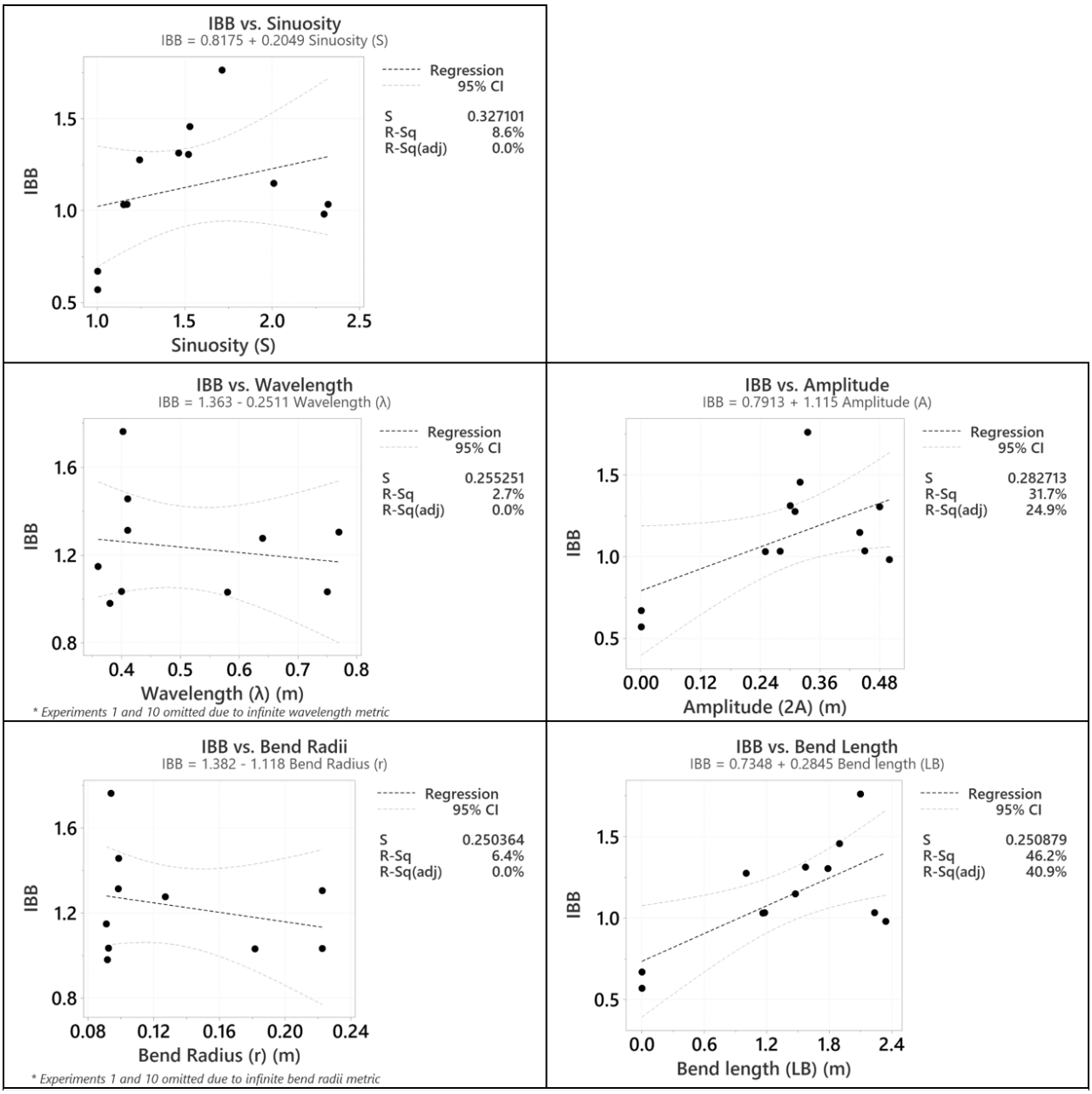


**Figure 43.** Regressions: IBB vs. planform metric. Planform metrics include sinuosity, wavelength, amplitude, bend radius, and bend length variables. Given the input variable, the regression analysis was able to account for 81.5% of variance in the IBB variable.

### *Ice-bank impacts and erosion*

Although experimental periods of ice additions were expected to show significantly more erosion than the final stabilization period, no significant difference was determined (P = 0.97). Not one experiment showed the expected pattern of decreasing eroded volumes through the

stabilization periods and then a higher eroded volume during the period of ice addition (Figure 44). The patterns of erosion were not consistent between the runs, with one run showing a constant decrease in erosion (run 8) or a decrease after the first stabilization period (run 11), one showing an increase in erosion until the ice blocks were added (run 12) and two showing variability in erosion for each period (runs 9 and 10). The two runs that showed this variability (runs 9 and 10) are the only two where erosion appears to have increased after ice was added, but the overall trend is not conclusive.

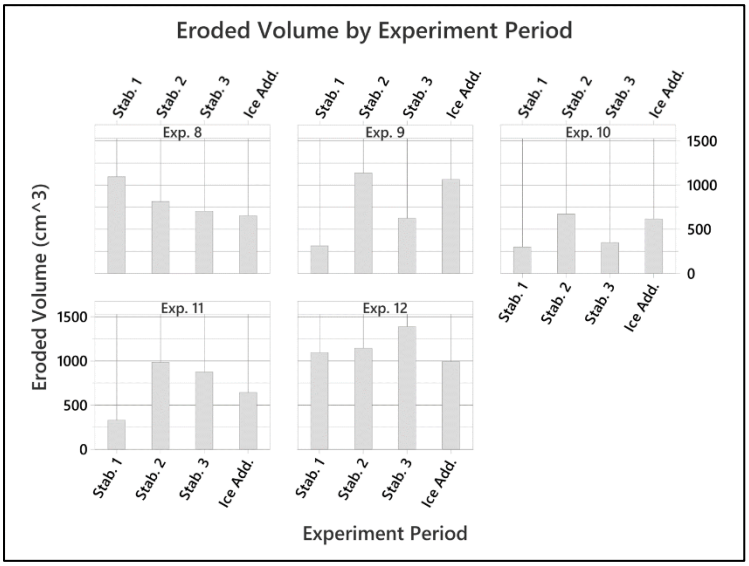


**Figure 44.** Eroded volume by 5-minute experiment period. Shown are each of the five experiments for which erosion was monitored. Periods of ice addition were expected to cause a greater eroded volume than the final stabilization period, but did not (P = 0.97).

The experimental runs for which erosion was studied generally showed erosion at areas of clustered ice-bank impacts, and deposition in the channel bed either a) immediately adjacent to the locations of ice-bank impacts or b) at the downstream side of the inner bank of the next bend (Figure 45). Erosion calculations were thresholded at 1 cm to remove erroneous values sourced from overlaying of terrain models. Digital animations of erosion throughout experimental periods can be found in Appendix D.

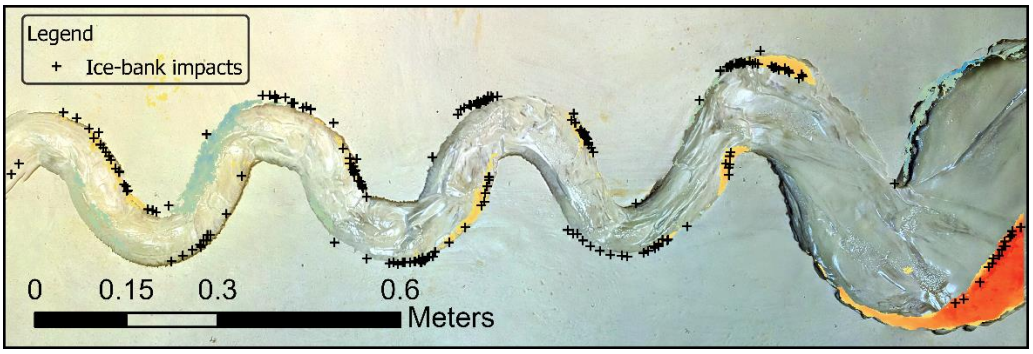


**Figure 45.** River ice experiment erosion and deposition areas. Example of eroded areas (yellow-red) and depositional areas (green-blue) for Experiment 8. Areas of erosion generally coincide with concentrated areas of ice-bank impacts. Areas of deposition are most common at the toe of the inner bank downstream of areas with concentrated ice-bank impacts.

When comparing channel planform metrics and IBB variable to the eroded volumes during the ice addition period of Experiments 8-12, eroded volume shows the strongest relationships with sinuosity (R-squared = 69%, P = 0.08), IBB (R-squared = 63%, P = 0.11), bend length (R-squared = 55%, P = 0.15), and amplitude (R-squared = 45%, P = 0.21) but were insignificant at the 95% confidence interval (Figure 46). The relationships between eroded volume and the sinuosity, IBB, bend length, and amplitude were each weak to moderate positive relationships. The wavelength and bend radii variables had no relationship with the eroded volume during the period of ice addition.

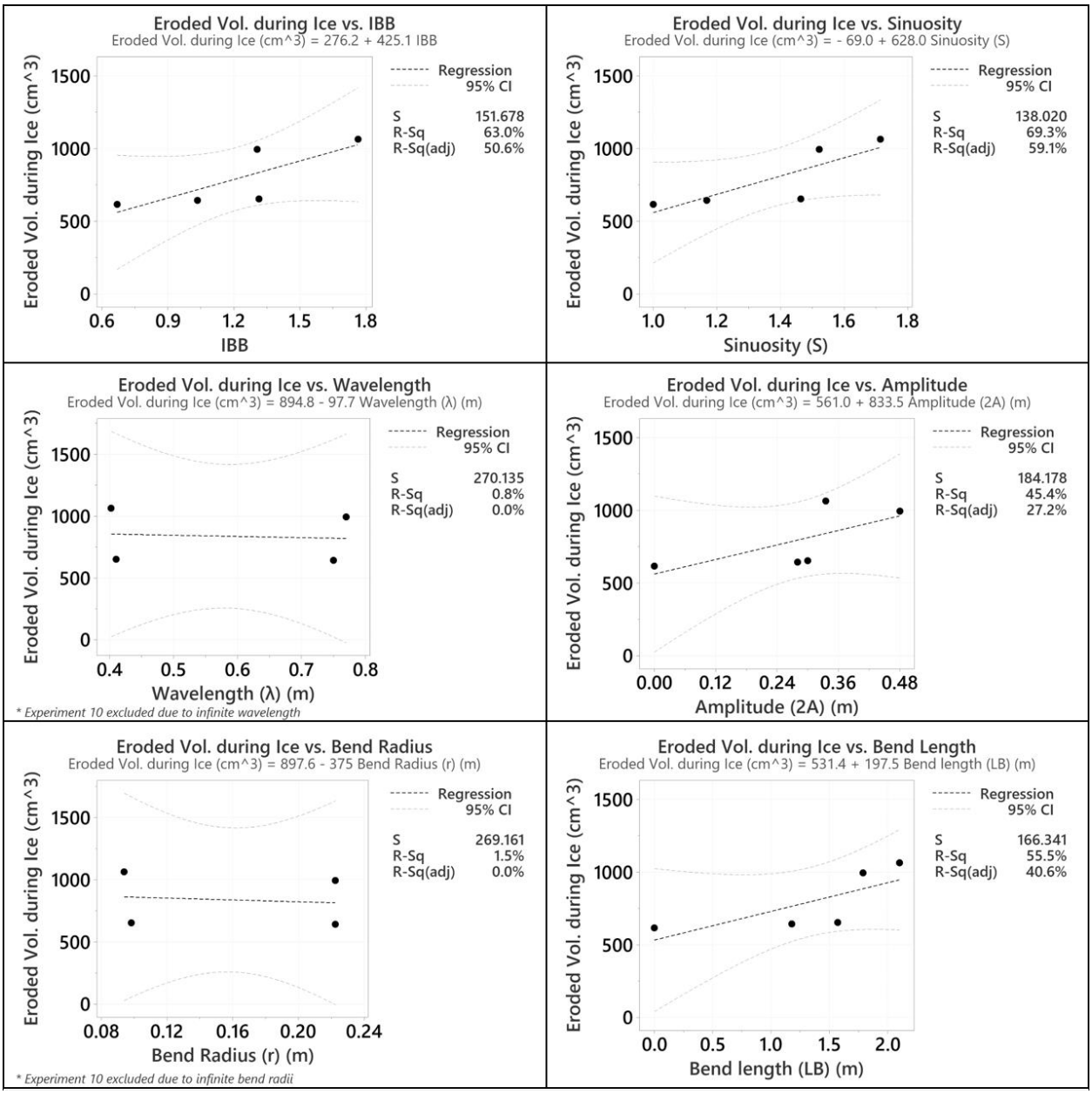


**Figure 46.** Regressions: Eroded volume vs IBB and planform metrics. Regressions of eroded volume during ice addition period versus channel planform metrics and IBB variable. Weak to moderate positive relationships exist between

Results for erosion may be complicated by the processes of channel incision and widening at the downstream outlet of the experimental basin. For each of the experiments, the most significant area of erosion was in the area of incision and widening. Although incision and widening were persistent throughout the five experiments, it likely complicates the volume calculation when attempting to quantify the effect of river ice.

## Discussion

### *Challenges in quantifying erosion due to mobile river ice*

Mobile river ice is acknowledged as an important factor in river bank erosion by gouging and abrasion (Borland, 1959; Smith, 1979; Doyle, 1988; Brooks, 1993; Wuebben, 1995; MacKay and MacKay, 1977; Lotsari et al., 2015), but ice also contributes to bank erosion by bankfast ice loading or heaving (Ettema, 2002; Zabilansky, 2002), and freeze-thaw processes (Anderson et al., 1978; Ferrick and Gatto, 2005; Dagesse, 2013; Edwards, 2013). During the spring thaw, floods occur simultaneously with river ice breakup and floe to compound differentiation between erosion caused by the two. During this period, floodwaters also erode banks, and channels are highly susceptible to shifting due to ice jamming or grounding (Beltaos, 1995; Smith and Pearce, 2002).

The list of processes above demonstrates the challenges in quantifying the overall effect of mobile river ice impacts on bank erosion in meander loops (Zabilansky et al., 2002; Vandermause, 2018). Those challenges were observed as the expected temporal patterns of erosion over the course of experiments were not observed clearly in each of the experiments, but when summing the five experiments the expected pattern of more erosion during ice addition periods was observed.

### *Ice-bank impact forces*

Detailed video evidence of experiments shows obvious erosion due to the impact of wax against banks, and numeric estimates of fluid and critical shear stresses and ice impact forces to differentiate between erosion caused by ice or water. It is estimated that the very fine sand used in these experiments was not eroded by fluid shear stress in areas where incision and widening

were not obvious. With a semicircular channel with a 3.5 cm radius and a slope of 0.001 (measured from elevation models), the fluid shear stress of these experiments ($\tau$ = 0.109 N/m$^2$) is slightly less than the critical shear stress of the very fine sand ($\tau_c$ = 0.11-0.143 N/m$^2$).

The force of impact of a single piece of river ice can be estimated using the impact force equation that is dispersed over the length of impact, divided into vectors for the x- and y-direction (Figure 47). In nature, it is estimated that forces exerted would be largely compounded because of higher ice concentrations in river ice floes.

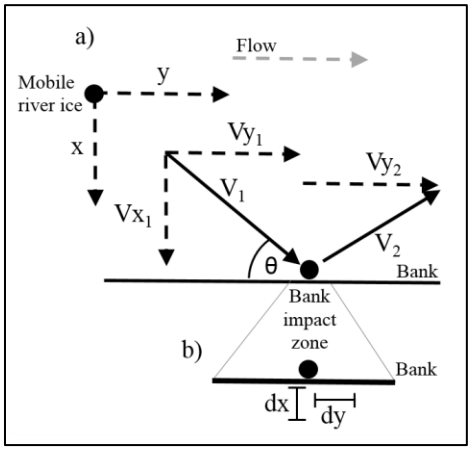


**Figure 47.** Ice bank impact force diagram. Velocities and forces are designated in the x- (bankwise) and y-direction (downstream) directions to calculate the bank-normal and shear forces of ice-bank impacts.

Thus, if y denotes the block's location in the downstream direction and x denotes its location in the lateral direction, the velocities can be broken down into x- and y-vectors as related to the angle of approach toward the bank. Considering the angle of approach ($\theta$), the velocity in the x- and y-direction are calculated as:

$$v_x = V \sin(\theta) \qquad \text{(Equation 12)}$$

and

$$v_y = V \cos(\theta) \quad . \qquad \text{(Equation 13)}$$

Calculation of velocity vectors using Equations 12 and 13 above allows for the total impact force, F, in the x- and y-direction to be calculated as:

$$F = \frac{1}{2}\left(\frac{mv_x}{d_x}\right) + \frac{1}{2}\left(\frac{m(v_{y1}-v_{y2})}{d_y}\right) \quad \text{(Equation 14)}$$

where m is the ice block's mass, $v_x$ and $v_y$ are velocities in the x- and y-directions (with $v_{y1}$ and $v_{y2}$ as the velocity before and after the bank impact, respectively), and $d_x$ and $d_y$ are the distance over which the collision occurs. Terms to the left of the addition sign in Equation 14 describe the bank-normal force and terms after describe the impact force in the downstream direction. Equation 14 lacks a velocity term for the x-direction after bank impact because it is assumed that the ice block stops its progress in the x-direction when impacting the bank.

Equation 14 produces forces that, for a single ice block, depend on 1) the velocity of ice blocks in relation to the bank its impacting, 2) its angle of approach (which affect x and y velocities, and 3) the distances of deceleration that a block experiences when impacting the bank. As applied to this study, if a wax block of average mass (m = 3.77 g) were moving with a velocity of 0.147 m/s (similar to that of flow), and an approach angle of 30° and impacts the bank, penetrating 0.5 mm into the bank and dragging along the bank for 3 mm while slowing to 50% its initial velocity, the resulting force exerted on the area of bank effected by the impact is 0.002 N in the x-direction and 0.001 N in the y-direction. Although these numbers are low, video evidence (not pictured here) from experiments shows the abrasion of bank sediments by river ice and stable conditions under only flowing water.

At field scale, river ice impact force on submerged bridge piers in South Dakota measured over two years ranged between 22,240 and 489,304 N (Pei et al., 2017). The results of Pei et al., (2017), are in the case of a direct impact, under conditions of possible ice jams, and also include the force of flowing water. These forces, exerted on a 0.39 $m^2$ area of a force

transducer, lead to shear stresses of 8.8 to 193 kPa. These stresses exceed the shear strength of most unconsolidated alluvial sediments and would cause their displacement.

***Planform metrics, ice-bank interactions, and bend evolution***

Planform metrics can be used to explain the frequency of ice-bank interactions using classical physics equations. For example, the angular momentum equation

$$L = rmv, \quad \text{(Equation 15)}$$

where $L$ is the angular momentum, $r$ is radius, $m$ is ice block mass, and $v$ is velocity, can explain 1) the relationship between bend length and IBB, 2) more frequent ice-bank interactions by more massive wax blocks, and 3) more frequent impacts at the outer banks of bends.

The centrifugal force equation,

$$F = mv^2/r, \quad \text{(Equation 16)}$$

where $F$ is centrifugal force, $m$ is ice block mass, $v$ is velocity, and $r$ is the bend radius, explains why tighter bends lead to a higher IBB. Bends with lower radii have a greater centrifugal force, assuming constant mass and velocity, causing the acceleration of ice toward the outer bank. It is also understood that river planform can be used to describe flow deflection toward outer banks downstream of bend exits (Nouh and Townsend, 1979). With flow carrying river ice in directions very similar to flow (Browne et al., 2019), ice impacts the banks in similar locations as where flow erodes banks.

Knighton (1998) diagrammed the various ways that channel bends erode. Variation in the distribution of fluid shear stress around the bend controlled how bends evolved, either by translation, rotation, extension, or by lobing (compound growth). Ice-bank interactions, being clustered in some areas is expected to cause lobing and compound growth of bends experiencing

clustered ice impacts. Bends with dispersed ice impacts is estimated to cause the translation or rotation of bends due to its nature to impact bends on the outside bank of the bend's exit.

## Conclusions

These results lead to the expectation that reaches with tight and long river bends and a high sinuosity metric experience the most erosion caused by river ice. River ice impacting outer banks of channels accelerates river bank erosion and meandering during the spring thaw, driving the increase of sinuosity in temperate and polar rivers.

Periods when mobile river ice floes are progressing through river systems cause more erosion than periods without erosion. In natural river systems, high concentrations of ice floes are sure to exaggerate the results found by this study. Numerical comparisons of fluvial forces and ice abrasion forces support the result of ice being a significant contributor to bank erosion.

Quantifying the contribution of river ice is difficult due to contemporaneous erosion processes. Here, the quantification was complicated by the processes of incision and widening at the basin outlet. It is suggested that further work focus on the stable areas of channel by omitting such reaches from results.

# CHAPTER V: CONCLUSIONS

## Significant contributions

Work performed as part of this dissertation has contributed tools and knowledge to the study of post-glacial rivers, important factors that influence them, and has contributed important knowledge as to the initial establishment of rivers on post-glacial landscapes. Regionally, this work has developed a finer understanding of the influence of glacial deposits and topography on the morphology of the Red River. This work has contributed new tools to studying rivers and fluvial geomorphology using computers, specifically the MC Mapper tool and Landlab methods for creating paleotopographies, tilting landscapes, and mapping channel paths in raster format. In terms of river ice, this study begins the complex process of dividing the effects of many contemporaneous processes during the spring thaw that are key to understanding how climate change effects thawing rivers in the future.

## Limitations and future work

Some limitations exist related to the work performed in this dissertation. First, the MC Mapper GIS tool requires the availability of high-resolution DEM's. These DEM's do not typically cover large spatial scales and when using MC Mapper it is important that data collection methods are uniform over the length of the study area. MC Mapper has not yet been tested on rivers outside of the Lake Agassiz plain and Red River Valley, so further testing is recommended before making wide use of the tool.

Second, limitations existed in the flow routing methods applied within Landlab to model channel path changes. The glacial uplands feature many closed depressions in the form of pothole lakes. The Landlab script applied in this study fills sinks and routes flow via the D8

routing method, which is a simplification of the hydrologic system that exists in western Minnesota. Further work should aim toward improving flow routing methods and being able to account for subsurface flow that is known to connect many pothole lakes.

Finally, the calculation of erosion from ice abrasion for each experiment was complicated by multiple limitations. Those limitations stemmed from experimental design and methodology flaws which in future mobile river ice studies should be addressed. Further experiments should ensure a greater difference between the fluvial shear stress of the discharge added to the experimental channel and the critical shear stress required for erosion of substrate. These adjustments are necessary to more clearly determine that erosion is only occurring by ice abrasion and not by flowing water. The outlet for further experiments needs to be controlled so that incision and widening does not influence the calculation of erosion and deposition volumes. To emphasize erosion caused by ice, a greater concentration of ice should be added to the channel which is more closely representative of the natural system. A material other than paraffin wax should be used that is more similar to the density of river ice. Further, it is recommended that more easily repeatable 3D modeling procedures be used to replace the small-scale structure-from-motion used here because it is very difficult to align repeated scans of the same surface.

**Summary**

This study has contributed to the overall understanding of spatial and temporal variations in the processes that shape post-glacial rivers established on low-relief landscapes. Results demonstrate the spatial and temporal variations in susceptibility to erosion due to pre-set conditions, like surficial geology and palimpsest conditions, and outside forcings such as tilting

from GIA or mobile river ice abrasion and gouging. Highlights of this work display the following general conclusions:

- Spatial variations in the pre-set conditions formed by glacial deposition and overprinted by glaciolacustrine Lake Agassiz clays causes morphologic variations in meander cutoff relief and river incision presently observable using morphometric techniques. Provided here is an automated method of mapping meander cutoffs at the river-scale that shows that more erodible glacial moraines, as compared to clays, allow for greater net incision and more meandering which leads to the formation of more meander cutoffs in river reaches established atop moraines deposited in the late-Wisconsinan during the recession of the Des Moines and Red River Lobes of the LIS.
- In low relief landscapes with no incised river valleys, channel avulsions occur more frequently and with greater length in modeling scenarios with low incision rates, during rapid periods of tilting due to GIA. Landscape roughness is significant in determining the character of channel path changes, showing abrupt avulsions in rough landscapes and gradual shifts in smoothed landscapes.
- In meandering channels, ice most frequently impacts the outer banks of meander bends. Channel planform in the form of bend length significantly effects the frequency of ice impacting banks. Other planform metrics such as sinuosity, bend radius, and wavelength also show relationships with the frequency of ice impacts on banks. Mobile river ice is a significant factor in causing erosion during the spring thaw, but observation of this process is difficult because of contemporaneous occurrence with other erosion processes.

## REFERENCES


Adams, J., 1980. Active tilting of the United States midcontinent: Geodetic and geomorphic evidence. *Geology*, 8(9), pp.442-446.

Alexander, J., Bridge, J.S., Leeder, M.R., Collier, R.E. and Gawthorpe, R.L., 1994. Holocene meander-belt evolution in an active extensional basin, southwestern Montana. *Journal of Sedimentary Research*, 64(4b), pp.542-559.

Anderson, D.M., R. Pusch and E. Penner, 1978. Physical and thermal properties of frozen ground. In *Geotechnical Engineering for Cold Regions* (O.B. Andersland and D.M. Anderson, Ed.), Chapter 2, p. 37–102. New York: McGraw-Hill Book Co.

Andres, D., Jasek, M. and Fonstad, G., 2005. Field and theoretical study of the toe region of a consolidated ice cover. *Proc. 13th Wksp. on River Ice*, pp.16-18.

Apmann, R.P., 1964. A case history in theory and experiment: Fluid flow in bends. *Isis*, 55(4), pp.427-434.

Arbogast, A.F., Bookout, J.R., Schrotenboer, B.R., Lansdale, A., Rust, G.L. and Bato, V.A., 2008. Post-glacial fluvial response and landform development in the upper Muskegon River valley in North-Central Lower Michigan, USA. *Geomorphology*, 102(3-4), pp.615-623.

Archuleta, C.M., Constance, E.W., Arundel, S.T., Lowe, A.J., Mantey, K.S., and Phillips, L.A., 2017. The National Map seamless digital elevation model specifications: *U.S. Geological Survey Techniques and Methods*, book 11, chap. B9, 39 p., https://doi.org/10.3133/tm11B9.

Arnborg, L., Walker, H.J. and Peippo, J., 1967. Suspended load in the Colville river, Alaska, 1962. Geografiska Annaler: Series A, *Physical Geography*, 49(2-4), pp.131-144.

Arndt, Michael B., 1975. "Stratigraphy of offshore sediment of Lake Agassiz, North Dakota," *Theses and Dissertations*. 7.

Ashworth, A.C., Clayton, L. and Bickley, W.B., 1972. The Mosbeck site: a paleoenvironmental interpretation of the late Quaternary history of Lake Agassiz based on fossil insect and mollusk remains. *Quaternary Research*, 2(2), pp.176-188.

Aslan, A., Autin, W.J. and Blum, M.D., 2005. Causes of river avulsion: insights from the late Holocene avulsion history of the Mississippi River, USA. *Journal of Sedimentary Research*, 75(4), pp.650-664.

Barnes, N., Luffman, I. and Nandi, A., 2016. Gully erosion and freeze-thaw processes in clay-rich soils, northeast Tennessee, USA. *GeoResJ*, 9, pp.67-76.

Barnett, P.J., Sharpe, D.R., Russell, H.A.J., Brennand, T.A., Gorrell, G., Kenny, F. and Pugin, A., 1998. On the origin of the Oak Ridges Moraine. *Canadian Journal of Earth Sciences*, 35(10), pp.1152-1167.

Belmont, P., 2011. Floodplain width adjustments in response to rapid base level fall and knickpoint migration. *Geomorphology*, 128(1-2), pp.92-102.

Beltaos, S. ed., 1995. River ice jams. *Water Resources Publication*.

Beltaos, S., 1997. Onset of river ice breakup. *Cold Regions Science and Technology*, 25(3), pp.183-196.

Beltaos, S., 2003. Threshold between mechanical and thermal breakup of river ice cover. *Cold Regions Science and Technology*, 37(1), pp.1-13.

Beltaos, S., 2018. Frequency of ice-jam flooding of Peace-Athabasca Delta. *Canadian Journal of Civil Engineering*, 45(1), pp.71-75.

Beltaos, S., Carter, T., Rowsell, R. and DePalma, S.G., 2018. Erosion potential of dynamic ice breakup in Lower Athabasca River. Part I: Field measurements and initial quantification. *Cold Regions Science and Technology*, 149, pp.16-28.

Bierman, P.R., Marsella, K.A., Patterson, C., Davis, P.T. and Caffee, M., 1999. Mid-Pleistocene cosmogenic minimum-age limits for pre-Wisconsinan glacial surfaces in southwestern Minnesota and southern Baffin Island: a multiple nuclide approach. *Geomorphology*, 27(1-2), pp.25-39.

Blair, T.C. and McPherson, J.G., 1994. Historical adjustments by Walker River to lake-level fall over a tectonically tilted half-graben floor, Walker Lake Basin, Nevada. *Sedimentary geology*, 92(1-2), pp.7-16.

Blanckaert, K. and de Vriend, H.J. 2004. Secondary flows in sharp open-channel bends. *Journal of Fluid Mechanics* 498:353-380

Bluemle, J.P., 1977. Face of North Dakota - The Geologic Story, *Educational Series 11*, North Dakota Geological Survey

Boellstorff, J., 1978. North American Pleistocene stages reconsidered in light of probable Pliocene-Pleistocene continental glaciation. *Science*, 202(4365), pp.305-307.

Bofinger, J. and Hesse, R., 2011. As far as the laser can reach… Laminar analysis of LiDAR detected structures as a powerful instrument for archaeological heritage management in Baden-Württemberg, Germany, Cowley (ed.), *Remote Sensing for Archaeological Heritage Management*, EAC Occasional Paper No. 5, 163-173.

Bogoni, M., Putti, M. and Lanzoni, S., 2017. Modeling meander morphodynamics over self-formed heterogeneous floodplains. *Water Resources Research*, 53(6), pp.5137-5157.

Borland, W.M., 1959. Sediment problems of the lower Colorado River. Series 2: Indexed reports; *Subseries 1: Sedimentation reports*.

Boulton, G.S. and Paul, M.A., 1976. The influence of genetic processes on some geotechnical properties of glacial tills. *Quarterly Journal of Engineering Geology*, 9(3), pp.159-194.

Boyd, K.F., Schumm, S.A., 1995. Geomorphic evidence of deformation in the northern part of the New Madrid seismic zone. *U.S. Geol.Surv. Prof. Pap*. 1538-R,35 pp.

Breckenridge, A., 2015. The Tintah-Campbell gap and implications for glacial Lake Agassiz drainage during the Younger Dryas cold interval. *Quaternary Science Reviews*, 117, pp.124-134.

Brevik, E.C. and Reid, J.R., 2000. Uplift-based limits to the thickness of ice in the Lake Agassiz basin of North Dakota during the Late Wisconsinan. *Geomorphology*, 32(1-2), pp.161-169.

Bridge, J.S., Smith, N.D., Trent, F., Gabel, S.L. and Bernstein, P., 1986. Sedimentology and morphology of a low-sinuosity river: Calamus River, Nebraska Sand Hills. *Sedimentology*, 33(6), pp.851-870.

Brooks, G.R., 1993. Characteristics of an ice-scoured river bank near Keele River confluence, Mackenzie Valley, Northwest Territories. *Papers-Geological Survey of Canada*, pp.39-39.

Brooks, G.R., 2003a. Holocene lateral channel migration and incision of the Red River, Manitoba, Canada. *Geomorphology*, 54(3), pp.197-215.

Brooks, G.R., 2003b. Alluvial deposits of a mud-dominated stream: the Red River, Manitoba, Canada. *Sedimentology*, 50(3), pp.441-458.

Brooks, G.R., 2005. Overbank deposition along the concave side of the Red River meanders, Manitoba, and its geomorphic significance. *Earth Surface Processes and Landforms*, 30(13), pp.1617-1632.

Brooks, G.R., 2017. Red River Valley, Manitoba: The Geomorphology of a Low-Relief, Flood-Prone Prairie Landscape. In *Landscapes and Landforms of Western Canada* (pp. 143-155). Springer, Cham.

Brown, E.T., Stallard, R.F., Larsen, M.C., Bourlès, D.L., Raisbeck, G.M. and Yiou, F., 1998. Determination of predevelopment denudation rates of an agricultural watershed (Cayaguas River, Puerto Rico) using in-situ-produced 10Be in river-borne quartz. *Earth and Planetary Science Letters*, 160(3-4), pp.723-728.

Browne, T., Vouk, I., Cornett, A., Watson, D., Murphy, E. and Sayed, M., 2019. Numerical Simulation of Ice Dynamics on the St. Lawrence River at Montréal. In *Proceedings of the 20$^{th}$ Workshop on the Hydraulics of Ice Covered Rivers*, Ottawa, Ont., Canada

Burnett, A.W. and Schumm, S.A., 1983. Alluvial-river response to neotectonic deformation in Louisiana and Mississippi. *Science*, 222(4619), pp.49-50.

Camporeale, C., Perucca, E. and Ridolfi, L., 2008. Significance of cutoff in meandering river dynamics. *Journal of Geophysical Research: Earth Surface*, 113(F1).

Carr, M.L. and Vuyovich, C.M., 2014. Investigating the effects of long-term hydro-climatic trends on Midwest ice jam events. *Cold Regions Science and Technology*, 106, pp.66-81.

Chamberlin, E.P. and Hajek, E.A., 2015. Interpreting paleo-avulsion dynamics from multistory sand bodies. *Journal of Sedimentary Research*, 85(2), pp.82-94.

Chamberlin, E.P., Hajek, E.A. and Trampush, S.M., 2016. Measuring scales of autogenic organization in fluvial stratigraphy: An example from the Cretaceous Lower Williams Fork Formation, Colorado. *SEPM Special Publications*, 106, pp.132-144.

Clark, P.U., Marshall, S.J., Clarke, G.K., Hostetler, S.W., Licciardi, J.M. and Teller, J.T., 2001. Freshwater forcing of abrupt climate change during the last glaciation. *Science*, 293(5528), pp.283-287.

Clayton L., Moran S.R., 1982. A Glacial Process-Form Model. In: Coates D.R. (eds) *Glacial Geomorphology*. Springer, Dordrecht

Colgan, P.M., Mickelson, D.M. and Cutler, P.M., 2003. Ice-marginal terrestrial landsystems: southern Laurentide Ice Sheet margin. *Glacial landsystems*. London: Arnold, pp.111-142.

Constantine, C.R., Dunne, T. and Hanson, G.J., 2009. Examining the physical meaning of the bank erosion coefficient used in meander migration modeling. *Geomorphology*, 106(3-4), pp.242-252.

Constantine, J.A. and Dunne, T., 2008. Meander cutoff and the controls on the production of oxbow lakes. *Geology*, 36(1), pp.23-26.

Constantine, J.A., Dunne, T., Ahmed, J., Legleiter, C. and Lazarus, E.D., 2014. Sediment supply as a driver of river meandering and floodplain evolution in the Amazon Basin. *Nature Geoscience*, 7(12), p.899.

Constantine, J.A., McLean, S.R. and Dunne, T., 2010. A mechanism of chute cutoff along large meandering rivers with uniform floodplain topography. *Geological Society of America Bulletin*, 122(5-6), pp.855-869.

Cook, H., 2018. River channel planforms and floodplains: a study in the Wessex landscape. *Landscape History*, 39(1), pp.5-24.

Cooley, S.W. and Pavelsky, T.M., 2016. Spatial and temporal patterns in Arctic river ice breakup revealed by automated ice detection from MODIS imagery. *Remote Sensing of Environment*, 175, pp.310-322.

Cordier, S., Adamson, K., Delmas, M., Calvet, M. and Harmand, D., 2017. Of ice and water: Quaternary fluvial response to glacial forcing. *Quaternary Science Reviews*, 166, pp.57-73.

Costa, P.J.M., 2016. Sediment Transport. In: Kennish M.J. (eds) Encyclopedia of Estuaries. *Encyclopedia of Earth Sciences Series*. Springer, Dordrecht.

Curran, J.H., Loso, M.G. and Williams, H.B., 2017. Glacial conditioning of stream position and flooding in the braid plain of the Exit Glacier foreland, Alaska. *Geomorphology*, 293, pp.272-288.

Cusick, J.A., 2001. Foliar nutrients in black cottonwood and Sitka alder along a soil chronosequence at Exit Glacier, Kenai Fjords National Park, Alaska. Doctoral dissertation, University of Alaska Anchorage.

Dagesse, D.F., 2013. Freezing cycle effects on water stability of soil aggregates. *Canadian Journal of Soil Science*, 93(4), pp.473-483.

de Quay, G.S., Roberts, G.G., Rood, D.H. and Fernandes, V.M., 2019. Holocene uplift and rapid fluvial erosion of Iceland: A record of post-glacial landscape evolution. *Earth and Planetary Science Letters*, 505, pp.118-130.

Dietrich, W.E., 1987. Mechanics of flow and sediment transport in river bends. In *River channels: Environment and process* (Vol. 18, pp. 179-227). Oxford: Blackwell.

Dietrich, W.E., Day, G. and Parker, G., 1999. The Fly River, Papua New Guinea: Inferences about river dynamics, floodplain sedimentation and fate of sediment. *Varieties of fluvial form*, pp.345-376.

Dilworth, J. and Fisher, T.G., 2018. Determining the Lake Agassiz Moorhead Phase lowstand elevation from compaction ridges and newly identified strandlines in the Red River Valley, USA. *Geomorphology*, 319, pp.216-225.

Doyle, P.F., 1988. Damage resulting from a sudden river ice breakup. *Canadian Journal of Civil Engineering*, 15(4), pp.609-615.

Dyke, A.S. and Evans, D.J., 2003. Ice-marginal terrestrial landsystems: northern Laurentide and Innuitian ice sheet margins. *Glacial landsystems*, 24.

Eardley, A.J., 1938. Yukon channel shifting. *Bulletin of the Geological Society of America*, 49(3), pp.343-358.

Edmonds, D.A., Hajek, E.A., Downton, N. and Bryk, A.B., 2016. Avulsion flow-path selection on rivers in foreland basins. *Geology*, 44(9), pp.695-698.

Edwards, L.M., 2013. The effects of soil freeze–thaw on soil aggregate breakdown and concomitant sediment flow in Prince Edward Island: A review. *Canadian Journal of Soil Science*, 93(4), pp.459-472.

Ehlers, J., Gibbard, P.L. and Hughes, P.D. eds., 2011. Quaternary glaciations-extent and chronology: a closer look (Vol. 15). Elsevier.

Emmerton, C.A., Lesack, L.F. and Vincent, W.F., 2008. Mackenzie River nutrient delivery to the Arctic Ocean and effects of the Mackenzie Delta during open water conditions. *Global Biogeochemical Cycles*, 22(1).

Ettema, R. and Daly, S.F., 2004. Sediment transport under ice. ERDC. *CRREL TR-04-20*.

Ettema, R. and Muste, M., 2001. Laboratory observations of ice jams in channel confluences. *Journal of cold regions engineering*, 15(1), pp.34-58.

Ettema, R. and Zabilansky, L., 2004. Ice influences on channel stability: Insights from Missouri's Fort Peck reach. *Journal of Hydraulic Engineering*, 130(4), pp.279-292.

Ettema, R., 2002. Review of alluvial-channel responses to river ice. *Journal of Cold Regions Engineering*, 16(4), pp.191-217.

Ettema, R., 2006. Information needs when estimating ice jam floods and ice runs. In *Extreme Hydrological Events: New Concepts for Security* (pp. 285-298). Springer, Dordrecht.

Ferrick, M.G. and Gatto, L.W., 2005. Quantifying the effect of a freeze–thaw cycle on soil erosion: laboratory experiments. Earth Surface Processes and Landforms: *The Journal of the British Geomorphological Research Group*, 30(10), pp.1305-1326.

Flint, R.F., 1971. Glacial and Quaternary Geology. Wiley and Sons.

Fullerton, D.S., Bush, C.A. and Pennell, J.N., 2003. Surficial deposits and materials in the eastern and central United States (east of 102 west longitude): *US Geological Survey Geologic Investigations Series I-2789*. US Geological Survey, Denver, Colorado, USA.

Gagliano, S.M. and Howard, P.C., 1984. The neck cutoff oxbow lake cycle along the Lower Mississippi River. In *River Meandering* (pp. 147-158). ASCE.

Gatto, L.W., 1995. Soil Freeze-Thaw Effects on Bank Erodibility and Stability (No. *CRREL-SR-95-24*). Cold Regions Research and Engineering Lab, Hanover NH

Gay, G.R., Gay, H.H., Gay, W.H., Martinson, H.A., Meade, R.H. and Moody, J.A., 1998. Evolution of cutoffs across meander necks in Powder River, Montana, USA. *Earth Surface Processes and Landforms*, 23(7), pp.651-662.

Gendaszek, A.S., Magirl, C.S. and Czuba, C.R., 2012. Geomorphic response to flow regulation and channel and floodplain alteration in the gravel-bedded Cedar River, Washington, USA. *Geomorphology*, 179, pp.258-268.

Gesch, D.B., Oimoen, M.J. and Evans, G.A., 2014. Accuracy assessment of the US Geological Survey National Elevation Dataset, and comparison with other large-area elevation datasets: SRTM and ASTER (No. 2014-1008). US Geological Survey.

Gomez, B. and Livingston, D.M., 2012. The river it goes right on: Post-glacial landscape evolution in the upper Waipaoa River basin, eastern North Island, New Zealand. *Geomorphology*, 159, pp.73-83.

Gore, J.A. and Shields, F.D., 1995. Can large rivers be restored?, *BioScience*, 45(3), pp.142-152.

Gowan, E.J., Tregoning, P., Purcell, A., Montillet, J.P. and McClusky, S., 2016. A model of the western Laurentide Ice Sheet, using observations of glacial isostatic adjustment. *Quaternary Science Reviews*, 139, pp.1-16.

Gran, K.B., Finnegan, N., Johnson, A.L., Belmont, P., Wittkop, C. and Rittenour, T., 2013. Landscape evolution, valley excavation, and terrace development following abrupt postglacial base-level fall. *Geological Society of America Bulletin*, 125(11-12), pp.1851-1864.

Gray, D.M. and Prowse, T.D., 1993. Snow and Floating Ice. Chapter 7 in *Handbook of Hydrology* (DR Maidment, ed.).

Grenfell, M., Aalto, R. and Nicholas, A., 2012. Chute channel dynamics in large, sand-bed meandering rivers. *Earth Surface Processes and Landforms*, 37(3), pp.315-331.

Güneralp, İ. and Marston, R.A., 2012. Process–form linkages in meander morphodynamics: Bridging theoretical modeling and real world complexity. *Progress in Physical Geography*, 36(6), pp.718-746.

Güneralp, İ. and Rhoads, B.L., 2011. Influence of floodplain erosional heterogeneity on planform complexity of meandering rivers. *Geophysical Research Letters*, 38(14).

Guo, J., Jing, H.W., Li, J.X. and Li, L.J., 2012. Surface water quality of Beiyun Rivers basin and the analysis of acting factors for the recent ten years. *Environmental Science*, 33(5), pp.1511-1518.

Hajek, E.A. and Wolinsky, M.A., 2012. Simplified process modeling of river avulsion and alluvial architecture: connecting models and field data. *Sedimentary Geology*, 257, pp.1-30.

Hajek, E.A., Huzurbazar, S.V., Mohrig, D., Lynds, R.M. and Heller, P.L., 2010. Statistical characterization of grain-size distributions in sandy fluvial systems. *Journal of Sedimentary Research*, 80(2), pp.184-192.

Hajic, E.R., 1990. Late Pleistocene and Holocene landscape evolution, depositional subsystems, and stratigraphy in the lower Illinois River Valley and adjacent central Mississippi River Valley (Doctoral dissertation, University of Illinois at Urbana-Champaign).

Harden, G.J., 1990. Flora of New South Wales (Vol. 4). UNSW Press.

Harris, K.L., 1987. The Quaternary Geology of the Grand Forks-Red Lake Falls Area, North Dakota-Minnesota (Vol. 87, No. 1). North Dakota Geological Survey.

Harris, K.L., and Luther, M.L., 1991, Surface Geology of the Goose River Map Area: North Dakota Geological Survey Atlas Series AS-14-Al, scale 1:250,000

Harris, K.L., Moran, S.R. and Clayton, L., 1974. Late Quaternary stratigraphic nomenclature, Red River Valley, North Dakota and Minnesota (No. 52). North Dakota Geological Survey.

Harris, K.L., West, S.A, Lusardi, B.A, and Tipping, R.G., 1995, Quaternary stratigraphy, plate 2 of Harris, K.L., project manager, Regional hydrogeologic assessment, Quaternary

geology, Red River Valley, Minnesota: Minnesota Geological Survey Regional Hydrogeologic Assessment RHA-3, Part A, scale 1 :750,000.

Hicken, E. J. and Nanson, G. C. 1984. 'Lateral migration rates of river bends', *Journal of Hydraulic Engineering*, 110, 1557–1567

Hobley, D., Adams, J.M., Siddhartha Nudurupati, S., Hutton, E.W., Gasparini, N.M., Istanbulluoglu, E. and Tucker, G.E., 2017. Creative computing with Landlab: an open-source toolkit for building, coupling, and exploring two-dimensional numerical models of Earth-surface dynamics. *Earth Surface Dynamics*, 5, pp.21-46.

Holbrook, J., and Schumm, S.A., 1999. Geomorphic and sedimentary response of rivers to tectonic deformation: a brief review and critique of a tool for recognizing subtle epeirogenic deformation in modern and ancient settings. *Tectonophysics*, 385, 286-306

Hooke, J., 2003. River meander behaviour and instability: a framework for analysis. *Transactions of the Institute of British Geographers*, 28(2), pp.238-253.

Hooke, J.M., 1995. River channel adjustment to meander cutoffs on the River Bollin and River Dane, northwest England. *Geomorphology*, 14(3), pp.235-253.

Hooke, J.M., 2004. Cutoffs galore!: occurrence and causes of multiple cutoffs on a meandering river. *Geomorphology*, 61(3), pp.225-238.

Hooke, R.L.B., 1975. Distribution of sediment transport and shear stress in a meander bend. *The Journal of Geology*, 83(5), pp.543-565.

Howard, A.D., 2009. How to make a meandering river. *Proceedings of the National Academy of Sciences*, 106(41), pp.17245-17246.

International Water Institute, 2010. LiDAR-Derived 3-m DEM, Red River Basin Mapping Initiative 2008-2010, Fargo, ND

Ippen, A. T., Drinker, P. A., Jobin, W. R. and Shemdin, 0. H., 1962. Stream dynamics and boundary shear distributions for curved trapezoidal channels, M. I T., Hydrodynamics Lab., Dept. Civil Engrg. Rept. No. 47.

Jerolmack, D.J. and Mohrig, D., 2007. Conditions for branching in depositional rivers. *Geology*, 35(5), pp.463-466.

Jerolmack, D.J. and Paola, C., 2007. Complexity in a cellular model of river avulsion. *Geomorphology*, 91(3-4), pp.259-270.

Johnson, R.H. and Paynter, J., 1967. The development of a cutoff on the River Irk at Chadderton, Lancashire. *Geography*, 52(1), pp.41-49.

Jones, L.S. and Schumm, S.A., 1999. Causes of avulsion: an overview. *Fluvial sedimentology VI*, 28, pp.171-178.

Kalke, H., McFarlane, V., Schneck, C. and Loewen, M., 2017. The transport of sediments by released anchor ice. *Cold Regions Science and Technology*, 143, pp.70-80.

Kasai, M., Marutani, T., Reid, L.M. and Trustrum, N.A., 2001. Estimation of temporally averaged sediment delivery ratio using aggradational terraces in headwater catchments of the Waipaoa River, North Island, New Zealand. *Earth Surface Processes and Landforms*, 26(1), pp.1-16.

Keller, E.A. and Swanson, F.J., 1979. Effects of large organic material on channel form and fluvial processes. *Earth surface processes*, 4(4), pp.361-380

Kelly, S. and Belmont, P., 2018. High resolution monitoring of river bluff erosion reveals failure mechanisms and geomorphically effective flows. *Water*, 10(4), p.394.

Kempema, E.W. and Ettema, R., 2011. Anchor ice rafting: observations from the Laramie River. *River research and applications*, 27(9), pp.1126-1135.

Kempema, E.W., Reimnitz, E., Clayton Jr, J.R. and Payne, J.R., 1993. Interactions of frazil and anchor ice with sedimentary particles in a flume. *Cold Regions Science and Technology*, 21(2), pp.137-149.

Kleinhans, M.G., Ferguson, R.I., Lane, S.N. and Hardy, R.J., 2013. Splitting rivers at their seams: bifurcations and avulsion. *Earth Surface Processes and Landforms*, 38(1), pp.47-61.

Knack, I.M., Tuthill, A.M. and Shen, H.T., 2010. Ice and sediment transport in channels with in-stream channel restoration structures. In *Graduate Research Symposium*, pp. 75

Knighton, D., 2014. Fluvial forms and processes: a new perspective. Routledge.

Knox, J.C., 1995. Fluvial systems since 20,000 years BP. In: Gregory, K.J., Starkel, L., Baker, V.R. (Eds.), *Global Continental Palaeohydrology*. John Wiley and Sons, Chichester, pp. 87–108.

Knox, J.C., 2000. Sensitivity of modern and Holocene floods to climate change, *Quaternary Science Reviews*, Volume 19, Issues 1–5, pp. 439-457

Koppes, M.N. and Montgomery, D.R., 2009. The relative efficacy of fluvial and glacial erosion over modern to orogenic timescales. *Nature Geoscience*, 2(9), pp.644-647.

Lai, J. and Anders, A.M., 2018. Modeled Postglacial Landscape Evolution at the Southern Margin of the Laurentide Ice Sheet: Hydrological Connection of Uplands Controls the Pace and Style of Fluvial Network Expansion. *Journal of Geophysical Research: Earth Surface*, 123(5), pp.967-984.

Lawler, D.M., 1993. Needle ice processes and sediment mobilization on river banks: the River Ilston, West Glamorgan, UK. *Journal of Hydrology*, 150(1), pp.81-114.

Leeder, M.R. and Alexander, J.A.N., 1987. The origin and tectonic significance of asymmetrical meander-belts. *Sedimentology*, 34(2), pp.217-226.

Leverington, D.W., and Teller, J.T., 2003. Paleotopographic reconstructions of the eastern outlets of glacial Lake Agassiz. *Canadian Journal of Earth Sciences* 40, pp. 1259–1278.

Lewin, J. and Brindle, B.J., 1977. Confined meanders, In *River Channel Change*, Gregory, K.J. (ed.), Wiley: Chichester, 221–233

Lewis, G.W. and Lewin, J., 1983. Alluvial cutoffs in Wales and the Borderlands. *Modern and ancient fluvial systems*, pp.145-154.

Li, J., Grenfell, M.C., Wei, H., Tooth, S. and Ngiem, S., 2019. Chute cutoff-driven abandonment and sedimentation of meander bends along a fine-grained, non-vegetated, ephemeral river on the Bolivian Altiplano. *Geomorphology*, p.106917.

Lindenschmidt, K.E., Baulch, H.M. and Cavaliere, E., 2018. River and Lake Ice Processes—Impacts of Freshwater Ice on Aquatic Ecosystems in a Changing Globe. *Water*, 10, 1586

Lord, M.L. and Kehew, A.E., 1987. Sedimentology and paleohydrology of glacial-lake outburst deposits in southeastern Saskatchewan and northwestern North Dakota. *Geological Society of America Bulletin*, 99(5), pp.663-673.

Lotsari, E., Wang, Y., Kaartinen, H., Jaakkola, A., Kukko, A., Vaaja, M., Hyyppä, H., Hyyppä, J. and Alho, P., 2015. Gravel transport by ice in a subarctic river from accurate laser scanning. *Geomorphology*, 246, pp.113-122.

Mackay, J.R. and Mackay, D.K., 1977. The stability of ice-push features, Mackenzie River, Canada. *Canadian Journal of Earth Sciences*, 14(10), pp.2213-2225.

Macklin, M.G., 1999. Holocene river environments in prehistoric Britain: human interaction and impact. *Journal of Quaternary Science: Published for the Quaternary Research Association*, 14(6), pp.521-530.

Macklin, M.G., Lewin, J. and Woodward, J.C., 2012. The fluvial record of climate change. *Philosophical Transactions of the Royal Society A: Mathematical, Physical, and Engineering Sciences*, 370(1966), pp.2143-2172.

Maddy, D. and Bridgland, D.R., 2000. Accelerated uplift resulting from Anglian glacioisostatic rebound in the Middle Thames Valley, UK?: evidence from the river terrace record. *Quaternary Science Reviews*, 19(16), pp.1581-1588.

Manitoba Conservation, 2005a. 5-m Lidar-derived DEM of the southern Red River, Manitoba, available for download at: http://mli2.gov.mb.ca/dems/index.html

Manitoba Conservation, 2005b. 5-m Lidar-derived DEM of the northern Red River, Manitoba, available for download at: http://mli2.gov.mb.ca/dems/index.html

Markham, A.J. and Thorne, C.R., 1992. Geomorphology of gravel-bed river bends. *Dynamics of gravel-bed rivers*, pp.433-450.

Mickelson, D.M. and Colgan, P.M., 2003. The southern Laurentide ice sheet. *Developments in Quaternary Sciences*, 1, pp.1-16.

Milburn, D. and Prowse, T.D., 1996. The Effect of River-Ice Break-Up on Suspended Sediment and Select Trace-Element Fluxes Paper presented at the 10th Northern Res. Basin Symposium (Svalbard, Norway–28 Aug./3 Sept. 1994). *Hydrology Research*, 27(1-2), pp.69-84.

Milburn, D. and Prowse, T.D., 2002. Under-ice movement of cohesive sediments before river-ice breakup. *Hydrological Processes*, 16(4), pp.823-834.

Mohrig, D., Heller, P.L., Paola, C. and Lyons, W.J., 2000. Interpreting avulsion process from ancient alluvial sequences: Guadalope-Matarranya system (northern Spain) and Wasatch Formation (western Colorado). *Geological Society of America Bulletin*, 112(12), pp.1787-1803.

Moore, J.N. and Landrigan, E.M., 1999. Mobilization of metal-contaminated sediment by ice-jam floods. *Environmental Geology*, 37(1-2), pp.96-101.

Moran, S.R., Clayton, L., Hooke, R.L., Fenton, M.M. and Andriashek, L.D., 1980. Glacier-bed landforms of the prairie region of North America. *Journal of Glaciology*, 25(93), pp.457-476.

Morozova, G.S. and Smith, N.D., 2000. Holocene avulsion styles and sedimentation patterns of the Saskatchewan River, Cumberland Marshes, Canada. *Sedimentary Geology*, 130(1-2), pp.81-105.

Nanson, G.C., 1980. A regional trend to meander migration. *The Journal of Geology*, 88(1), pp.100-108.

National Hydrography Dataset (NHD) for {HUC 0902}, [https://nhd.usgs.gov/]. Available URL: "http://datagateway.nrcs.usda.gov" [Accessed 10/14/2017].

Nouh, M. and Townsend, R.D., 1979. Shear-stress distribution in stable channel bends. *Journal of the Hydraulics Division*, 105(10), pp.1233-1245.

Novák, D., 2014. Local Relief Model (LRM) Toolbox for ArcGIS. Electronic Document.

Oliva, F., Viau, A.E., Bjornson, J., Desrochers, N. and Bonneau, M.A., 2016. A 1300-year reconstruction of paleofloods using oxbow lake sediments in temperate southwestern Quebec, Canada. *Canadian Journal of Earth Sciences*, 53(4), pp.378-386.

Outhet, D.N., 1974. Progress report on bank erosion studies in the Mackenzie River delta, NWT *Hydrologic aspects of northern pipeline development, 1974: Environmental-Social Comm. Northern Pipelines, Task Force on Northern Oil Devel., Rept*, pp.74-12.

Paulson, A., S. Zhong and J. Wahr. 2007. Inference of mantle viscosity from GRACE and relative sea level data, *Geophys. J. Int*. 171, 497-508

Payne, C., Panda, S. and Prakash, A., 2018. Remote sensing of river erosion on the Colville River, North Slope Alaska. *Remote Sensing*, 10(3), p.397.

Peakall, J., 1995. The influences of lateral ground-tilting on channel morphology and alluvial architecture (Doctoral dissertation, University of Leeds).

Peakall, J., 1998. Axial river evolution in response to half-graben faulting; Carson River, Nevada, USA. *Journal of Sedimentary Research*, 68(5), pp.788-799.

Peakall, J., Ashworth, P.J. and Best, J.L., 2007. Meander-bend evolution, alluvial architecture, and the role of cohesion in sinuous river channels: a flume study. *Journal of Sedimentary Research*, 77(3), pp.197-212.

Peakall, J., Leeder, M., Best, J. and Ashworth, P., 2000. River response to lateral ground tilting: a synthesis and some implications for the modelling of alluvial architecture in extensional basins. *Basin Research*, 12(3-4), pp.413-424.

Pei, S., Wehbe, N.I. and Ahrenstorff, B., 2017. Evaluation of Ice Loads on Bridge Sub-Structures in South Dakota (No. MPC 17-335).

Peltier, W.R., 2004. Global glacial isostasy and the surface of the ice-age Earth: the ICE-5G (VM2) model and GRACE. *Annu. Rev. Earth Planet. Sci.*, 32, pp.111-149.

Perron, J.T., Dietrich, W.E. and Kirchner, J.W., 2008. Controls on the spacing of first-order valleys. *Journal of Geophysical Research: Earth Surface*, 113(F4).

Phillips, R.T.J. and Desloges, J.R., 2014. Glacially conditioned specific stream powers in low-relief river catchments of the southern Laurentian Great Lakes. *Geomorphology*, 206, pp.271-287.

Phillips, R.T.J. and Desloges, J.R., 2015. Glacial legacy effects on river landforms of the southern Laurentian Great Lakes. *Journal of Great Lakes Research*, 41(4), pp.951-964.

Piégay, H. and Schumm, S.A., 2003. Systems approach in fluvial geomorphology. *Tools in Fluvial Geomorphology*; Kondolf, GM, Piégay, H., Eds, pp.103-132.

Prowse, T.D. and Conly, F.M., 2000. Multiple-hydrologic stressors of a northern delta ecosystem. *Journal of Aquatic Ecosystem Stress and Recovery*, 8(1), pp.17-26.

Prowse, T.D. and Culp, J.M., 2003. Ice breakup: a neglected factor in river ecology. *Canadian Journal of Civil Engineering*, 30(1), pp.128-144.

Prowse, T.D., Bonsal, B.R., Lacroix, M.P. and Beltaos, S., 2002, December. Trends in river-ice breakup and related temperature controls. In *Ice in the environment*. 16th IAHR international symposium on ice (Vol. 3, pp. 64-71).

Reid Jr, J.B., 1992. The Owens River as a tiltmeter for long valley Caldera, California. *The Journal of Geology*, 100(3), pp.353-363.

Reimnitz, E., Barnes, P.W. and Harper, J.R., 1990. A review of beach nourishment from ice transport of shoreface materials, Beaufort Sea, Alaska. *Journal of Coastal Research*, pp.439-469.

Reitz, M.D. and Jerolmack, D.J., 2012. Experimental alluvial fan evolution: Channel dynamics, slope controls, and shoreline growth. *Journal of Geophysical Research: Earth Surface*, 117(F2).

Reitz, M.D., Jerolmack, D.J. and Swenson, J.B., 2010. Flooding and flow path selection on alluvial fans and deltas. *Geophysical Research Letters*, 37(6).

Remenda, V.H., Cherry, J.A. and Edwards, T.W.D., 1994. Isotopic composition of old ground water from Lake Agassiz: implications for late Pleistocene climate. *Science*, 266(5193), pp.1975-1978.

Rowland, J.C., Lepper, K., Dietrich, W.E., Wilson, C.J. and Sheldon, R., 2005. Tie channel sedimentation rates, oxbow formation age and channel migration rate from optically stimulated luminescence (OSL) analysis of floodplain deposits. *Earth Surface Processes and Landforms*, 30(9), pp.1161-1179.

Ruhe, R.V., 1969. Quaternary landscapes in Iowa: Ames. *Iowa State University Press*, 2, p.55..

Russ, D.P., 1982. Style and significance of surface defomration in the vicinity of New Madrid, Missouri, *US Geological Survey Professional Paper*, (1236), p.95.

Schumm, S.A. and Winkley, B.R., 1994. The variability of large alluvial rivers. ASCE

Schumm, S.A., 1968. River adjustment to altered hydrologic regimen, Murrumbidgee River and paleochannels, Australia (Vol. 598). US Government Printing Office.

Schumm, S.A., 1969. River metamorphosis. *Journal of the Hydraulics division*, 95(1), pp.255-274.

Schumm, S.A., 1977. The fluvial system (Vol. 338). New York: Wiley.

Schumm, S.A., 1985. Patterns of alluvial rivers. Annual Review of Earth and Planetary Sciences, 13(1), pp.5-27.

Schumm, S.A., 1986. Alluvial river response to active tectonics. *Active tectonics*, pp.80-94.

Schumm, S.A., 2007. River variability and complexity. Cambridge University Press.

Schwendel, A.C., Nicholas, A.P., Aalto, R.E., Sambrook Smith, G.H. and Buckley, S., 2015. Interaction between meander dynamics and floodplain heterogeneity in a large tropical sand-bed river: the Rio Beni, Bolivian Amazon. *Earth Surface Processes and Landforms*, 40(15), pp.2026-2040.

Scrimgeour, G.J., Prowse, T.D., Culp, J.M. and Chambers, P.A., 1994. Ecological effects of river ice break-up: a review and perspective. *Freshwater Biology*, 32(2), pp.261-275.

Sella, G. F., S. Stein, T. H. Dixon, M. Craymer, T. S. James, S. Mazzotti, and R. K. Dokka, 2007. Observation of glacial isostatic adjustment in “stable” North America with GPS, *Geophysical Research Letters*, 34(2)

Sheets, B.A., Paola, C. and Kelberer, J.M., 2007. Creation and preservation of channel-form sand bodies in an experimental alluvial system. *Sedimentary processes, environments and basins: a tribute to Peter Friend*, pp.555-567.

Shields, F.D., Simon, A., and Dabney, S.M., 2009. Streambank dewatering for increased stability. *Hydrological Processes*. 23, 1537-1547

Shugar, D., Clague, J., Best, J., Schoof, C., Willis, M., Copland, L., and Roe, G., 2017. River piracy and drainage basin reorganization led by climate-driven glacier retreat. *Nature Geoscience*. 10, 370–375.

Sigafoos, R.S., 1964. Botanical evidence of floods and flood-plain deposition (Vol. 485). US Government Printing Office.

Sin, K.S., Thornton, C.I., Cox, A.L. and Abt, S.R., 2012. Methodology for calculating shear stress in a meandering channel. Prepared for US Department of Interior, Bureau of Reclamation, Albuquerque Area Office. Fort Collins, CO: Colorado State University, Engineering Research Center. 168 p.

Slingerland, R. and Smith, N.D., 2004. River avulsions and their deposits. *Annu. Rev. Earth Planet. Sci.*, 32, pp.257-285.

Smith, D.G. and Pearce, C.M., 2002. Ice jam-caused fluvial gullies and scour holes on northern river flood plains. *Geomorphology*, 42(1-2), pp.85-95.

Smith, D.G., 1979. Effects of channel enlargement by river ice processes on bankfull discharge in Alberta, Canada. *Water Resources Research*, 15(2), pp.469-475.

Smith, N.D., Slingerland, R.L., Pérez-Arlucea, M. and Morozova, G.S., 1998. The 1870s avulsion of the Saskatchewan River. *Canadian Journal of Earth Sciences*, 35(4), pp.453-466.

Starkel, L., 1991. Environmental changes at the Younger Dryas-Preboreal transition and during the early Holocene: some distinctive aspects in central Europe. *The Holocene*, 1(3), pp.234-242.

Steffen, H. and Wu, P., 2011. Glacial isostatic adjustment in Fennoscandia—a review of data and modeling. *Journal of geodynamics*, 52(3-4), pp.169-204.

Stewart, A.M. and Desloges, J.R., 2014. A 9000-year record of vertical and lateral accretion on the floodplain of the lower Thames River, southwestern Ontario, Canada, and implications for archaeological research. *Quaternary International*, 342, pp.161-172

Stouthamer, E. and Berendsen, H.J., 2001. Avulsion frequency, avulsion duration, and interavulsion period of Holocene channel belts in the Rhine-Meuse delta, the Netherlands. *Journal of Sedimentary Research*, 71(4), pp.589-598.

Straub, K.M., Paola, C., Mohrig, D., Wolinsky, M.A. and George, T., 2009. Compensational stacking of channelized sedimentary deposits. *Journal of Sedimentary Research*, 79(9), pp.673-688.

Sui, J., Wang, J., Balachandar, R., Sun, Z. and Wang, D., 2008. Accumulation of frazil ice along a river bend. *Canadian Journal of Civil Engineering*, 35(2), pp.158-169.

Taha, Z.P. and Anderson, J.B., 2008. The influence of valley aggradation and listric normal faulting on styles of river avulsion: a case study of the Brazos River, Texas, USA. *Geomorphology*, 95(3-4), pp.429-448.

Teller, J.T. and Bluemle, J.P., 1983. Geological setting of the Lake Agassiz region. *Glacial Lake Agassiz: Geological Association of Canada Special Paper*, 26, pp.5-20.

Teller, J.T. and Fenton, M.M., 1980. Late Wisconsinan glacial stratigraphy and history of southeastern Manitoba. *Canadian Journal of Earth Sciences*, 17(1), pp.19-35.

Teller, J.T. and Leverington, D.W., 2004. Glacial Lake Agassiz: A 5000 yr history of change and its relationship to the δ18O record of Greenland. *Geological Society of America Bulletin*, 116(5-6), pp.729-742.

Thayer, J.B., Phillips, R.T. and Desloges, J.R., 2016. Downstream channel adjustment in a low-relief, glacially conditioned watershed. *Geomorphology*, 262, pp.101-111.

Thomson, J., 1879. *On the flow of water round river bends*. Institution of Mechanical Engineers.

Thorne, C.R. (1991). Bank erosion and meander migration of the Red and Mississippi Rivers, USA. In: *Hydrology for the Water Management of Large River Basins (Proceedings of the Vienna Symposium, August)*, International Association of Hydrological Sciences (IAHS) Publication No. 201.

Toonen, W.H., Kleinhans, M.G. and Cohen, K.M., 2012. Sedimentary architecture of abandoned channel fills. *Earth Surface Processes and Landforms*, 37(4), pp.459-472.

Törnqvist, T.E., González, J.L., Newsom, L.A., Van Der Borg, K. and De Jong, A.F., 2002. Reconstructing "background" Rates of sea-level rise as a tool for forecasting coastal wetland loss, Mississippi Delta. Eos, *Transactions American Geophysical Union*, 83(46), pp.525-531.

Turcotte, B., Alfredsen, K., Beltaos, S. and Burrell, B.C., 2017, July. Ice-related floods and flood delineation along streams and small rivers. In *Proceedings of the 19th Workshop on the Hydraulics of Ice Covered Rivers*, Whitehorse, YT, Canada (pp. 10-12).

Turcotte, B., Morse, B., Bergeron, N.E. and Roy, A.G., 2011. Sediment transport in ice-affected rivers. *Journal of hydrology*, 409(1-2), pp.561-577.

Tuthill, A.M., and Mamone, A.C., 1997. Selection of Confluence Sites with Ice Problems for Structural Solutions, *USACE Special Report 97-4*, CRREL

Upham, W., 1896. The glacial lake agassiz (Vol. 25). US Government Printing Office.

Ursic, M.E., 2011. Quantification of shear stress in a meandering native topographic channel using a physical hydraulic model. Fort Collins, CO: Colorado State University. 154 p. Thesis.

USGS, The National Map, 2017. 3DEP products and services: The National Map, 3D Elevation Program Web page, accessed 08/30/18 at https://nationalmap.gov/3DEP/3dep_prodserv.html.

Van Dijk, W.M., Schuurman, F., Van de Lageweg, W.I. and Kleinhans, M.G., 2014. Bifurcation instability and chute cutoff development in meandering gravel-bed rivers. *Geomorphology*, 213, pp.277-291.

Vandermause, R.A., 2018. Role of dynamic ice-breakup on bank erosion and lateral migration of the Middle Susitna River, Alaska, The. 2000-2019-CSU Theses and Dissertations.

Walcott, R.I., 1970. Isostatic response to loading of the crust in Canada. *Canadian Journal of Earth Sciences*, 7(2), pp.716-727.

Walker, H.J. and Hudson, P.F., 2003. Hydrologic and geomorphic processes in the Colville River delta, Alaska. *Geomorphology*, 56(3-4), pp.291-303.

Walker, H.J., 1959. Some aspects of erosion and sedimentation in an arctic delta during breakup. Symposium on Hydrology of Deltas; Hydrology of deltas: proceedings of the Bucharest Symposium; Studies and reports in hydrology, Coastal Studies Institute, Louisiana State University.

Wang, Y., Straub, K.M. and Hajek, E.A., 2011. Scale-dependent compensational stacking: an estimate of autogenic time scales in channelized sedimentary deposits. *Geology*, 39(9), pp.811-814.

Wankiewicz, A., 1984. Analysis of winter heat flow in an ice-covered Arctic stream. Canadian *Journal of Civil Engineering*, 11(3), pp.430-443.

Wayne, W.J. and Thornbury, W.D., 1951. Glacial geology of Wabash County, Indiana.

Wheaton, J.M., Brasington, J., Darby, S.E. and Sear, D.A., 2010. Accounting for uncertainty in DEMs from repeat topographic surveys: improved sediment budgets. *Earth surface processes and landforms: the journal of the British Geomorphological Research Group*, 35(2), pp.136-156.

Whipple, K.X. and Tucker, G.E., 1999. Dynamics of the stream-power river incision model: Implications for height limits of mountain ranges, landscape response timescales, and research needs. *Journal of Geophysical Research: Solid Earth*, 104(B8), pp.17661-17674.

Whitehouse, P.L., 2018. Glacial isostatic adjustment modelling: historical perspectives, recent advances, and future directions. *Earth surface dynamics*., 6(2), pp.401-429.

Wiles, G.C. and Calkin, P.E., 1994. Late Holocene, high-resolution glacial chronologies and climate, Kenai Mountains, Alaska. *Geological Society of America Bulletin*, 106(2), pp.281-303.

Wolfe, B.B., Hall, R.I., Last, W.M., Edwards, T.W., English, M.C., Karst-Riddoch, T.L., Paterson, A. and Palmini, R., 2006. Reconstruction of multi-century flood histories from oxbow lake sediments, Peace-Athabasca Delta, Canada. *Hydrological Processes: An International Journal*, 20(19), pp.4131-4153.

Wright Jr, H.E. and Ruhe, R.V., 1965. Glaciation of Minnesota and Iowa: in Wright, HE, Jr. and Frey, DG,(eds.), *The Quaternary of the United States*.

Wuebben, J.L. and Gagnon, J.J., 1995. Ice jam flooding on the Missouri River near Williston, North Dakota. *USACE CRREL Report 95-19*

Yang, X., Pavelsky, T.M. and Allen, G.H., 2020. The past and future of global river ice. *Nature*, 577(7788), pp.69-73.

Zabilansky, L.J., Ettema, R., Wuebben, J. and Yankielun, N., 2002. Survey of River Ice Influences on Channel Bathymetry Along the Fort Peck Reach of the Missouri River, Winter 1998-1999 (*No. ERDC/CRREL-TR-02-14*). Engineering Research and Development Center, Hanover NH Cold Regions Research and Engineering Lab.

Zinger, J.A., Rhoads, B.L. and Best, J.L., 2011. Extreme sediment pulses generated by bend cutoffs along a large meandering river. *Nature Geoscience*, 4(10), p.675.

# APPENDIX A: MC MAPPER SCRIPT

```
# MC-Mapper Model (Meander-Cutoff Mapper)
# This is a script for extracting polygons that are likely meander cutoffs from high-resolution DEM data.
# The final file "Cutoffpolys.shp" still requires manual cleaning of data because other topography is very similar to cutoffs.
# It was written by Zachary Phillips during his time in the NDSU Dept. of Geosciences (with some pieces from Novak[2014])

# Load arcpy and spatial analyst
import arcpy
from arcpy import env
arcpy.CheckOutExtension("Spatial")
from arcpy.sa import *

# Set path for output folder
Output_Folder = arcpy.GetParameterAsText(0)
env.workspace = Output_Folder
arcpy.env.overwriteOutput = True

# Enter Inputs
River_Line = arcpy.GetParameterAsText(1)
DEM = arcpy.GetParameterAsText(2)
Buff_dist = arcpy.GetParameterAsText(3)
neighborhood1 = arcpy.GetParameterAsText(4)
Set_cellsize_of_input_DEM = arcpy.GetParameterAsText(5)
neighborhood2 = arcpy.GetParameterAsText(6)
Channel_Width = arcpy.GetParameterAsText(7)
min_area = arcpy.GetParameterAsText(8)

# Create Search Buffer in which to search for meander-cutoffs
Chan_buff = r"Chan_buff.shp"
arcpy.Buffer_analysis(River_Line, Chan_buff, Buff_dist, "FULL", "ROUND", "ALL", "")

# Clip DEM to extent of the Search Buffer
ClippingGeometry = Chan_buff
out_raster = "clipped_DEM.tif"
arcpy.Clip_management (DEM, "", out_raster, Chan_buff, "", "ClippingGeometry","NO_MAINTAIN_EXTENT")

# Smooth the clipped DEM to get rid of extra noise from tiny topographic features using a low pass filter
DEMinput = "clipped_DEM.tif"
SmoothDEM = FocalStatistics(DEMinput, neighborhood1, "MEAN")
SmoothDEM.save(r"SmoothDEM.tif")

# Now we put the smoothed DEM through the Local Relief Model
# Pass the smoothed DEM for the LRM input
Input_DEM = SmoothDEM

# Local variables:
smoothedx2_DEM = "low_pass.tif"
outMinus = "outMinus.tif"
break_lines = "contour.shp"
simplified_elevation_raster = "mask"
elev_points = "point.shp"
TIN = "TIN"
DTM = "DTM"
```

```
name = "FILE"
LRM = "LRM"

# Process: Focal Statistics
SmoothDEM2 = FocalStatistics(SmoothDEM, neighborhood2, "MEAN")

# Process: Minus
arcpy.CheckOutExtension("Spatial")
outMinus = arcpy.sa.Minus(SmoothDEM, SmoothDEM2)
outMinus.save(r"outMinus.tif")

# Process: Contour
arcpy.CheckOutExtension("Spatial")
arcpy.sa.Contour(outMinus, break_lines, "10000", "0")

# Process: Extract by Mask
extract_elev = arcpy.sa.ExtractByMask(SmoothDEM, break_lines)

# Process: Raster to Point
arcpy.RasterToPoint_conversion(extract_elev, elev_points, "Value")
print "raster to point done"

# Process: Create TIN
arcpy.CheckOutExtension("3d")
arcpy.CreateTin_3d(TIN, "", "point.shp grid_code Mass_Points <None>", "DELAUNAY")

# Process: TIN to Raster
arcpy.TinRaster_3d(TIN, DTM, "FLOAT", "NATURAL_NEIGHBORS", Set_cellsize_of_input_DEM, "
1")

# Process: Minus (#2)
arcpy.CheckOutExtension("Spatial")
outMinus = arcpy.Minus_3d(SmoothDEM, DTM, LRM)

# Now that the LRM is completed, we need to "remove" the current-
day channel from the LRM raster
# We'll "remove" the channel by creating a "zero" raster and mosaic-
ing it to the LRM raster
# We do this so we have a better chance of extracting meander cutoffs rather than activ
e channels
# This is because meander cutoffs still have relatively similar topography as the curre
nt channel (relative to the rest of the landscape)

# We start by making another buffer that is a little bit wider than the channel, I use
150 meters as the default
Chan_buff0 = r"River_width.shp"
arcpy.Buffer_analysis(River_Line, Chan_buff0, Channel_Width, "FULL", "ROUND", "ALL", ""
)

#first lets get the cell size of the LRM
Cell_SizeResult = arcpy.GetRasterProperties_management("LRM", "CELLSIZEX")
Cell_Size = Cell_SizeResult.getOutput(0)

# Now lets create a zero raster to mosaic into the LRM
        zeroRas = r"zeroRas.tif"
        arcpy.CheckOutExtension("Spatial")
        arcpy.gp.CreateConstantRaster_sa(zeroRas, "0", "FLOAT", Cell_Size, Chan_buff0)

        # Clip DEM to extent of the Search Buffer
        BUFFinput = "Chan_buff0.shp"
        zeroChan = r"zeroChan.tif"
```

```
        ClippingGeometry = "Chan_buff0"
        out_raster = r"buff_DEM.tif"
        arcpy.Clip_management(zeroRas, "", zeroChan, Chan_buff0, "-
    3.402823e+038", "ClippingGeometry", "NO_MAINTAIN_EXTENT")

        # Finally, let's mosaic the rasters to get rid of the channel. You can input
    your own coordinate system if necessary
        PATH = Output_Folder
        arcpy.MosaicToNewRaster_management("lrm;zeroChan.tif", PATH, "Final_LRM.tif" ,"P
    ROJCS['NAD_1983_UTM_Zone_14N',GEOGCS['GCS_North_American_1983',DATUM['D_North_American_
    1983',SPHEROID['GRS_1980',6378137.0,298.257222101]],PRIMEM['Greenwich',0.0],UNIT['Degre
    e',0.0174532925199433]],PROJECTION['Transverse_Mercator'],PARAMETER['False_Easting',500
    000.0],PARAMETER['False_Northing',0.0],PARAMETER['Central_Meridian',-
    99.0],PARAMETER['Scale_Factor',0.9996],PARAMETER['Latitude_Of_Origin',0.0],UNIT['Meter'
    ,1.0]]", "64_BIT", "3", "1", "BLEND", "MATCH")

        # Use an ISO Unsupervised classification to classify the LRM for cutoffs and non
    -cutoffs
        # First lets get some info on the LRM raster value range
        MaxLRMValue_Result = arcpy.GetRasterProperties_management("LRM", "MAXIMUM")
        LRM_Max = MaxLRMValue_Result.getOutput(0)
        MinLRMValue_Result = arcpy.GetRasterProperties_management("LRM", "MINIMUM")
        LRM_Min = MinLRMValue_Result.getOutput(0)

        LRM_Range = float(LRM_Max)-float(LRM_Min)

        # Now perform an ISO Unsupervised classification
        classes = int(3)
        sampInterval = LRM_Range / classes
        outUnsupervised = IsoClusterUnsupervisedClassification("Final_LRM.tif", classes,
     "", sampInterval)
        outUnsupervised.save("LRM_classes.tif")

        # Turn classes into polygons
        outPolygons = "LRM_polys.shp"
        arcpy.RasterToPolygon_conversion("LRM_classes.tif", outPolygons, "NO_SIMPLIFY",
    "VALUE")

        # Select and create a new shapefile for polygons that may be cutoffs. Selection
    will be made by selecting tiny polygons and those with a "gridcode" that isn't that of
    cutoff polygons (gridcode = 1)
        where_clause =  '"gridcode" = 1'
        output_data = "cutoff_polys.shp"
        arcpy.Select_analysis("LRM_polys.shp", output_data, where_clause)

        # Add area attributes to cutoff polygons so we can delete extra tiny features th
    at aren't cutoffs
        arcpy.AddGeometryAttributes_management("cutoff_polys.shp", "AREA", "", "SQUARE_M
    ETERS", "")

        # Use a search cursor to delete small polygons based on a user input threshold
        mini_area = int(min_area)
        with arcpy.da.UpdateCursor("cutoff_polys.shp", "POLY_AREA") as cursor:
            for row in cursor:
                if row[0] < mini_area:
                    cursor.deleteRow()
```

## APPENDIX B: LANDLAB AVULSION MODELING SCRIPT SAMPLES

### Decaying GIA example for Campbell reconstruction with normal topography, and low incision

```
# -*- coding: utf-8 -*-
"""
Campbell Reconstruction with Decaying GIA, Normal Topography, and Low Incision
Created on Thu Jan 30 20:59:42 2020
@author: Zach Phillips
"""

from matplotlib import pyplot as plt
from pylab import figure
import numpy as np
from landlab.components import FlowRouter, LinearDiffuser
from landlab.components import DepressionFinderAndRouter
from landlab.components import FastscapeEroder
from landlab import imshow_grid
from landlab.io import read_esri_ascii
from landlab.plot import channel_profile as prf

##### Adjust values below with values from GIA_over_time .xls file for #####
##### different reconstructions
# Name of the reconstruction by Lake Agassiz Strandline
recon_name = 'Campbell'
# gia rate type: either "decay" or "constant"
gia_type = 'decay'
k_sp_level = 'low'
k_sp = 0.00000001  # from Equation 9 and Table 2
tilt_sx = -0.000085  # from Table 3 for Campbell Reconstruction
tilt_sy = -0.000084  # from Table 3 for Campbell Reconstruction
A = 23.825  # adjustment coefficient to make tilting landscape match present tilt
###############################################################################

adj_x = abs(tilt_sx)*A
adj_y = abs(tilt_sy)*A

plotAllTimes = True

# point to the DEM's file location
DEM = r'J:\_LandscapeModeling\_GSA_Landlab\asciis\rlr_30m_utm_smth_asc.txt'

dxy = 30 # cell size for the raster

# Load the ESRI ascii DEM
(mg, z) = read_esri_ascii(DEM, name='topographic__elevation', halo=1)

# add a channel status attribute to the raster (0 for no channel, 1 for channel)
c = mg.add_zeros('node', 'chan_status')


# set watershed area for applying GIA adjustments
watershed = np.where(z > -1000)

# set the watershed outlet
mg.set_watershed_boundary_condition_outlet_id(46643, z)
```

```
53.
54.
55. ### Apply the plunges of the Upper Campbell beach strandline to
56. ### recreate the approximate topography of the Moorhead lowstand.
57.
58. if watershed:
59.     z += tilt_sx*(mg.node_x)  # Equation 1
60.     z += tilt_sy*(mg.node_y)  # Equation 2
61. else:
62.     z == -9999
63.
64. min_z = np.min(z[np.where(z>0)])
65. max_z = np.max(z[np.where(z>0)])
66.
67. fig_1 = figure(1)
68. imshow_grid(mg, z, plot_name = recon_name +' Reconstruction Estimated Topography (m)',

69.             grid_units= ['m','m'], limits=(min_z, max_z), cmap = 'gist_earth')
70. plt.close()
71.
72.
73. # route flow and fill depressions
74. fr = FlowRouter(mg, method = 'D8')
75. df = DepressionFinderAndRouter(mg)
76. fr.route_flow()
77. print('filling sinks...')
78. df.map_depressions()
79. print('done filling sinks')
80.
81.
82. fig_2 = figure(2)
83. imshow_grid(mg, mg.cell_at_node, plot_name = 'Node IDs')
84. plt.close()
85.
86.
87. # This sets the flow accumulation threshold for designating channels
88. chan_thresh = 3500000000
89.
90. # assign a value of 1 to all channel locations
91. chan_path = np.where(mg.at_node['drainage_area'] > chan_thresh)
92. if chan_path:
93.     c[chan_path] = 1
94.
95.
96. # plot the initial channel locations
97. fig_3 = figure(3)
98. imshow_grid(mg, 'chan_status', plot_name = recon_name +' Reconstruction Estimated Chann
    el Locations',
99.             grid_units=('m', 'm'), var_name=None, cmap = 'Blues')
100.        plt.close()
101.
102.
103.        ### Erosion-related Variable inputs  ###
104.        # Any uplift?
105.        uplift_rate1 = 0.0 # m/yr
106.
107.        K_sp = k_sp       # stream power coefficient [meters^(1-2*m_sp)/year]
108.
109.        K_hs = 0.00000001     # hillslope diffusion coefficient [m^2/year]
110.
111.        ### Set up model time and timesteps
```

```
112.
113.       sim_time = 10000
114.       dt1 = 100
115.       tmax = sim_time + dt1   # needs added so we actually simulate desired amount
116.                               # of time since t starts at 0
117.
118.       # More advanced options: exponents for the stream power law
119.       m_sp = 0.5
120.       n_sp = 1
121.
122.       # set up the fluvial incision component
123.       fe = FastscapeEroder(mg, K_sp = K_sp, m_sp = m_sp, n_sp = n_sp)
124.
125.
126.       # plot the location of
127.       fig_4 = figure(4)
128.       imshow_grid(mg, 'flow__sink_flag', plot_name = recon_name +' Reconstruction Outl
    et Location',
129.                   grid_units = ['m','m'], cmap = 'Blues')
130.       plt.close()
131.       # Set up the hillslope erosion component
132.       ld = LinearDiffuser(mg, linear_diffusivity=K_hs)
133.
134.       ## find the location of the largest channels
135.       profile_IDs = prf.channel_nodes(mg, mg.at_node['topographic__steepest_slope'],
136.                                       mg.at_node['drainage_area'],
137.                                       mg.at_node['flow__receiver_node'],
138.                                       number_of_channels=1)
139.
140.       ## find the distances upstream at each node along the profile
141.       profile_upstream_dists = prf.get_distances_upstream(mg,
142.                                                           len(mg.at_node['topographic_
    _steepest_slope']),
143.                                                           profile_IDs,
144.                                                           mg.at_node['flow__link_to_re
    ceiver_node'])
145.
146.       ## plot elevation vs. distance
147.       fig_5 = figure(5)
148.       plt.plot(profile_upstream_dists[0], z[profile_IDs[0]],'b-', label='chan 1')
149.       plt.title(recon_name +' Reconstruction Long Profiles')
150.       plt.ylabel('Elevation [m]')
151.       plt.xlabel('Distance Upstream [m]')
152.       plt.show(fig_5)
153.       plt.savefig(recon_name + 'profile_pre' + '.jpg')
154.       plt.close()
155.
156.       ############### This is where the erosion is going to happen ##################
157.
158.       t = np.arange(0, tmax, dt1)
159.       title_text_z = recon_name +'Simulation Topography after '+str(tmax/1000.)+' kyr\
    n'+ '$K_{sp}$='+str(K_sp) + '; $K_{hs}$='+str(K_hs) + '; $dx$='+str(dxy)
160.       title_text_SA = 'Slope-
    area relationship after '+str(tmax/1000.)+' kyr\n'+ '$K_{sp}$='+str(K_sp) + '; $K_{hs}$
    ='+str(K_hs) + '; $dx$='+str(dxy)
161.       gridlist = []
162.
163.
164.       # give our DEM a little bit of random noise to simulate an unaltered landscape
165.       np.random.seed(0)
166.       mg_noise = np.random.normal(0.0,0.4)
```

```
167.        z += mg_noise
168.
169.
170.        if plotAllTimes:
171.            plt.ion()
172.            figIter = plt.figure('Evolving Channel Location')
173.
174.        for ti in t:
175.            #last_elev = mg.copy()
176.            if plotAllTimes:
177.                plt.clf()
178.
179.                plt.close()
180.                imshow_grid(mg, 'topographic__elevation', grid_units=('m', 'm'),
181.                                var_name='Elevation (m)', cmap = 'gist_earth')
182.
183.                plt.xlabel('$x$ [m]', fontsize=16)
184.                plt.ylabel('$y$ [m]', fontsize=16)
185.                plt.title(recon_name + ' Reconstruction Topography at ' + str(ti) + ' ye
    ars')
186.                plt.pause(0.5)
187.                plt.savefig(recon_name + 'topo_'+ gia_type + str(ti) + '.jpg')
188.
189.                plt.close()
190.
191.                imshow_grid(mg, 'chan_status', grid_units=('m', 'm'),
192.                                var_name='Channel Location', cmap = 'Blues')
193.
194.                plt.xlabel('$x$ [m]', fontsize=16)
195.                plt.ylabel('$y$ [m]', fontsize=16)
196.                plt.title(recon_name + ' Reconstruction Channel Location at ' + str(ti)
    + ' years')
197.                plt.pause(0.5)
198.                plt.savefig(recon_name + '_chanloc_' + gia_type + k_sp_level + str(ti) +
     '.jpg')
199.                plt.close()
200.
201.            #Save the model grid before making any GIA or erosion happen in the timestep

202.            mg.save(recon_name + '_GIA_dec_smth_' + 'yr'+ str(ti) + '.asc')
203.
204.            # Apply a differential, dynamic, decaying uplift to the watershed nodes

205.            if watershed:
206.                z += (((adj_x)/((ti+100)))*mg.node_x)  # Equation 3
207.                z += (((adj_y)/((ti+100)))*mg.node_y)  # Equation 4
208.            else:
209.                z = -9999
210.
211.            print((ti/100)+1)
212.
213.            ld.run_one_step(dt1)
214.            fr.run_one_step()
215.            df.map_depressions()
216.            fe.run_one_step(dt1)
217.
218.            # optionally reset the c (chan_status) value to zero and get the
219.            # channel path for the timestep (turned on plots evolving channel location)

220.            # toggle off by entering 0 to map evolving channel locations
221.            c[watershed] = 0
```

```
222.
223.           # if the drainage area meets the designated threshold we assign the node a
224.           # value of 1
225.           chan_path = np.where(mg.at_node['drainage_area'] > chan_thresh)
226.           if chan_path:
227.               c[chan_path] = 1
228.           else:
229.               c = 0
230.
231.           print (ti, 'yr elapsed;', str(ti*100/sim_time) + '%',
232.                  'uplift rate (m/yr); ', uplift_rate1, 'm/n: ', m_sp/n_sp, K_sp, K_hs)
233.
234.       plt.ioff()
235.
236.
237.       fig_8 = figure(8)
238.       imshow_grid(mg, 'topographic__elevation', plot_name = recon_name + 'Reconstructi
    on End Topography',
239.                   grid_units= ['m','m'], var_name='Elevation (m)', cmap = 'gist_earth'
    )
240.       plt.savefig(recon_name + 'recon_end_topo_' + gia_type + '.jpg')
241.       plt.close()
242.
243.       ## find the location of the largest channels
244.       profile_IDs = prf.channel_nodes(mg, mg.at_node['topographic__steepest_slope'],
245.                                       mg.at_node['drainage_area'],
246.                                       mg.at_node['flow__receiver_node'],
247.                                       number_of_channels=1)
248.
249.       ## find the distances upstream at each node along the profile
250.       profile_upstream_dists = prf.get_distances_upstream(mg,
251.                                                           len(mg.at_node['topographic_
    _steepest_slope']),
252.                                                           profile_IDs,
253.                                                           mg.at_node['flow__link_to_re
    ceiver_node'])
254.
255.
256.       ## plot elevation vs. distance
257.       fig_9 = figure(9)
258.       plt.plot(profile_upstream_dists[0], z[profile_IDs[0]],'b-', label='chan 1')
259.       plt.title(recon_name + ' End Long Profiles:'+ gia_type)
260.       plt.ylabel('Elevation [m]')
261.       plt.xlabel('Distance Upstream [m]')
262.       plt.show(fig_9)
263.       plt.savefig(recon_name + 'profile_end_'+ gia_type + '.jpg')
264.
265.       print ('ALL DONE!')
```

**Constant GIA example for Campbell reconstruction with normal topography, and high incision**

```
# -*- coding: utf-8 -*-
"""
Constant GIA, Campbell Reconstruction, Normal Topography, High Incision
Created on Thu Jan 30 20:59:42 2020
@author: Zach Phillips
"""

from matplotlib import pyplot as plt
from pylab import figure
import numpy as np
from landlab.components import FlowRouter, LinearDiffuser
from landlab.components import DepressionFinderAndRouter
from landlab.components import FastscapeEroder
from landlab import imshow_grid
from landlab.io import read_esri_ascii
from landlab.plot import channel_profile as prf

##### Adjust values below with values from GIA_over_time .xls file for #####
##### different reconstructions
# Name of the reconstruction by Lake Agassiz Strandline
recon_name = 'Campbell'
# gia rate type: either "decay" or "constant"
gia_type = 'constant'
k_sp_level = 'high'
k_sp = 0.0001  # from Equation 9 and Table 2
tilt_sx = -0.000085  # from Table 3 for Campbell Reconstruction
tilt_sy = -0.000084  # from Table 3 for Campbell Reconstruction
###############################################################################

adj_x = -tilt_sx
adj_y = -tilt_sy

plotAllTimes = True

# point to the DEM's file location
DEM = r'J:\_LandscapeModeling\_GSA_Landlab\asciis\rlr_30m_utm_smth_asc.txt'

dxy = 30 # cell size for the raster

# Load the ESRI ascii DEM
(mg, z) = read_esri_ascii(DEM, name='topographic__elevation', halo=1)

# add a channel status attribute to the raster (0 for no channel, 1 for channel)
c = mg.add_zeros('node', 'chan_status')


# set watershed area for applying GIA adjustments
watershed = np.where(z > -1000)

# set the watershed outlet
mg.set_watershed_boundary_condition_outlet_id(46643, z)


### Apply the plunges of the Upper Campbell beach strandline to
```

```
### recreate the approximate topography of the Moorhead lowstand.

if watershed:
    z += tilt_sx*(mg.node_x)  # Equation 1
    z += tilt_sy*(mg.node_y)  # Equation 2
else:
    z == -9999

min_z = np.min(z[np.where(z>0)])
max_z = np.max(z[np.where(z>0)])

fig_1 = figure(1)
imshow_grid(mg, z, plot_name = recon_name +' Reconstruction Estimated Topography (m)',
            grid_units= ['m','m'], limits=(min_z, max_z), cmap = 'gist_earth')
plt.close()


# route flow and fill depressions
fr = FlowRouter(mg, method = 'D8')
df = DepressionFinderAndRouter(mg)
fr.route_flow()
print('filling sinks...')
df.map_depressions()
print('done filling sinks')


fig_2 = figure(2)
imshow_grid(mg, mg.cell_at_node, plot_name = 'Node IDs')
plt.close()


# This sets the flow accumulation threshold for designating channels
chan_thresh = 3500000000

# assign a value of 1 to all channel locations
chan_path = np.where(mg.at_node['drainage_area'] > chan_thresh)
if chan_path:
    c[chan_path] = 1


# plot the initial channel locations
fig_3 = figure(3)
imshow_grid(mg, 'chan_status', plot_name = recon_name +' Reconstruction Estimated Channel Locations',
            grid_units=('m', 'm'), var_name=None, cmap = 'Blues')
plt.close()


      ### Erosion-related Variable inputs  ###
      # Any uplift?
      uplift_rate1 = 0.0 # m/yr

      K_sp = k_sp       # stream power coefficient [meters^(1-2*m_sp)/year]

      K_hs = 0.00000001     # hillslope diffusion coefficient [m^2/year]

      ### Set up model time and timesteps

      sim_time = 10000
      dt1 = 100
```

```
114.        tmax = sim_time + dt1   # needs added so we actually simulate desired amount
115.                                # of time since t starts at 0
116.        n_tsteps = tmax/dt1
117.
118.        # More advanced options: exponents for the stream power law
119.        m_sp = 0.5
120.        n_sp = 1
121.
122.        # set up the fluvial incision component
123.        fe = FastscapeEroder(mg, K_sp = K_sp, m_sp = m_sp, n_sp = n_sp)
124.
125.
126.        # plot the location of
127.        fig_4 = figure(4)
128.        imshow_grid(mg, 'flow__sink_flag', plot_name = recon_name +' Reconstruction Outl
    et Location',
129.                    grid_units = ['m','m'], cmap = 'Blues')
130.        plt.close()
131.        # Set up the hillslope erosion component
132.        ld = LinearDiffuser(mg, linear_diffusivity=K_hs)
133.
134.        ## find the location of the largest channels
135.        profile_IDs = prf.channel_nodes(mg, mg.at_node['topographic__steepest_slope'],
136.                                        mg.at_node['drainage_area'],
137.                                        mg.at_node['flow__receiver_node'],
138.                                        number_of_channels=1)
139.
140.        ## find the distances upstream at each node along the profile
141.        profile_upstream_dists = prf.get_distances_upstream(mg,
142.                                                            len(mg.at_node['topographic_
    _steepest_slope']),
143.                                                            profile_IDs,
144.                                                            mg.at_node['flow__link_to_re
    ceiver_node'])
145.
146.        ## plot elevation vs. distance
147.        fig_5 = figure(5)
148.        plt.plot(profile_upstream_dists[0], z[profile_IDs[0]],'b-', label='chan 1')
149.        plt.title(recon_name +'Reconstruction Long Profiles')
150.        plt.ylabel('Elevation [m]')
151.        plt.xlabel('Distance Upstream [m]')
152.        plt.show(fig_5)
153.        plt.savefig(recon_name + 'profile_pre' + '.jpg')
154.        plt.close()
155.
156.        ############### This is where the erosion is going to happen ##################
157.
158.        t = np.arange(0, tmax, dt1)
159.        title_text_z = recon_name +'Simulation Topography after '+str(tmax/1000.)+' kyr\
    n'+ '$K_{sp}$='+str(K_sp) + '; $K_{hs}$='+str(K_hs) + '; $dx$='+str(dxy)
160.        title_text_SA = 'Slope-
    area relationship after '+str(tmax/1000.)+' kyr\n'+ '$K_{sp}$='+str(K_sp) + '; $K_{hs}$
    ='+str(K_hs) + '; $dx$='+str(dxy)
161.        gridlist = []
162.
163.
164.        # give our DEM a little bit of random noise to simulate an unaltered landscape
165.        np.random.seed(0)
166.        mg_noise = np.random.normal(0.0,0.4)
167.        z += mg_noise
168.
```

```
169.
170.       if plotAllTimes:
171.           plt.ion()
172.           figIter = plt.figure('Evolving Channel Location')
173.
174.       for ti in t:
175.           #last_elev = mg.copy()
176.           if plotAllTimes:
177.               plt.clf()
178.
179.               plt.close()
180.               imshow_grid(mg, 'topographic__elevation', grid_units=('m', 'm'),
181.                                   var_name='Elevation (m)', cmap = 'gist_earth')
182.
183.               plt.xlabel('$x$ [m]', fontsize=16)
184.               plt.ylabel('$y$ [m]', fontsize=16)
185.               plt.title(recon_name + ' Reconstruction Topography at ' + str(ti) + ' ye
    ars')
186.               plt.pause(0.5)
187.               plt.savefig(recon_name + 'topo_'+ gia_type + str(ti) + '.jpg')
188.
189.               plt.close()
190.
191.               imshow_grid(mg, 'chan_status', grid_units=('m', 'm'),
192.                                   var_name='Channel Location', cmap = 'Blues')
193.
194.               plt.xlabel('$x$ [m]', fontsize=16)
195.               plt.ylabel('$y$ [m]', fontsize=16)
196.               plt.title(recon_name + ' Reconstruction Channel Location at ' + str(ti)
    + ' years')
197.               plt.pause(0.5)
198.               plt.savefig(recon_name + '_chanloc_' + gia_type + k_sp_level + str(ti) +
     '.jpg')
199.               plt.close()
200.
201.           #Save the model grid before making any GIA or erosion happen in the timestep

202.           mg.save(recon_name + '_GIA_dec_smth_' + 'yr'+ str(ti) + '.asc')
203.
204.           # Apply a differential, dynamic, decaying uplift to the watershed nodes

205.           if watershed:
206.               z += (((adj_x)/((n_tsteps)))*mg.node_x)  # Equation 5
207.               z += (((adj_y)/((n_tsteps)))*mg.node_y)  # Equation 6
208.           else:
209.               z = -9999
210.
211.           print((ti/100)+1)
212.
213.           ld.run_one_step(dt1)
214.           fr.run_one_step()
215.           df.map_depressions()
216.           fe.run_one_step(dt1)
217.
218.           # optionally reset the c (chan_status) value to zero and get the
219.           # channel path for the timestep (turned on plots evolving channel location)

220.           # toggle off to map evolving channel locations
221.           c[watershed] = 0
222.
```

```
223.            # if the drainage area meets the designated threshold we assign the node a
224.            # value of 1
225.            chan_path = np.where(mg.at_node['drainage_area'] > chan_thresh)
226.            if chan_path:
227.                c[chan_path] = 1
228.            else:
229.                c = 0
230.
231.            print (ti, 'yr elapsed;', str(ti*100/sim_time) + '%',
232.                   'uplift rate (m/yr); ', uplift_rate1, 'm/n: ', m_sp/n_sp, K_sp, K_hs)
233.
234.        plt.ioff()
235.
236.
237.        fig_8 = figure(8)
238.        imshow_grid(mg, 'topographic__elevation', plot_name = recon_name + 'Reconstructi
    on End Topography',
239.                    grid_units= ['m','m'], var_name='Elevation (m)', cmap = 'gist_earth'
    )
240.        plt.savefig(recon_name + 'recon_end_topo_' + gia_type + '.jpg')
241.        plt.close()
242.
243.        ## find the location of the largest channels
244.        profile_IDs = prf.channel_nodes(mg, mg.at_node['topographic__steepest_slope'],
245.                                        mg.at_node['drainage_area'],
246.                                        mg.at_node['flow__receiver_node'],
247.                                        number_of_channels=1)
248.
249.        ## find the distances upstream at each node along the profile
250.        profile_upstream_dists = prf.get_distances_upstream(mg,
251.                                                            len(mg.at_node['topographic_
    _steepest_slope']),
252.                                                            profile_IDs,
253.                                                            mg.at_node['flow__link_to_re
    ceiver_node'])
254.
255.
256.        ## plot elevation vs. distance
257.        fig_9 = figure(9)
258.        plt.plot(profile_upstream_dists[0], z[profile_IDs[0]],'b-', label='chan 1')
259.        plt.title(recon_name + ' End Long Profiles:'+ gia_type)
260.        plt.ylabel('Elevation [m]')
261.        plt.xlabel('Distance Upstream [m]')
262.        plt.show(fig_9)
263.        plt.savefig(recon_name + 'profile_end_'+ gia_type + '.jpg')
264.
265.        print ('ALL DONE!')
```

# APPENDIX C: LANDSCAPE EVOLUTION MODELING AND CHANNEL PATH CHANGE GRAPHIC OUTPUTS

Graphic output videos of modeling results are available digitally in the supplemental materials. Filenames of supplemental files follow the format of "Reconstruction_GIA rate_incision level_ topographic smoothing_type." So, for example "Camp_con_hi_norm_topo" would denote a graphic output of the Campbell reconstruction with constant GIA tilt, high incision, normal topography, and shows the evolving topography. Another example, "Oja_dec_lo_smth_cp" would denote a graphic output of the Ojata reconstruction with decaying GIA tilt, low incision, smoothed topography, and shows the evolving channel path locations.

## APPENDIX D: GEOMORPHIC CHANGE DETECTION FOR RIVER ICE ABRASION EXPERIMENTS

### Experiment 8

***Starting terrain***

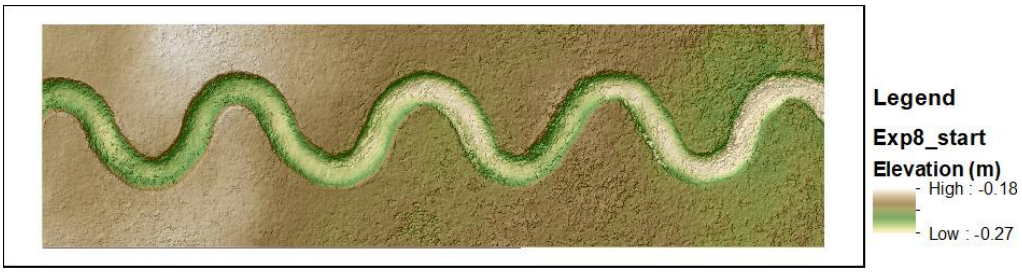


**Figure D1.** Exp. 8 Starting terrain

***Stabilization period 1 – Geomorphic Change Detection***

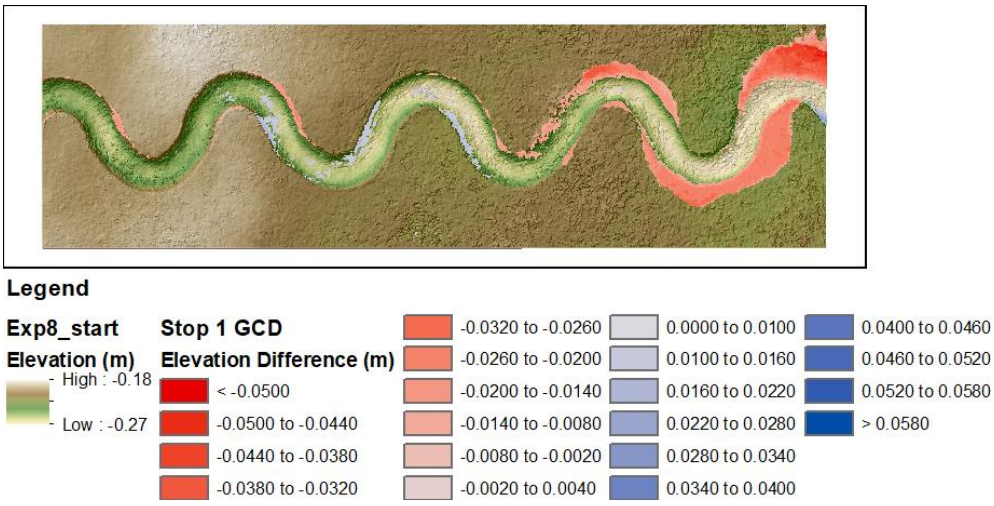


**Figure D2.** Exp. 8 Period 1 GCD

***Stop 1 terrain***

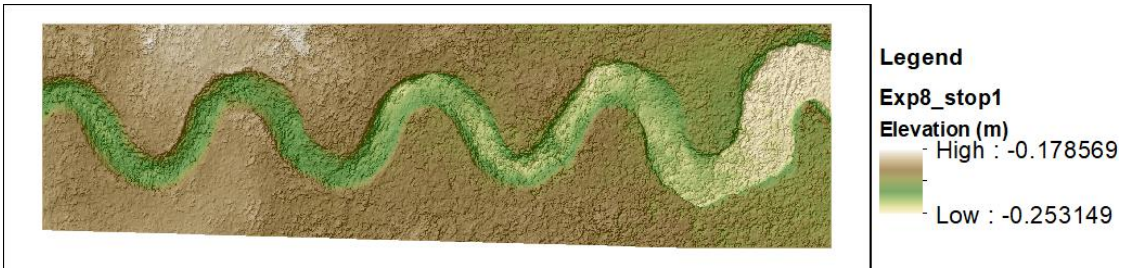


**Figure D3.** Exp. 8 Stop 1 terrain

***Stabilization period 2 – Geomorphic Change Detection***

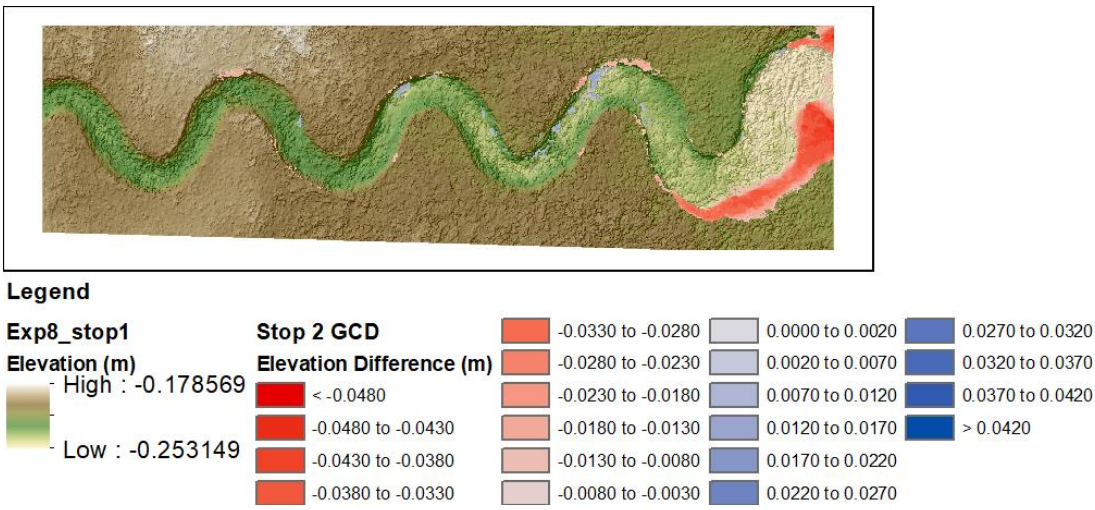


**Figure D4.** Exp. 8 Period 2 GCD

***Stop 2 terrain***

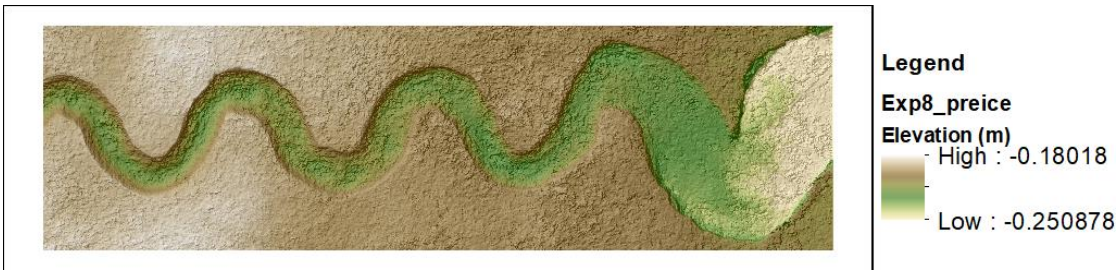


**Figure D5.** Exp. 8 Stop 2 terrain

***Stabilization period 3 – Geomorphic Change Detection***

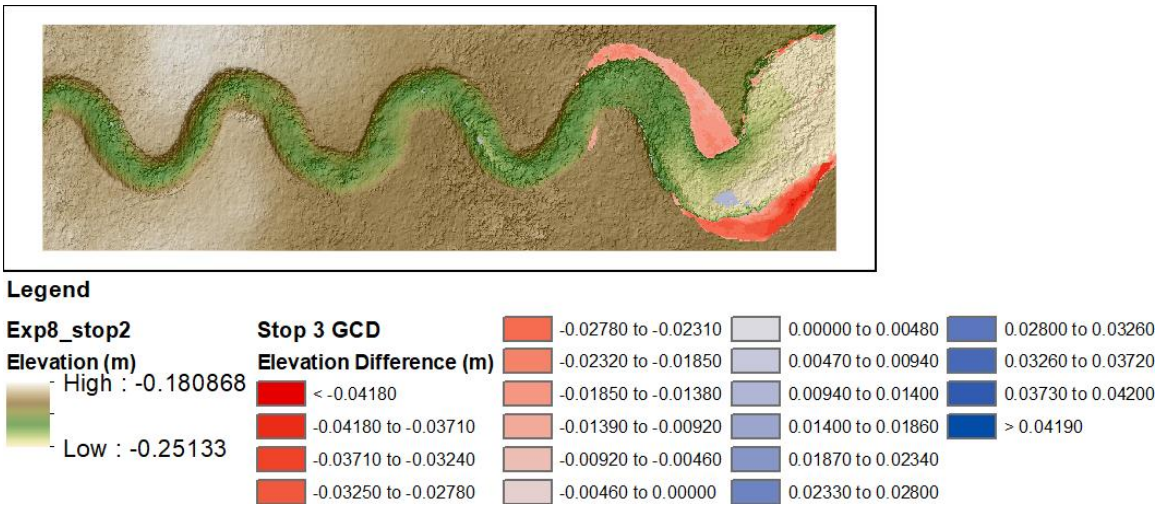


**Figure D6.** Exp. 8 Period 3 GCD

***Stop 3 terrain***

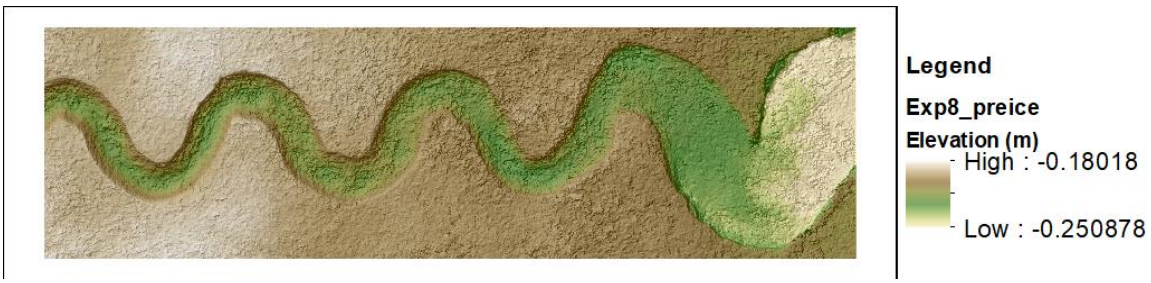


**Figure D7.** Exp. 8 Stop 3 terrain

***Ice period – Geomorphic Change Detection***

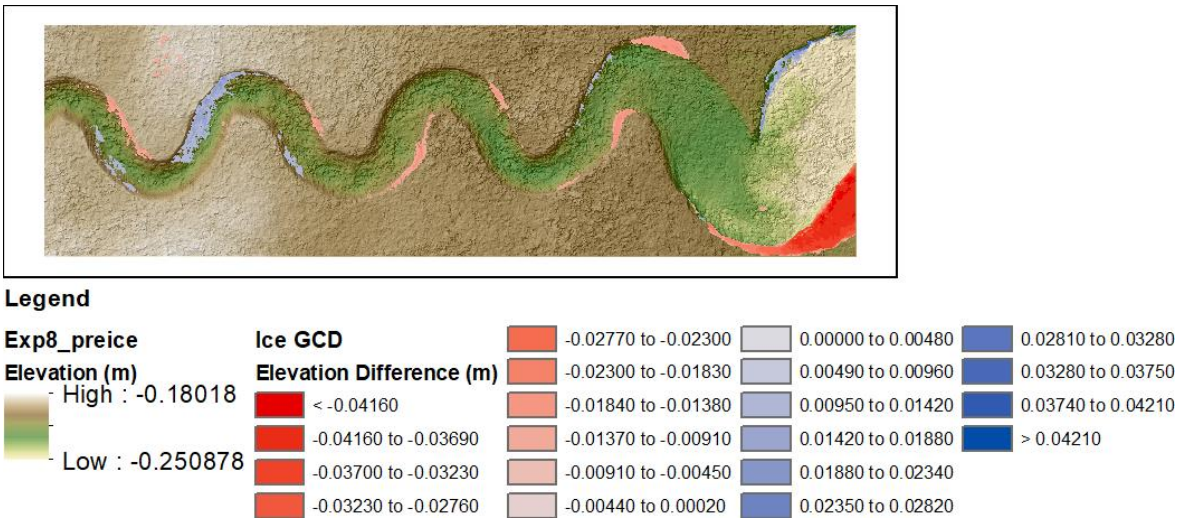


**Figure D8.** Exp. 8 Ice Period GCD

***End topography***

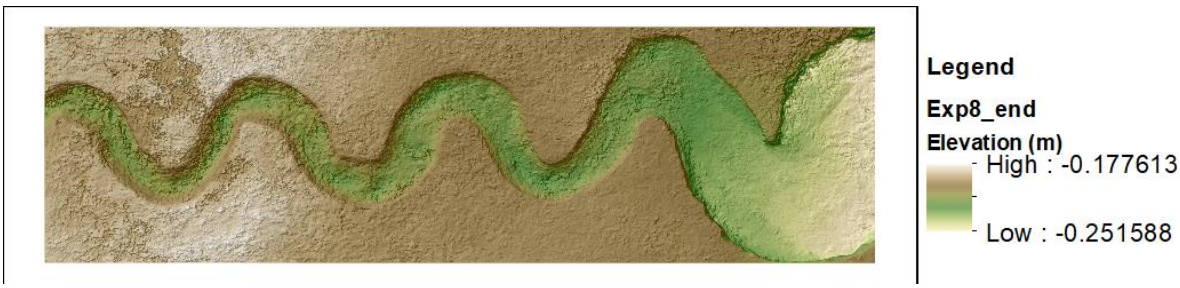


**Figure D9.** Exp. 8 End terrain

## Experiment 9

### *Starting terrain*

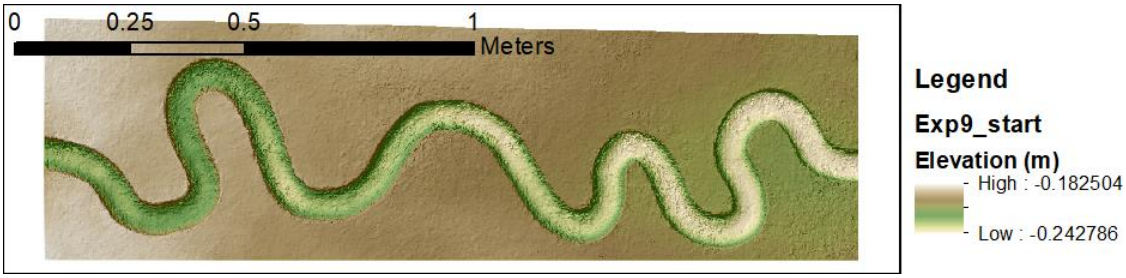


**Figure D10.** Exp. 9 Starting terrain

### *Stabilization period 1 – Geomorphic Change Detection*

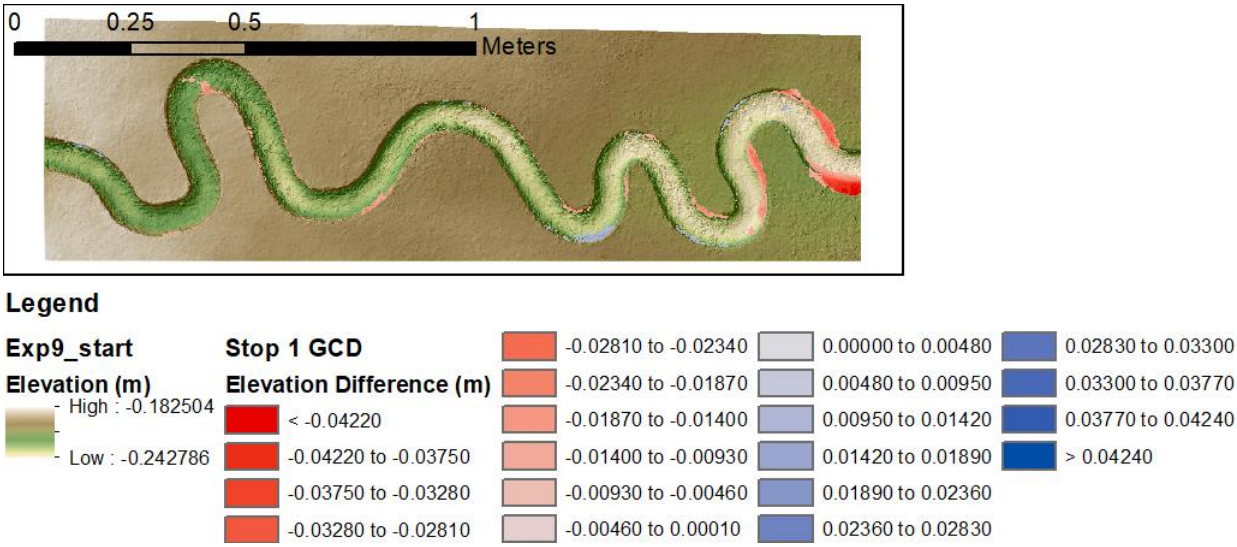


**Figure D11.** Exp. 9 Period 1 GCD

### *Stop 1 terrain*

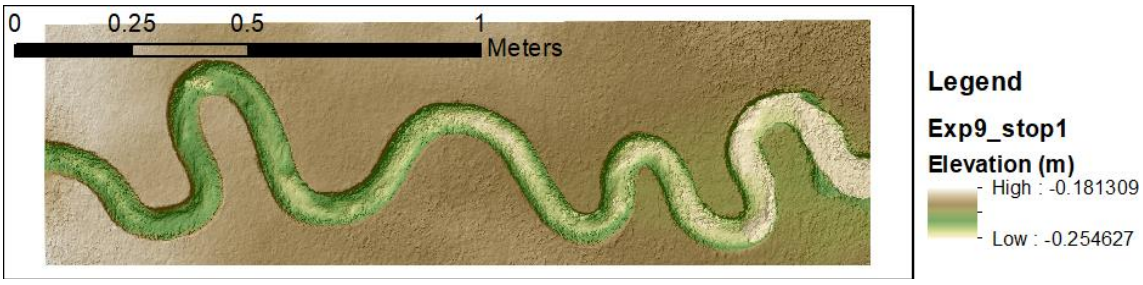


**Figure D12.** Exp. 9 Stop 1 terrain

***Stabilization period 2 – Geomorphic Change Detection***

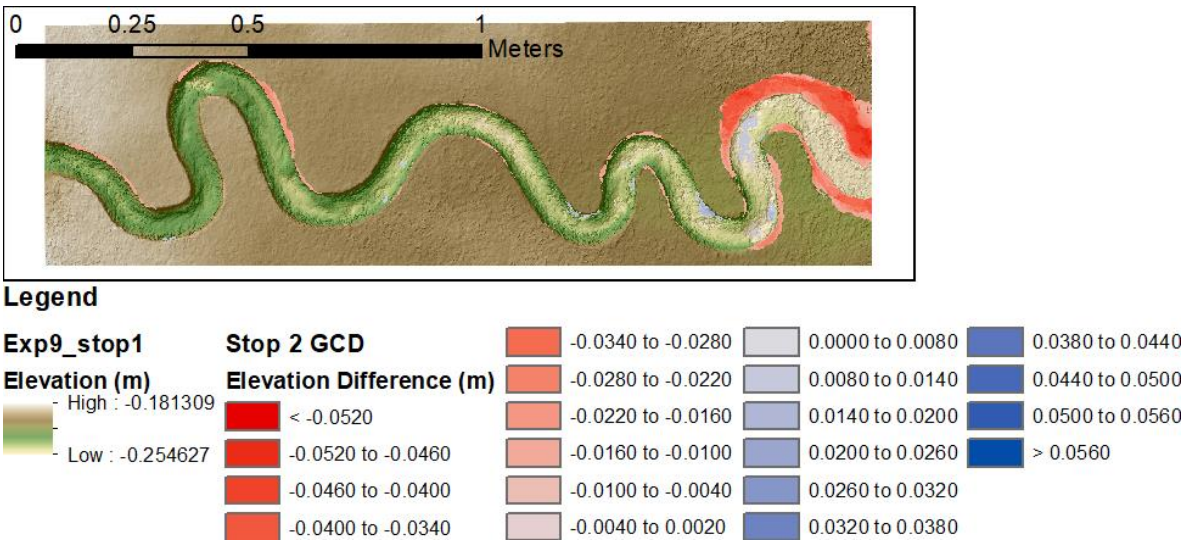


**Figure D13.** Exp. 9 Period 2 GCD

***Stop 2 terrain***

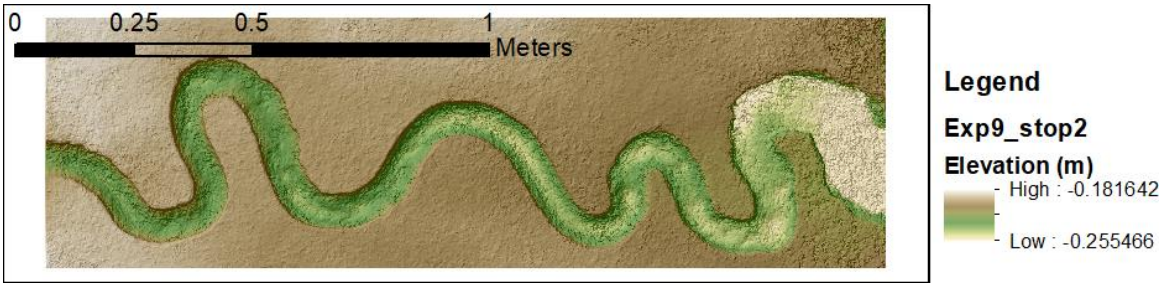


**Figure D14.** Exp. 9 Stop 2 terrain

***Stabilization period 3 – Geomorphic Change Detection***

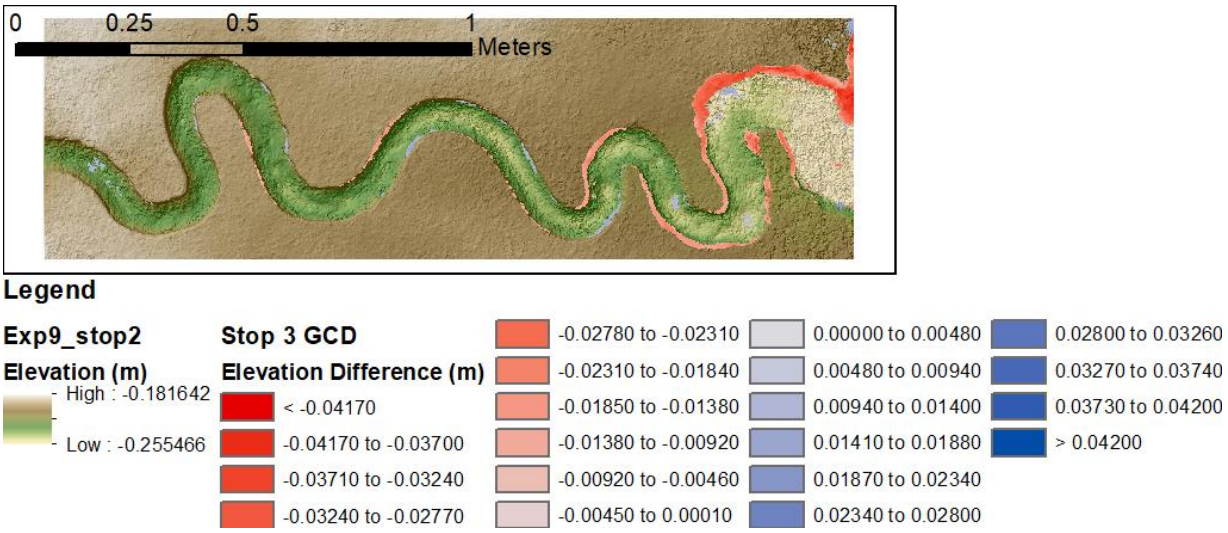


**Figure D15.** Exp. 9 Period 3 GCD

***Stop 3 terrain***

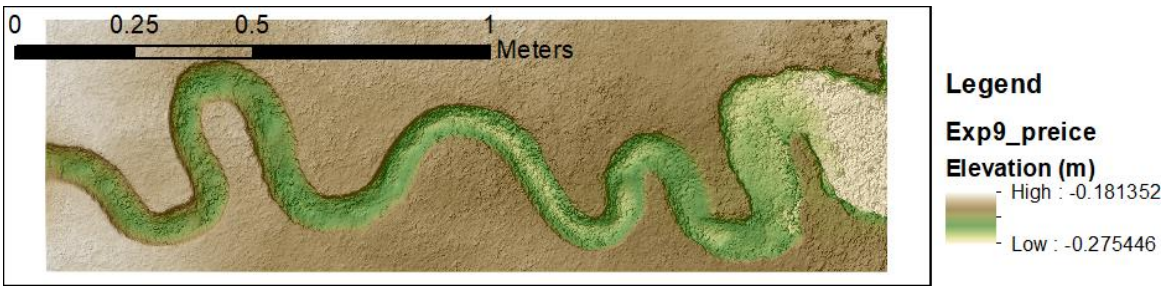


**Figure D16.** Exp. 9 Stop 3 terrain

***Ice period – Geomorphic Change Detection***

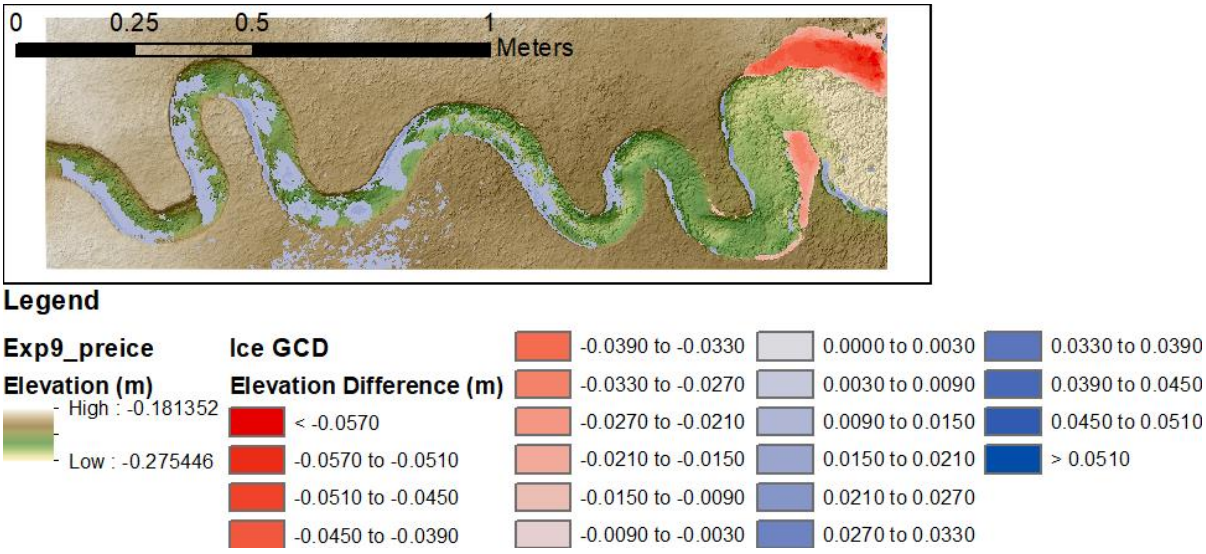


**Figure D17.** Exp. 9 Ice Period GCD

***End topography***

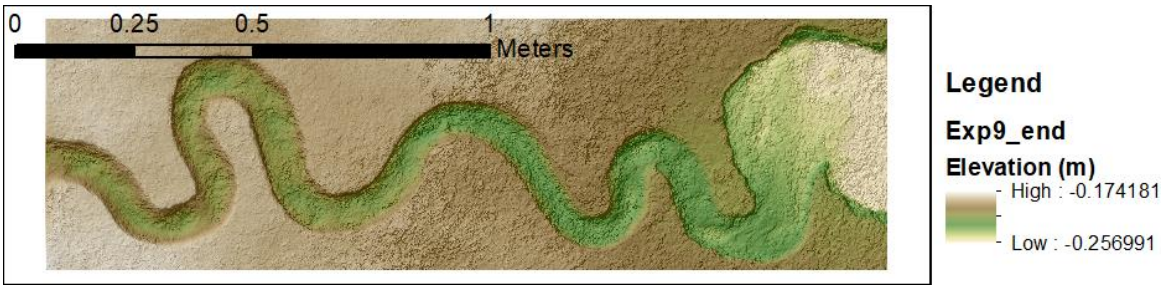


**Figure D18.** Exp. 9 End terrain

## Experiment 10

### *Starting terrain*

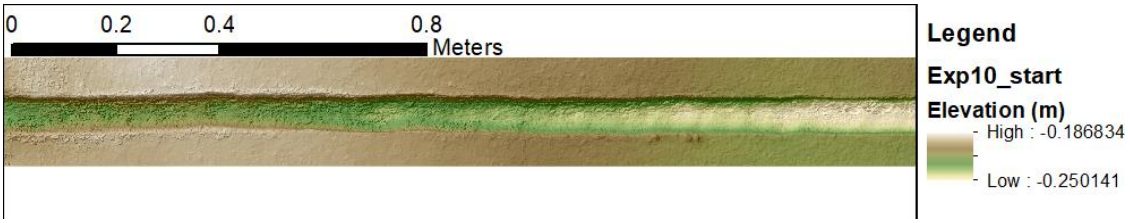


**Figure D19.** Exp. 10 Starting terrain

### *Stabilization period 1 – Geomorphic Change Detection*

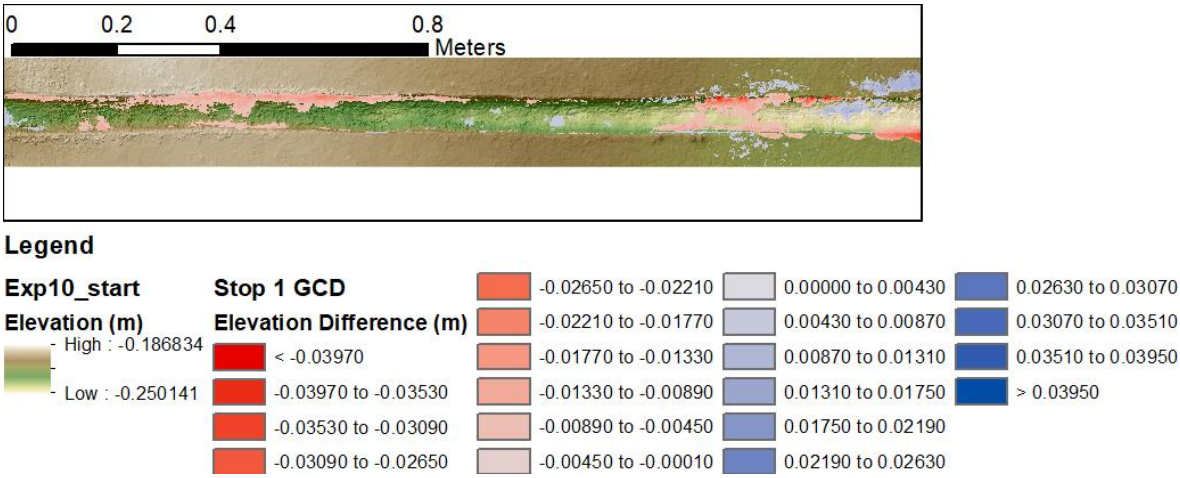


**Figure D20.** Exp. 10 Period 1 GCD

### *Stop 1 terrain*

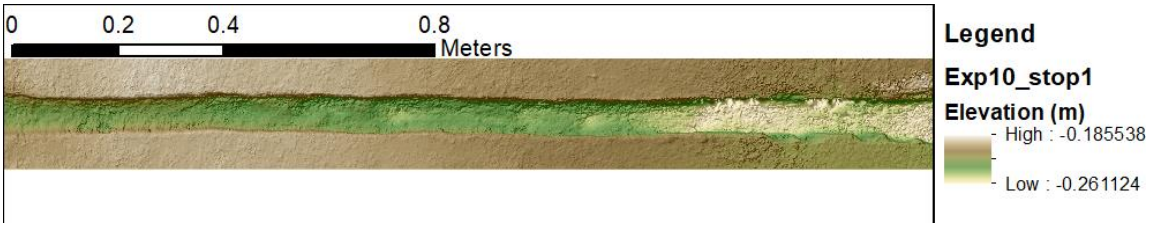


**Figure D21.** Exp. 10 Stop 1 terrain

***Stabilization period 2 – Geomorphic Change Detection***

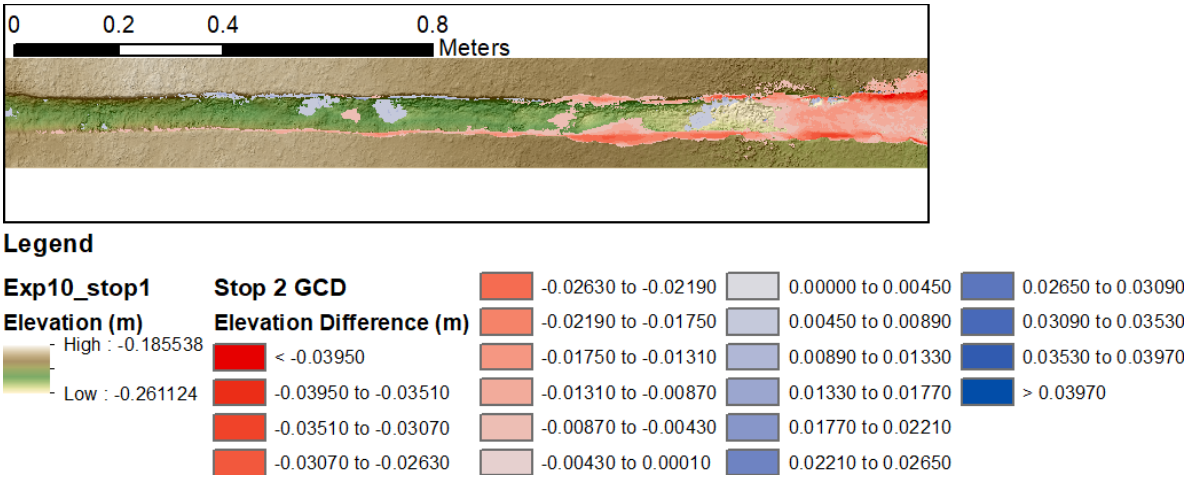


**Figure D22.** Exp. 10 Period 2 GCD

***Stop 2 terrain***

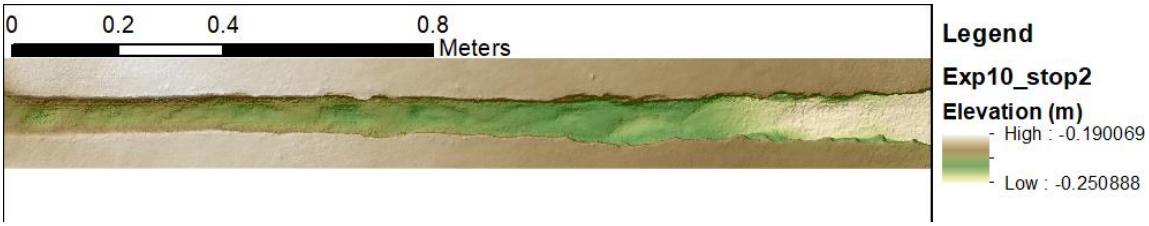


**Figure D23.** Exp. 10 Stop 2 terrain

***Stabilization period 3 – Geomorphic Change Detection***

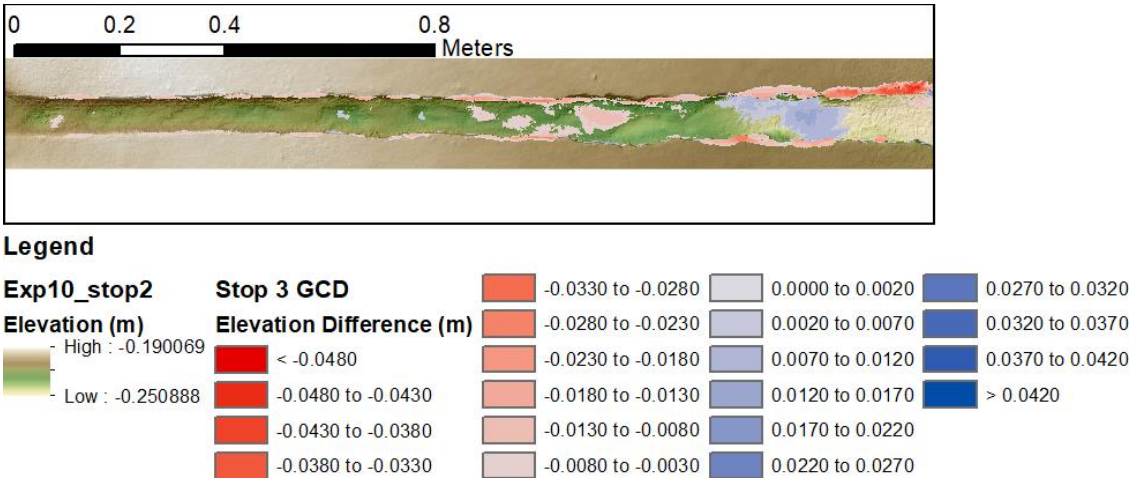


**Figure D24.** Exp. 10 Period 3 GCD

***Stop 3 terrain***

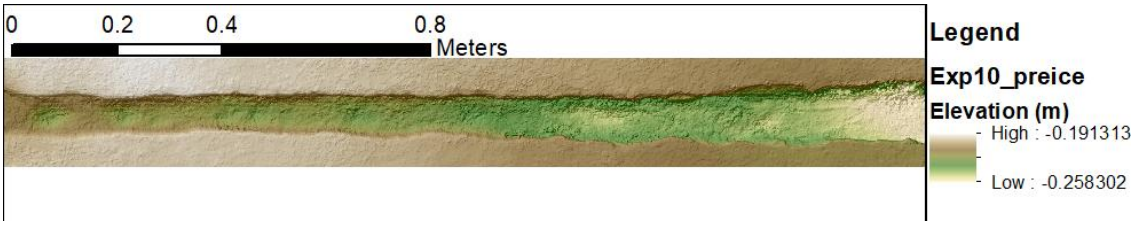


**Figure D25.** Exp. 10 Stop 3 terrain

***Ice period – Geomorphic Change Detection***

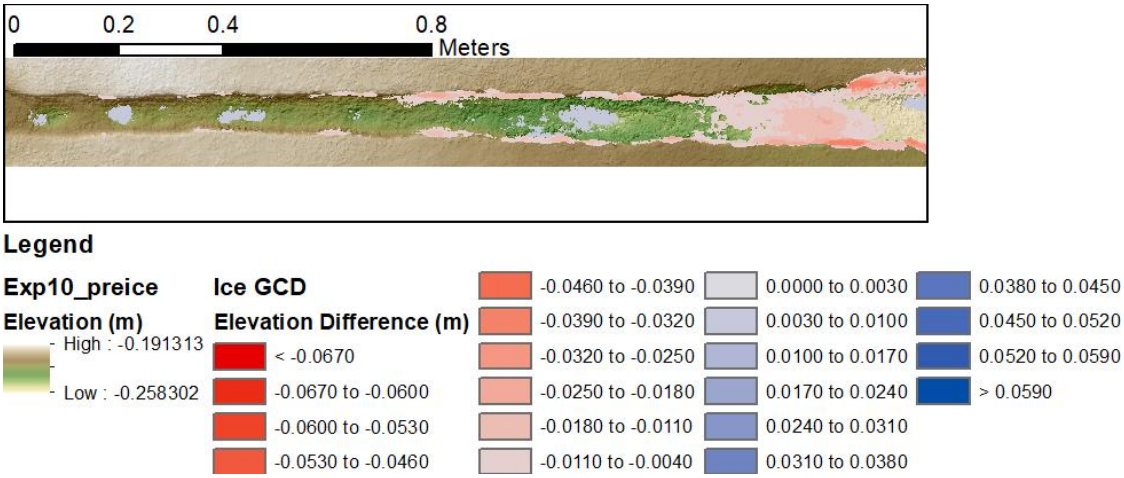


**Figure D26.** Exp. 10 Ice Period GCD

***End topography***

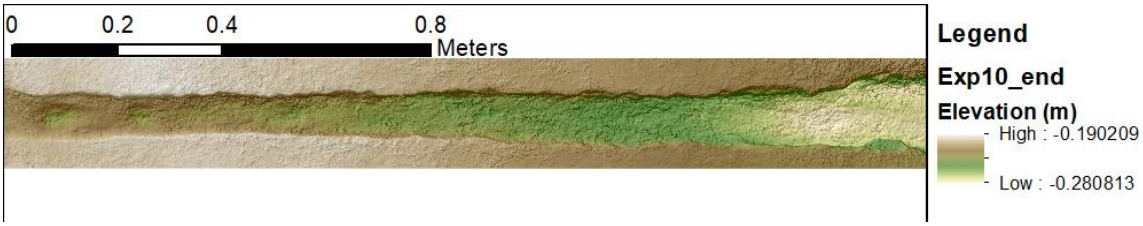


**Figure D27.** Exp. 10 End terrain

**Experiment 11**

***Starting terrain***

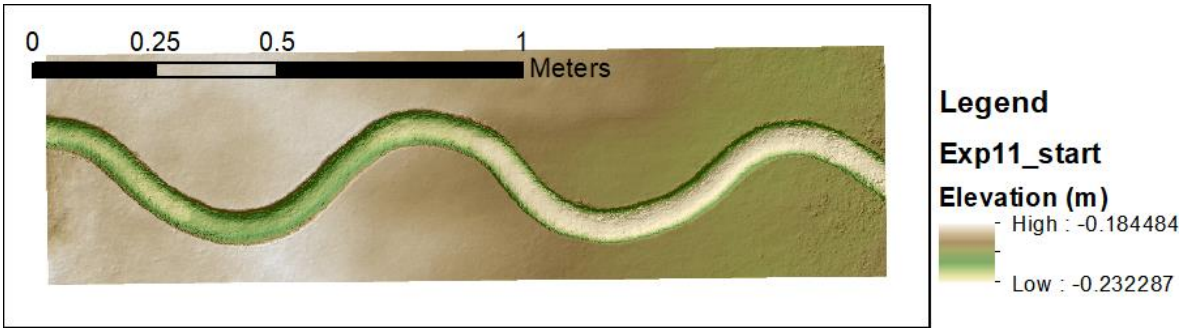


**Figure D28.** Exp. 11 Starting terrain

***Stabilization period 1 – Geomorphic Change Detection***

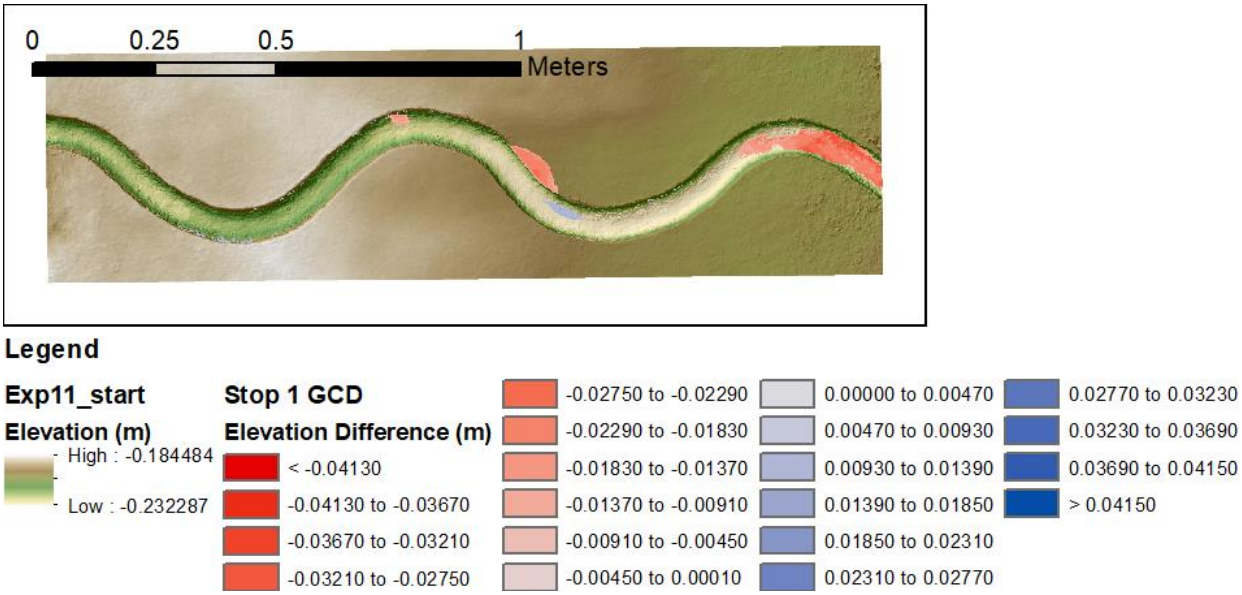


**Figure D29.** Exp. 11 Period 1 GCD

***Stop 1 terrain***

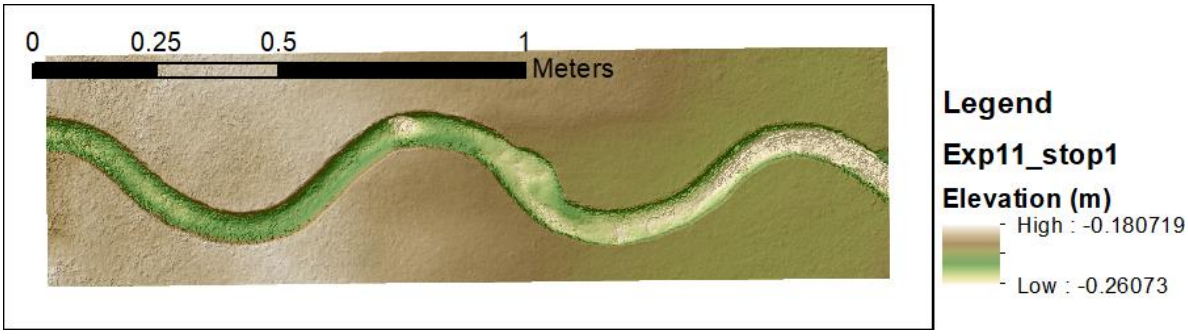


**Figure D30.** Exp. 11 Stop 1 terrain

***Stabilization period 2 – Geomorphic Change Detection***

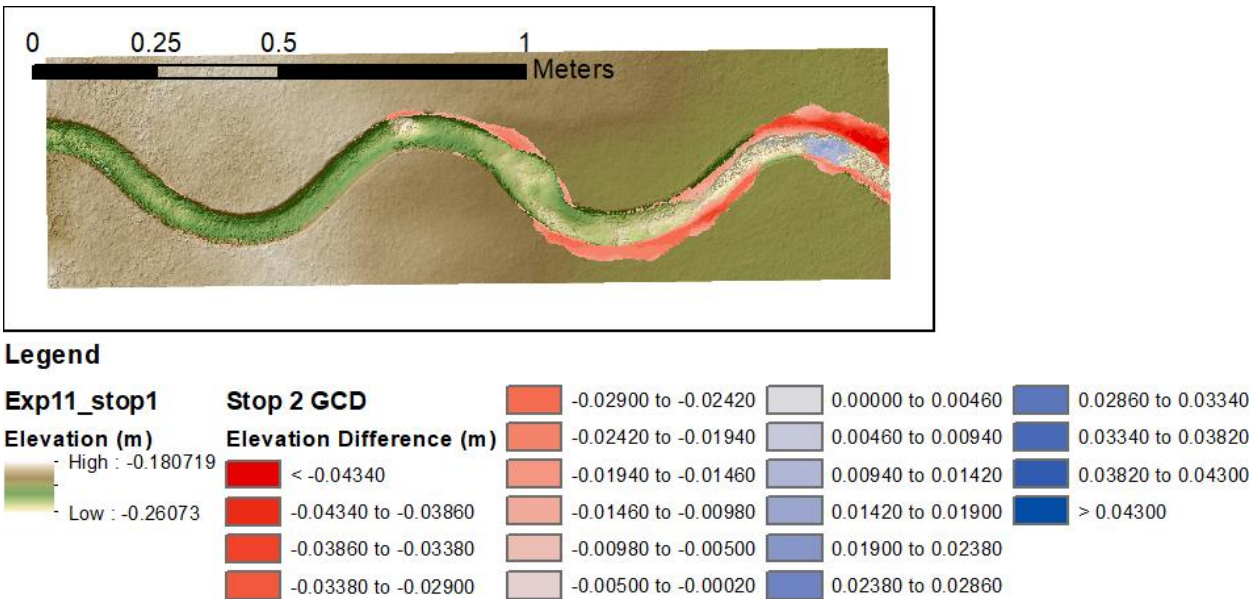


**Figure D31.** Exp. 11 Period 2 GCD

***Stop 2 terrain***

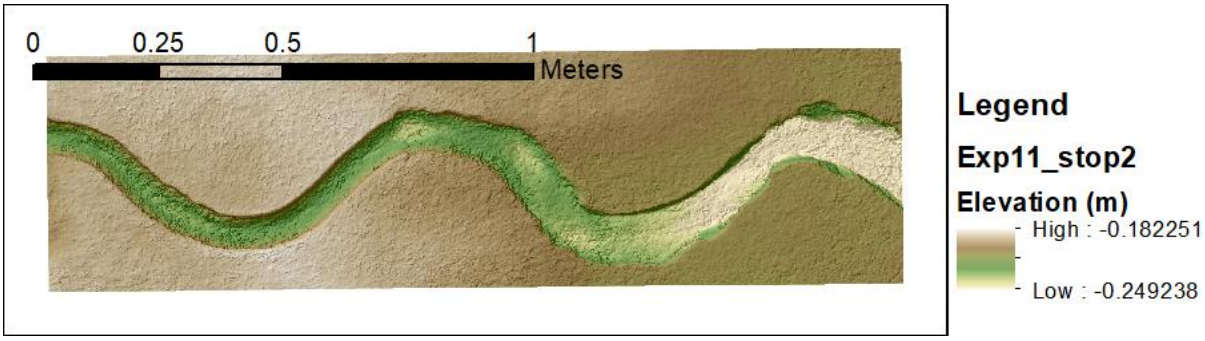


**Figure D32.** Exp. 11 Stop 2 terrain

***Stabilization period 3 – Geomorphic Change Detection***

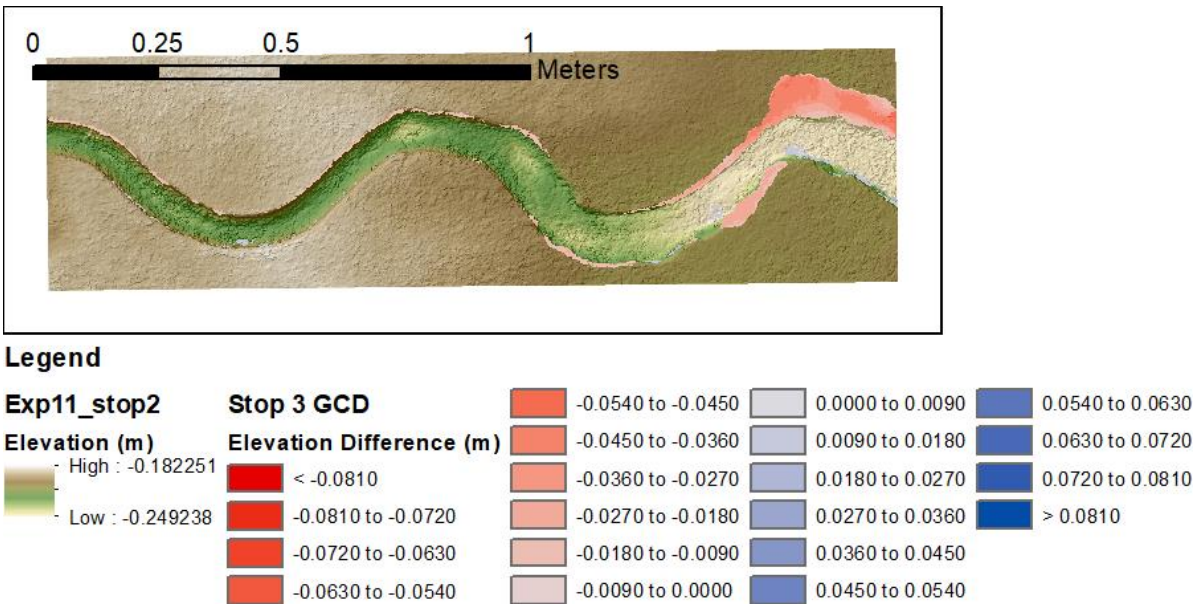


**Figure D33.** Exp. 11 Period 3 GCD

***Stop 3 terrain***

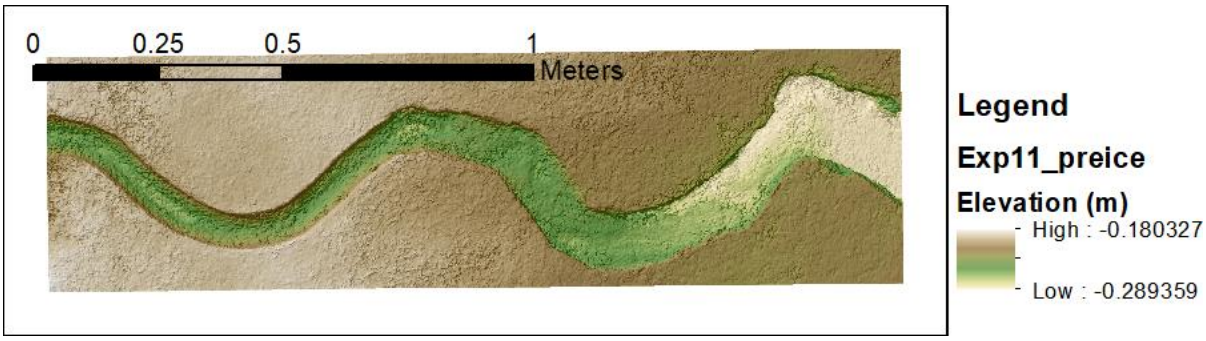


**Figure D34.** Exp. 11 Stop 3 terrain

***Ice period – Geomorphic Change Detection***

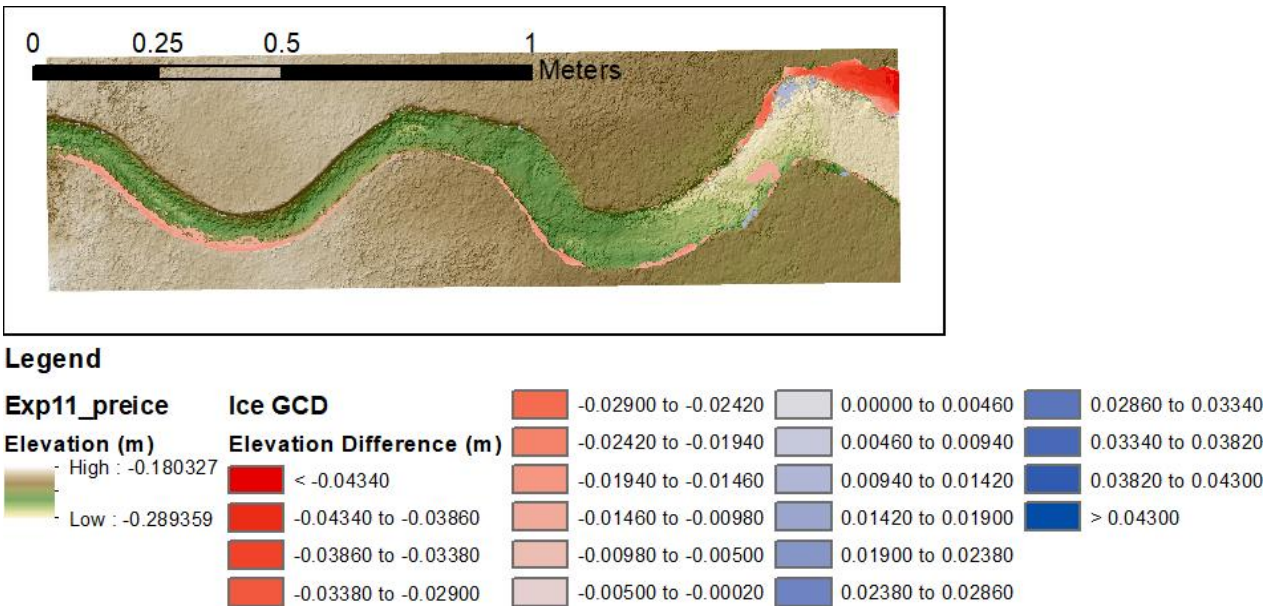


**Figure D35.** Exp. 11 Ice Period GCD

***End topography***

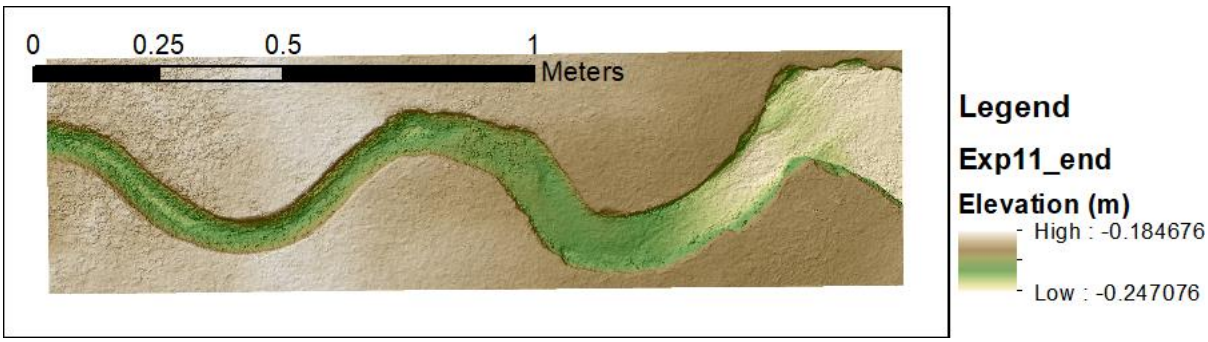


**Figure D36.** Exp. 11 End terrain

**Experiment 12**

***Starting terrain***

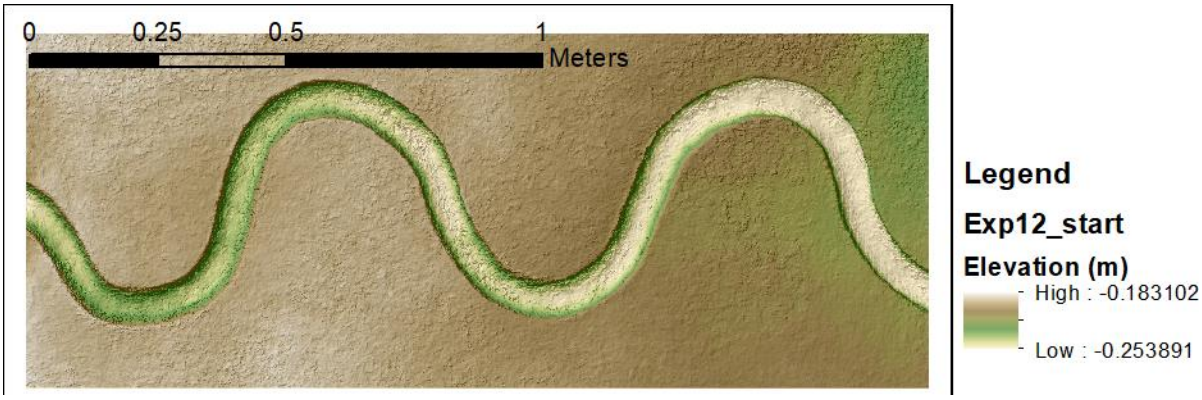


**Figure D37.** Exp. 12 Starting terrain

***Stabilization period 1 – Geomorphic Change Detection***

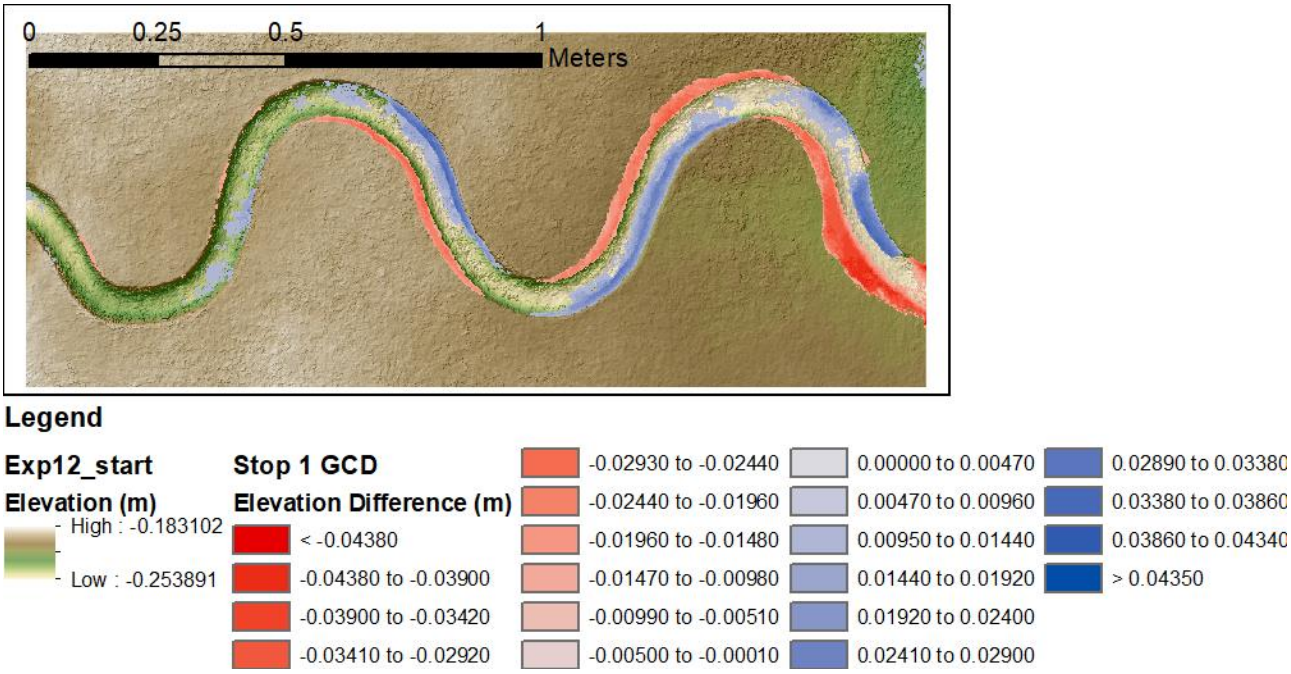


**Figure D38.** Exp. 12 Period 1 GCD

***Stop 1 terrain***

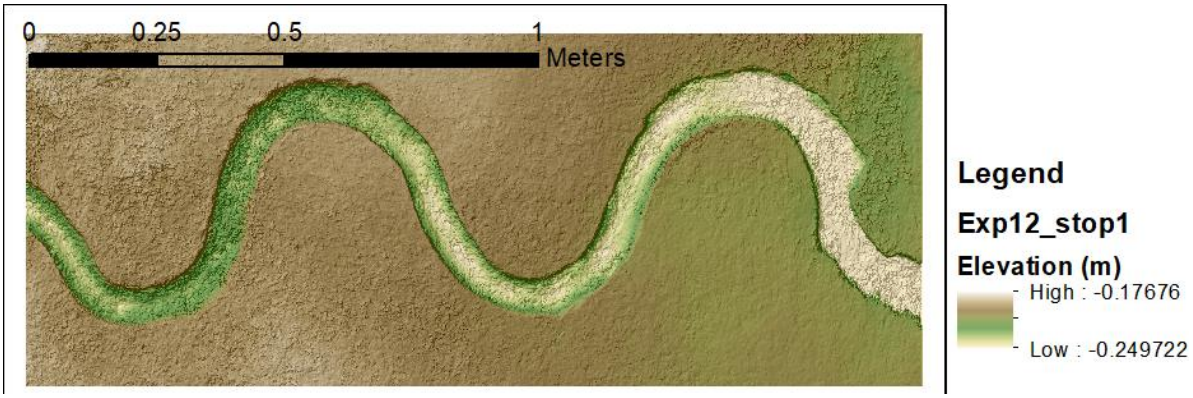


**Figure D39.** Exp. 12 Stop 1 terrain

***Stabilization period 2 – Geomorphic Change Detection***

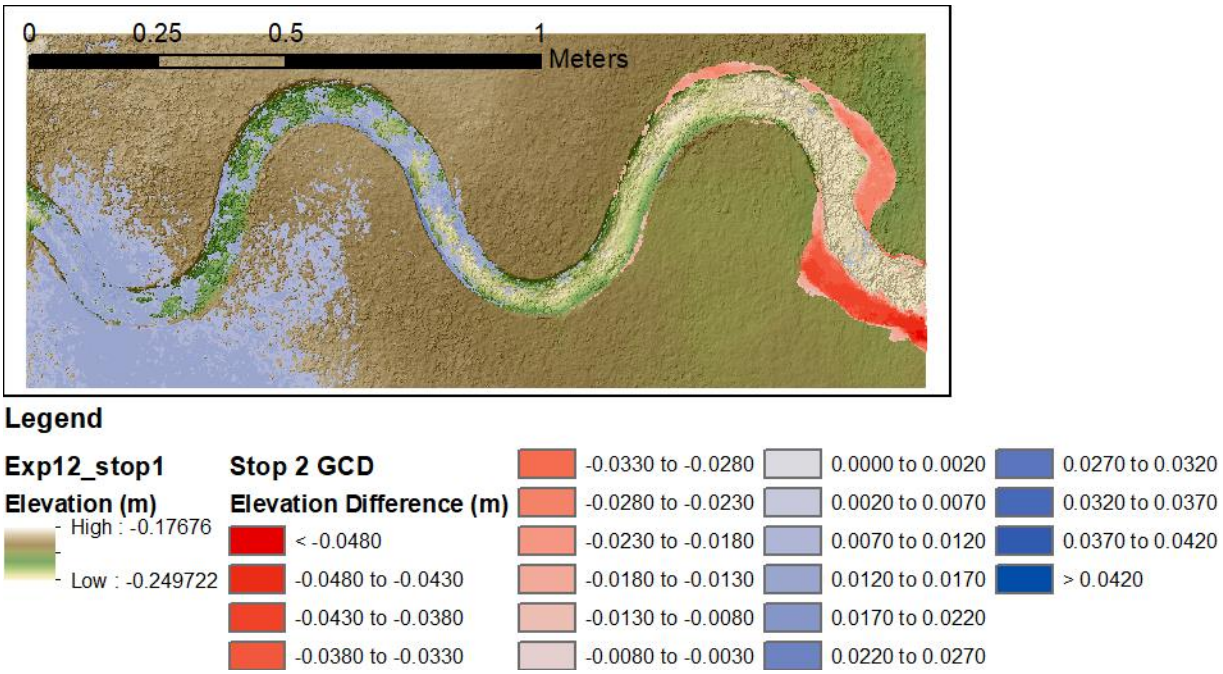


**Figure D40.** Exp. 12 Period 1 GCD

***Stop 2 terrain***

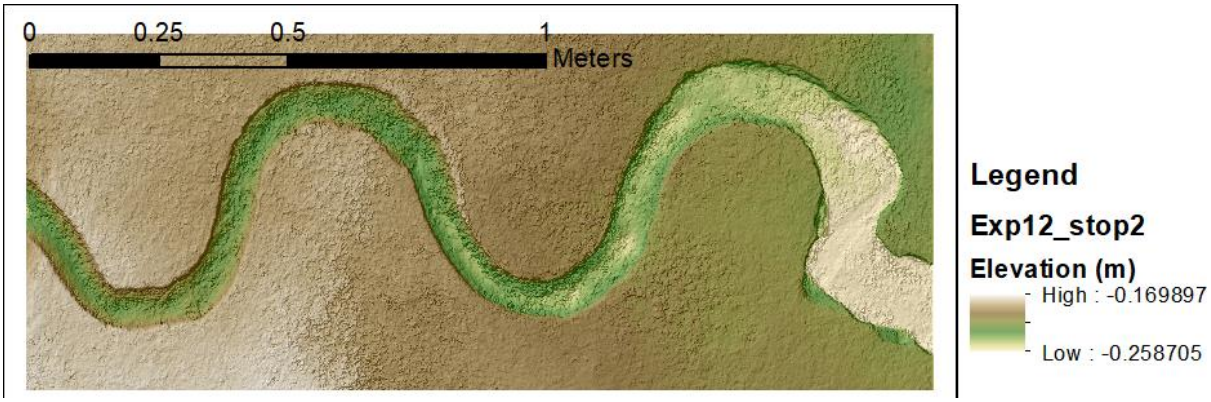


**Figure D41.** Exp. 12 Stop 2 terrain

***Stabilization period 3 – Geomorphic Change Detection***

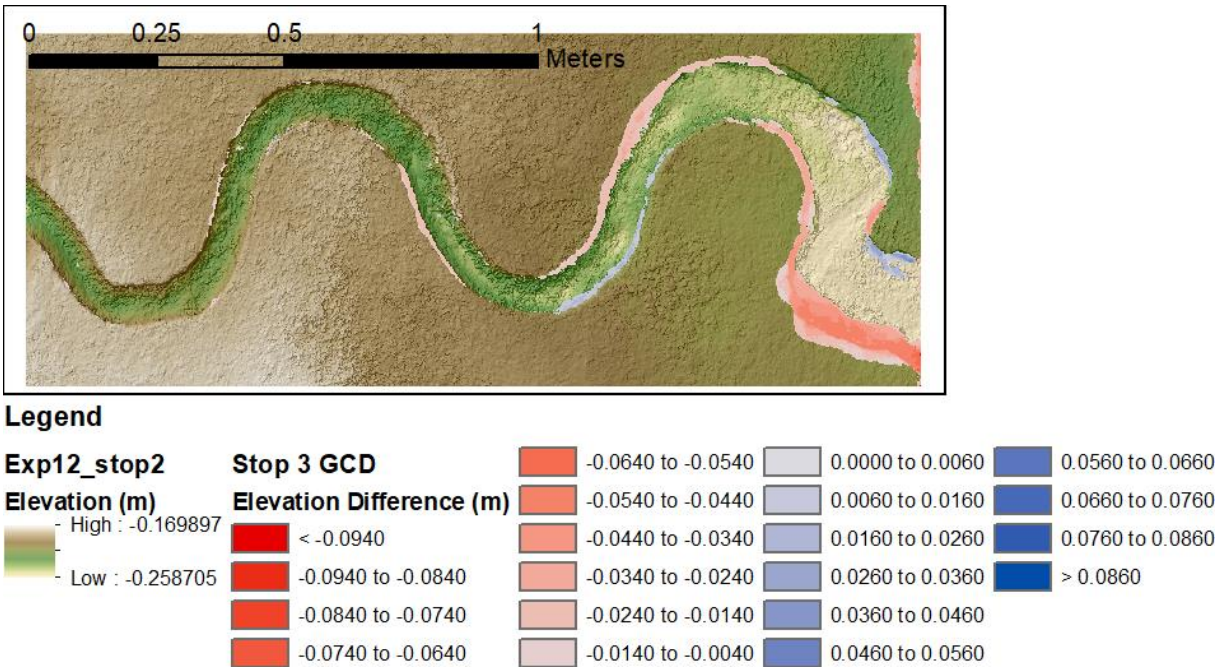


**Figure D42.** Exp. 12 Period 3 GCD

***Stop 3 terrain***

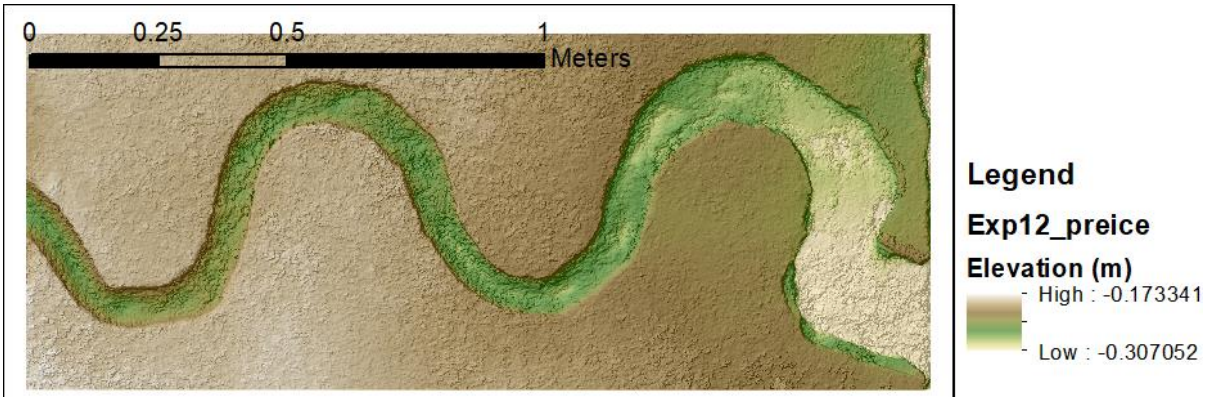


**Figure D43.** Exp. 12 Stop 3 terrain

***Ice period – Geomorphic Change Detection***

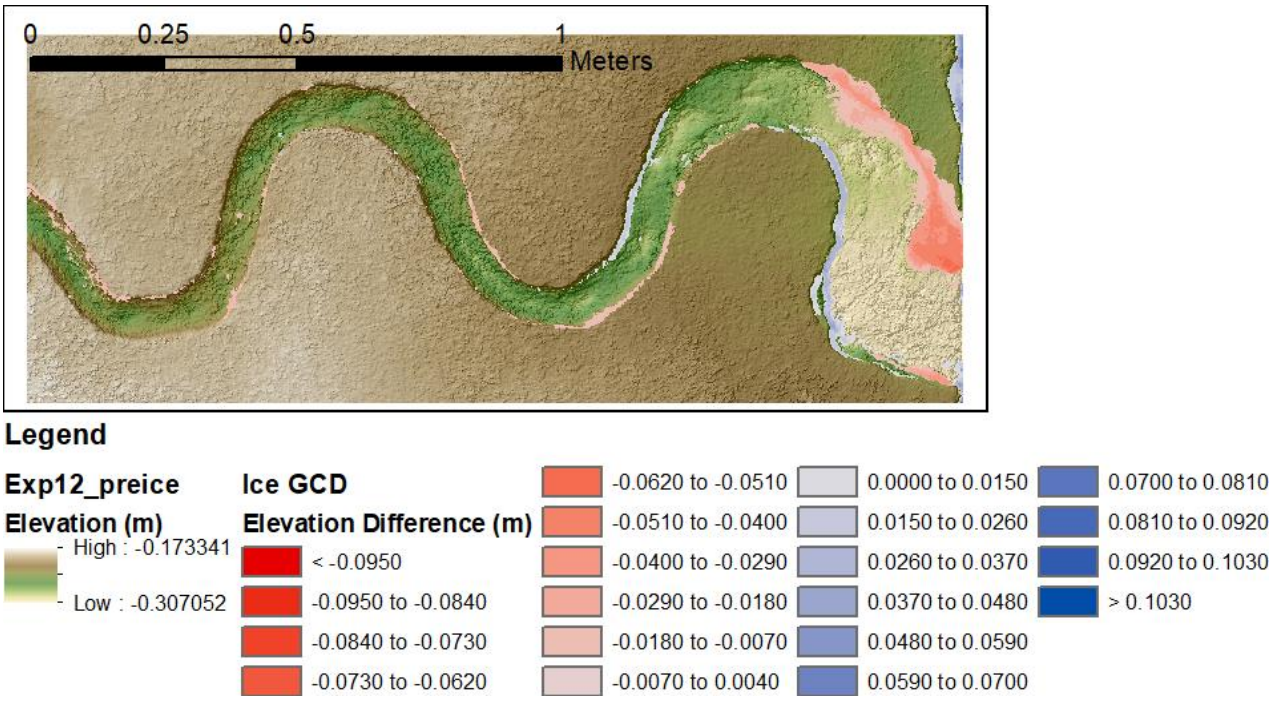


**Figure D44.** Exp. 12 Ice Period GCD

***End topography***

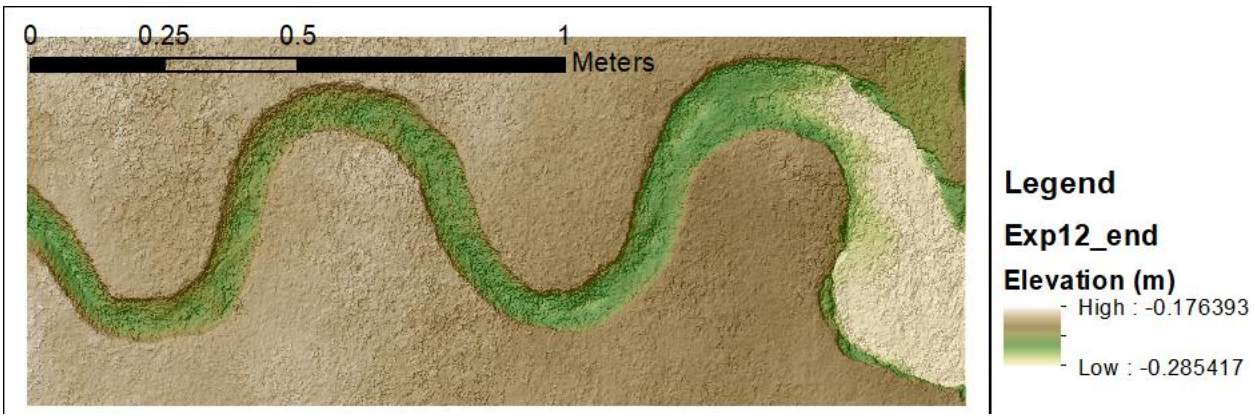


**Figure D45.** Exp. 12 End terrain